



PHD

**Computational Modelling of defects in Battery Materials
(Alternative Format Thesis)**

Squires, Alex

Award date:
2022

Awarding institution:
University of Bath

[Link to publication](#)

Alternative formats

If you require this document in an alternative format, please contact:
openaccess@bath.ac.uk

Copyright of this thesis rests with the author. Access is subject to the above licence, if given. If no licence is specified above, original content in this thesis is licensed under the terms of the Creative Commons Attribution-NonCommercial 4.0 International (CC BY-NC-ND 4.0) Licence (<https://creativecommons.org/licenses/by-nc-nd/4.0/>). Any third-party copyright material present remains the property of its respective owner(s) and is licensed under its existing terms.

Take down policy

If you consider content within Bath's Research Portal to be in breach of UK law, please contact: openaccess@bath.ac.uk with the details. Your claim will be investigated and, where appropriate, the item will be removed from public view as soon as possible.



PHD

**Computational Modelling of defects in Battery Materials
(Alternative Format Thesis)**

Squires, Alex

Award date:
2022

Awarding institution:
University of Bath

[Link to publication](#)

Alternative formats

If you require this document in an alternative format, please contact:
openaccess@bath.ac.uk

Copyright of this thesis rests with the author. Access is subject to the above licence, if given. If no licence is specified above, original content in this thesis is licensed under the terms of the Creative Commons Attribution-NonCommercial 4.0 International (CC BY-NC-ND 4.0) Licence (<https://creativecommons.org/licenses/by-nc-nd/4.0/>). Any third-party copyright material present remains the property of its respective owner(s) and is licensed under its existing terms.

Take down policy

If you consider content within Bath's Research Portal to be in breach of UK law, please contact: openaccess@bath.ac.uk with the details. Your claim will be investigated and, where appropriate, the item will be removed from public view as soon as possible.

ALEXANDER G. SQUIRES
for the degree of DOCTOR OF PHILOSOPHY

COMPUTATIONAL
MODELLING OF
DEFECTS IN
BATTERY MATERIALS

UNIVERSITY OF BATH
DEPARTMENT OF CHEMISTRY

Copyright © 2022 Alexander G. Squires

Attention is drawn to the fact that copyright of this thesis rests with the author. A copy of this thesis has been supplied on condition that anyone who consults it is understood to recognise that its copyright rests with the author and that they must not copy it or use material from it except as permitted by law or with the consent of the author.

This work is licensed under a Creative Commons “Attribution 4.0 International” license.



First printing, March 2022

Declaration of Authorship

I, Alexander G. Squires, declare that this thesis titled “Computational Modelling of Defects in Battery Materials” and the work presented in it are my own. I confirm that:

- where the thesis or any part of the thesis such as a published paper, has been produced jointly with others, that a substantial part is the original work of myself, and
- where the thesis incorporates material already submitted for another degree, the extent of that material and the degree, if any, obtained.

Signed



Date:

15 / 3 / 22

Acknowledgements

Despite some rough moments I have truly enjoyed my Ph.D. studies and no small amount of the credit for that lies with my supervisor, Ben Morgan. Ben's enthusiasm for—and commitment to—rigorous and meaningful research and how that research is communicated has been an inspiration. Other group members also deserve thanks for preempting my mistakes or graciously answered questions I had, in particular, Sam Coles, Jacob Dean, the honorary Morgang-member Dan Davies and Kit McColl. My academic efforts were also supported by collaborators such as Wolfgang Zeier, David Scanlon and Aron Walsh. David and Aron deserve extra thanks for their hospitality at conferences in far-flung places.

Camaraderie has come from the group members listed above, but in addition, I must thank Drew and Adam for never saying no to a Friday pint (and Steve Parker for often paying for those pints); my willing and able protege Patrick; Conn for patient assistance whenever I couldn't get my computers to work (and the barbeques/gigs/brews); and of course Georgie for being the trailblazing Ph.D. student in the group who should be commended for her diligent studies at the Académie de la Bière.

I am hugely grateful to the developers and maintainers of the excellent open-source software available to those studying the chemistry of materials. Without `PYMATGEN`, `ASE`, and `CPLAP` I would not have enjoyed myself half as much. Beyond materials simulation codes I am indebted to the developers of the Scientific Python Stack, and `JUPYTER`, the glue that has held my work together. Additional thanks to the research computing staff at Bath and UCL for keeping my calculations running, and to the UKRI and MCC for the provision of ARCHER(2).

The support of friends and family has meant a great deal. Robbie, Habiba, and Lydia were excellent neighbours in Bristol and I have appreciated frequent escapes to Starsmead in the Gloucestershire countryside.

Mum and Dad, I owe you everything.

Isabel, thank you for being a positive enabler, a constant voice of reason, and my teammate.

Finally, I have been assured that only my examiners and possibly my mum will ever try and read this dissertation, and so if you aren't one of those people and you make it past the acknowledgements, thanks.

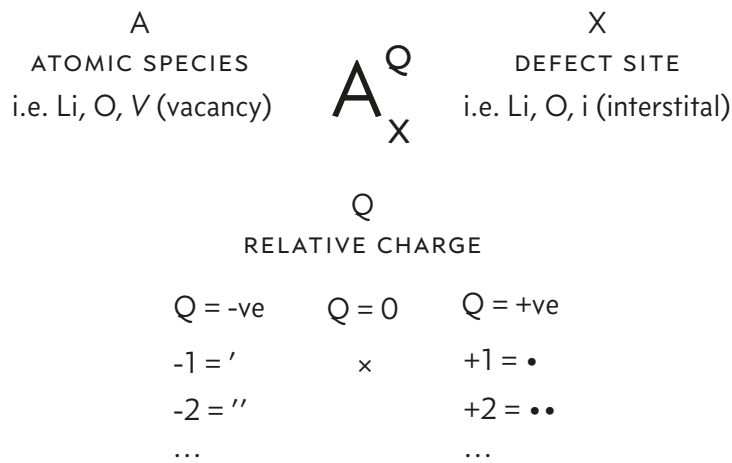
Contents

1	Lithium batteries	5
2	Point defects in solid electrolytes	17
3	Practicable solutions to Schrödinger's wave equation for solid-state systems	31
4	Methodology	45
5	Defect chemistry and aliovalent doping response in Li_3OCl	59
6	Point defect chemistry of the lithium garnet LLZO	81
7	Low electronic conductivity of LLZO from first principles	97
8	Evidence for an inductive effect in the lithium solid electrolyte LGPS on isovalent doping	113
9	Closing remarks	127

On notation

Kröger-Vink notation

In this work, point defects are described using **Kröger-Vink** notation: a point defect consists of a (atomic) species A , occupying site X with relative charge $Q = q_A - q_X$. A positive relative charge is indicated by superscript ‘•’ symbols, the number of which is equal to the magnitude of the charge. A relative negative charge is indicated with ‘’ symbols in an analogous fashion. ‘×’ is used to indicate no charge associated with the defect. We have exclusively indicated a vacant site using an italic V , to avoid confusion with vanadium defects. The notation is summarised in the schematic below



Miscellaneous

Concentrations are indicated with square brackets, i.e., the concentration of defect X would be given as $[X]$.

List of Abbreviations

AIMD	<i>Ab Initio</i> Molecular Dynamics
CBM	Conduction Band Minimum
CI-NEB	Climbing-Image Nudged Elastic Band
COHP	Crystal Orbital Hamilton Population
COOP	Crystal Orbital Overlap Population
CPLAP	Chemical Potential Limits Analysis Program
DFT	Density Functional Theory
DOS	Density of States
EC:DMC	(mixture of) Ethylene Carbonate and Dimethyl Carbonate
Ex-C	Exchange and Correlation
GGA	Generalised Gradient Approximation
HEG	Homogeneous Electron Gas
HSE06	Heyd–Scuseria–Ernzerhof (hybrid DFT functional)
ICOHP	Integrated Crystal Orbital Hamilton Population
ICOOP	Integrated Crystal Orbital Overlap Population
ICC	Image Charge Correction
KS	Kohn-Sham
LCAO	Linear Combination of Atomic Orbitals
LDA	Local Density Approximation
LGPS	$\text{Li}_{10}\text{GeP}_2\text{S}_{12}$
LISICON	Lithium SuperIonic CONductor
LLZO	$\text{Li}_7\text{La}_3\text{Zr}_2\text{O}_{12}$
NASICON	NAtrium SuperIonic CONductor
NEB	Nudged Elastic Band
PAW	Projector Augmented Wave method
PBE	Perdew-Burke-Ernzerhof (GGA functional)
PBEsol	Perdew-Burke-Ernzerhof revised for solids
SEI	Solid-Electrolyte Interface
VBM	Valence Band Maximum

List of Symbols

a_0	Bohr radius	$5.29 \times 10^{-11} \text{ m}$
e	elementary charge	$1.602\,176\,62 \times 10^{-19} \text{ C}$
F	Faraday constant	$96\,485.3329 \text{ C mol}^{-1}$
h	Planck's constant	$6.626\,070\,04 \times 10^{-34} \text{ m}^2 \text{ kg s}^{-1}$
k_B	Boltzmann constant	$1.380\,648\,52 \times 10^{-23} \text{ m}^2 \text{ kg s}^{-2} \text{ K}^{-1}$
m_e	rest mass of an electron	$9.109\,383\,701\,5 \times 10^{-31} \text{ kg}$
ϵ_0	vacuum permittivity	$8.854\,187\,812\,8 \times 10^{-12} \text{ F m}^{-1}$
C_{specific}	specific capacity	
D	diffusion coefficient	
E_{Fermi}	Fermi energy	eV
$\Delta E_f^{X^q}$	formation energy of defect X in charge state q	eV
E_g	bandgap	eV
$E(X, q/q')$	transition level for defect X^q to defect $X^{q'}$	eV
g_{X^q}	spin degeneracy of defect X in charge state q	
$g(E)$	density of states	
\hat{H}	many-body Hamiltonian operator*	
\mathbf{k}	wave-vector associated with a periodic electronic structure	
m^*	effective mass	m_e
N_X	site degeneracy of defect X	
q	defect charge state	e
\mathbf{r}	position vector	
\hat{T}	kinetic energy operator*	
T	temperature	K
V	potential energy	
X^q	defect X in charge state q	e
Z	charge on nucleus	
α	Madelung constant	
ϵ	dielectric constant	
η	doping response efficiency	
μ_i	chemical potential of species i	
$\mu_i^{\text{mob.}}$	mobility of species i	
ρ	(electron) density	

$\sigma_{\text{electronic}}$	electronic conductivity	S cm^{-1}
σ_{ionic}	ionic conductivity	S cm^{-1}
τ	scattering time	
Φ	Kohn-Sham many-body wave function*	
χ	non-interacting single-electron wave function	
Ψ	many-body wave function*	

*When referring to a single-electron analogue, the indicated symbols are presented in lower case, i.e. the many-body wave function Ψ becomes ψ when considering the wave function of a single electron. Likewise, the many-body Hamiltonian, \widehat{H} , becomes \widehat{h} .

Abstract

Suitably cost-effective energy storage will aid in the migration to a low carbon global energy economy. In an attempt to access such technology, recent years have seen a great deal of research into enabling a step change in the performance of lithium-ion batteries. One perceived route to achieving this is an all-solid-state battery, in which the flammable liquid electrolyte used in commercial battery technologies is replaced with a solid that has a high lithium-ion conductivity. Such batteries may have improved energy density and reliability as compared to the current state-of-the-art. Optimising the properties of these solid-electrolytes for successful incorporation into a battery cell has proved challenging, and a commercially viable all-solid cell has yet to be produced. Within this thesis, we argue for a full understanding of point defect chemistry to learn more about the performance and properties of crystalline solid electrolytes. In doing so we discuss these solid-state ionic materials through the lens of semiconductor defect chemistry, highlighting the importance of considering the coupling between defect populations via the electronic chemical potential, or rather the Fermi energy. We show how perturbations to the Fermi energy (facilitated by aliovalent doping) affect the concentrations of all charged defects in the system, questioning the validity of the commonly held assumption that the charge imbalance introduced by aliovalent dopants is compensated by changing concentrations of mobile-ion defects. This leads to potential difficulties in assigning a simple composition-property relationships. This approach reveals that the lithium-ion conductor Li_3OCl is, from a defect chemistry perspective, a somewhat poor candidate solid electrolyte and that the garnet ion conductor $\text{Li}_7\text{La}_3\text{Zr}_2\text{O}_{12}$ (LLZO) has a more complex than previously considered doping response. We then build on this model to examine electronic carrier populations in LLZO, discussing possible non-negligible *electronic* conductivity, which has been linked to battery failure owing to a bulk lithium reduction process. Finally, we explicitly consider dopant-driven changes in defect–host–framework interactions which result in modulations to the potential energy surface for lithium ion transport in the superionic conductor $\text{Li}_{10}\text{GeP}_2\text{S}_{12}$. To close, we briefly discuss the practical and theoretical challenges posed by modelling the point defect chemistry of solid electrolytes more fully. It is hoped that this work will inspire more considerations of the equivalence between a picture of defect chemistry in functional materials that invokes charge-neutral defect reactions and one which considers a system where the concentrations of all charged defects are coupled.

Preface: the pressing need for an energy revolution

“There is no square mile of earth’s inhabitable surface that is not beautiful in its own way, if we men will only abstain from wilfully destroying that beauty.”

—William Morris, 1881

“I want you to act like the house is on fire, because it is.”

—Greta Thunberg, 2019

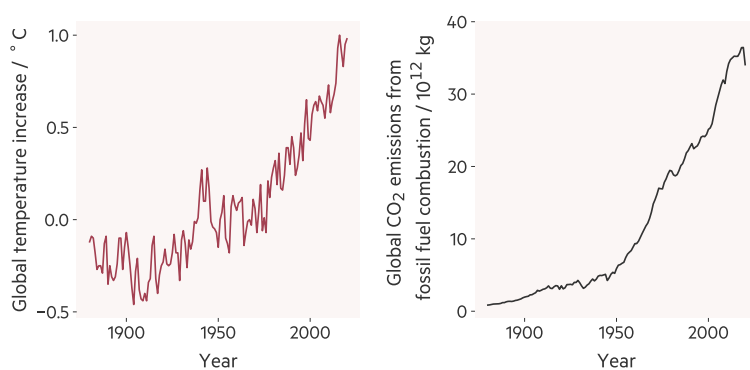


Figure 1: **Left**, variation in global land and ocean surface temperature from 1880 to 2020, based on temperature departure from the average 20th century temperatures [1]. **Right**, historical carbon dioxide emissions from global fossil fuel combustion and industrial processes from 1880 to 2020 [2].

The world stands on the brink of irreversible ecological collapse [3]; it has been posited that anthropogenic action has put Earth on track to its sixth great mass extinction [4, 5]. One major factor contributing to this situation is the continued high consumption of fossil fuels by industrialised nations. The combustion of fossil fuels produces greenhouse gases, such as CO₂, which are well known to be a driving factor behind a global rise in temperature (see Figure 1). This global heating effect has already begun causing climate instability such as an increased frequency of extreme weather events including wildfires and floods [6–8], and appears to be a driving factor behind potentially catastrophic changes in the global climate such as the collapse of the Gulf Stream [9]. Figure 2 shows the change in CO₂ emissions for a range of global regions between 1990 and 2017. Despite a modest decrease from some nations, overall, global CO₂ emissions continue to increase. Bold action is required to prevent the worst outcomes of climate collapse.

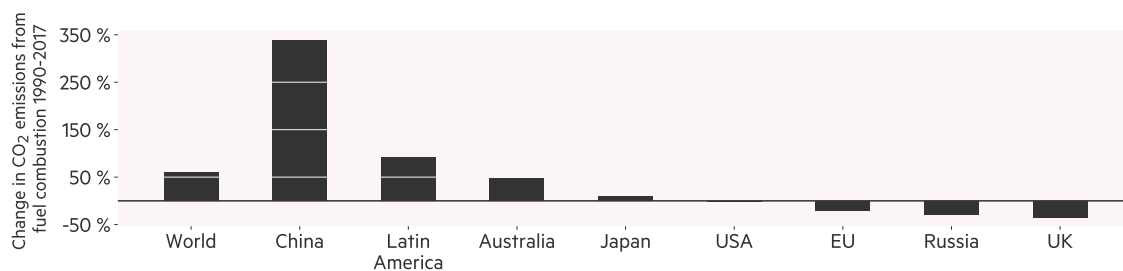


Figure 2: Increase in CO₂ emissions from fuel combustion worldwide between 1990 and 2017, by indicated region [10].

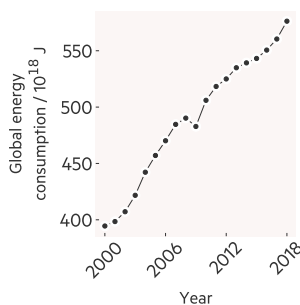


Figure 3: Primary energy consumption worldwide from 2000 to 2019 [18].

There is an apparent lack of public and political appetite for widespread reductions in energy consumption, illustrated by Figure 3, which shows a clear upward trend in global energy usage per year between 2000 and 2018, despite predictions from as early as the 19th century of rising temperatures associated with increased fossil fuel consumption [11]. This consistent increase in energy consumption perhaps stems from so-called “optimism-bias” observed in humans, where one assumes the worst outcomes of a disaster will not affect them personally [3, 12], or possibly the politicisation of positive climate action [13–16]. Whatever the cause, without a change in mindset leading to a major shift in either primary energy sources, or large reductions in energy usage—or ideally, both—this situation will eventually become unsalvageable [17]. The strategy that most governments seem to be pursuing is turning to sources of energy that do not produce greenhouse gases so as to maintain ever-increasing energy consumption while preventing further CO₂ emissions.

A global transition to low-carbon primary energy sources requires accompanying advances in effective energy storage, primarily because renewable energy sources that are not geographically restricted, such as solar and wind power, are typified by their reliance on inconsistent weather patterns. Mass uptake of these energy sources coupled with effective storage could end our reliance on fossil fuels by building a resilient low-carbon grid [19–21]. A particularly promising energy storage solution is lithium-ion batteries; the faith global governments have in such technology is evidenced by the widespread growth in large battery research consortia [22, 23]. Lithium-based electrochemical energy storage materials are the focus of this dissertation, and we will discuss some of the opportunities and challenges presented by their continued development in the next chapter.

Bibliography

- (1) National Centers for Environmental information, Climate at a Glance, www.ncdc.noaa.gov/cag/, accessed 25/01/2021.
- (2) Friedlingstein, P. et al. *Earth Syst. Sci. Data* **2020**, *12*, 3269–3340.
- (3) Bradshaw, C. J. A. et al. *Front. Conserv. Sci* **2021**, *1*, 615419.
- (4) Barnosky, A. D.; Matzke, N.; Tomiya, S.; Wogan, G. O. U.; Swartz, B.; Quental, T. B.; Marshall, C.; McGuire, J. L.; Lindsey, E. L.; Maguire, K. C.; Mersey, B.; Ferrer, E. A. *Nature* **2011**, *471*, 51–57.
- (5) Ceballos, G.; Ehrlich, P. R.; Dirzo, R. *Proc. Natl. Acad. Sci.* **2017**, *114*, E6089–E6096.

- (6) Sippel, S.; Meinshausen, N.; Fischer, E. M.; Székely, E.; Knutti, R. *Nat. Clim. Change* **2020**, *10*, 35–41.
- (7) Abatzoglou, J. T.; Williams, A. P. *Proc. Natl. Acad. Sci.* **2016**, *113*, 11770–11775.
- (8) Van der Wiel, K.; Kapnick, S. B.; van Oldenborgh, G. J.; Whan, K.; Philip, S.; Vecchi, G. A.; Singh, R. K.; Arrighi, J.; Cullen, H. *Hydrol. Earth Syst. Sci. Discuss.* **2017**, *21*, 897–921.
- (9) Boers, N. *Nat. Clim. Chang.* **2021**, *11*, 680–688.
- (10) CO₂ Emissions from Fuel Combustion: Overview, www.iea.org/reports/co2-emissions-from-fuel-combustion-overview, accessed 25/01/2021.
- (11) Arrhenius, S. *Lond. Edinb. Dublin Philos. Mag. J. Sci.* **1896**, *41*, 237–276.
- (12) Bavel, J. J. V. et al. *Nat. Hum. Behav.* **2020**, *4*, 460–471.
- (13) Gustafson, A.; Rosenthal, S. A.; Ballew, M. T.; Goldberg, M. H.; Bergquist, P.; Kotcher, J. E.; Maibach, E. W.; Leiserowitz, A. *Nat. Clim. Change* **2019**, *9*, 940–944.
- (14) Burck, J., *Climate Change Performance Index Results 2017*; Germanwatch Nord-Süd Initiative e.V: Bonn, 2016.
- (15) Venâncio, M. D.; Pope, K.; Sieber, S. *Nature* **2018**, *563*, 5–6.
- (16) Hejny, J. *J. Environ. Stud.* **2018**, *8*, 197–211.
- (17) Rhodes, C. *J. Sci. Prog* **2019**, *102*, 73–87.
- (18) BP statistical review of world energy, 2020.
- (19) Dunn, B.; Kamath, H.; Tarascon, J.-M. *Science* **2011**, *334*, 928–935.
- (20) Thackeray, M. M.; Wolverton, C.; Isaacs, E. D. *Energy Environ. Sci.* **2012**, *5*, 7854.
- (21) Tian, Y.; Zeng, G.; Rutt, A.; Shi, T.; Kim, H.; Wang, J.; Koettgen, J.; Sun, Y.; Ouyang, B.; Chen, T.; Lun, Z.; Rong, Z.; Persson, K.; Ceder, G. *Chem. Rev.* **2020**.
- (22) “Business Secretary announces founding partners of £65 million battery technology research institution”, bit.ly/366Fyq0, accessed 23/01/2021.
- (23) “BATTERY 2030+ – large-scale European initiative for battery research starts up”, bit.ly/3sPEKj9, accessed 23/01/2021.

Lithium batteries

1.1 The state of the art & material bottlenecks

Lithium's low weight and electropositivity contribute to the relatively high *energy density* of lithium-based energy storage: lithium batteries are able to deliver a large amount of energy for an acceptable weight or volume "cost". This high energy density has enabled the widespread uptake of evermore impressive portable electronics powered by lithium-based electrochemical energy storage. In many ways, however, elemental lithium is ill-suited to being directly incorporated into a battery: it is highly reactive in atmospheric conditions making it difficult and dangerous to process on a large scale and batteries with lithium-metal components tend to exhibit very poor performance over multiple electrochemical cycles [1–3]. These issues have been circumvented by the development of *intercalation* batteries, which function via transfer of lithium ions to and from host electrodes, in which the intercalant (Li^+) moves in and out of the structure without affecting the structural integrity of the electrode material [4, 5].¹

Intercalation materials are crystalline structures with relatively open channels through which intercalant ions can migrate. One archetypal intercalation material is the carbon allotrope graphite, which is comprised of two-dimensional "honeycomb" layers of covalently-bonded carbon atoms with adjacent layers held together by Van der Waals interactions (Figure 1.1). The intercalant can be accommodated between the C_6 layers and reversibly removed to recover pure graphite again.

Another key class of intercalation materials in the context of lithium-ion batteries are the layered transition metal dichalcogenides with the general formula MX_2 , where M is some transition metal and X is some chalcogenide. These contain layers of close-packed planes of chalcogenide ions with interstitial octahedral and tetrahedral sites. Every-other layer of octahedral interstitials is occupied by transition metal ions, with the rest left vacant. These vacant octahedral sites can host intercalant ions. The generalised structure of layered MX_2 materials is shown in Figure 1.2.

For the purposes of this work, we consider each battery cell to be comprised of three components: two electrodes, the cathode and the anode;

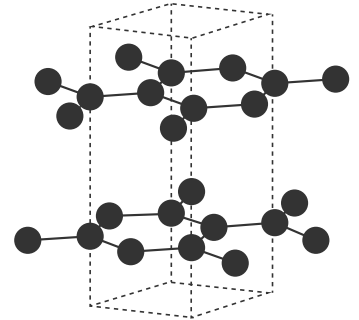


Figure 1.1: Structure of graphite. Carbon atoms are shown in grey, covalent bonds are indicated with solid lines. The offset layers of hexagonally arranged carbon are held together by Van der Waals forces.

¹ The intercalation mechanism, involving the storage and release of lithium ions from a host structure results in the term "lithium-ion" battery. Analogously, if a battery were to have a lithium anode, it would be termed a "lithium-metal" battery.

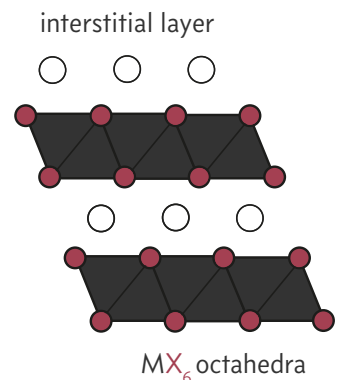


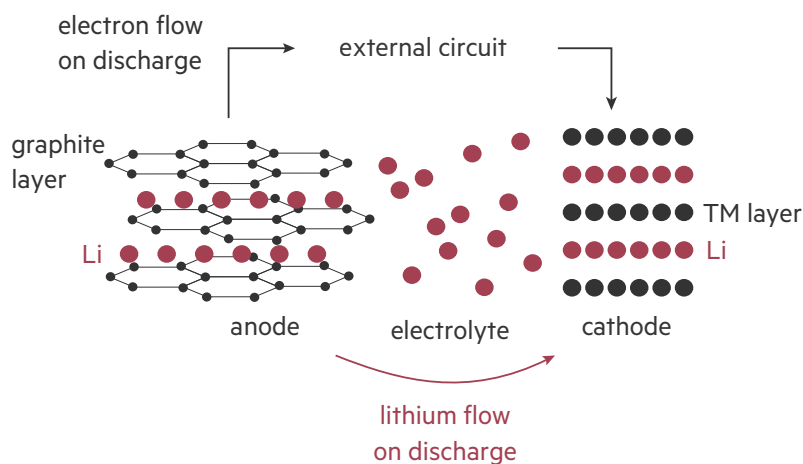
Figure 1.2: Structure of layered MX_2 . MX_6 octahedra are shown grey, with the chalcogenide ions highlighted in red. The interstitial sites that can accommodate lithium are shown with unfilled circles.

and the electrolyte. Both the anode and the cathode are intercalation compounds—typically graphite and MX_2 electrodes respectively. The cathode is the material with a higher reduction potential with respect to the reference electrode of metallic lithium. During discharge, lithium ions are released at the anode and travel via the electrolyte to the cathode. The electrolyte is an electronic insulator by design, whereas the anode and cathode are electronic conductors. The electrons associated with the lithium released from the anode are forced round an external circuit where they can perform work. The free energy change on transfer of lithium from the anode to the cathode defines the maximum work that can be extracted from the battery. This mechanism is summarised schematically in Figure 1.3.

The first commercial lithium-ion battery entered the market in the early 1990s [6], enabled by John Goodenough’s characterisation of the excellent cathodic properties of layered LiCoO_2 (an example of an MX_2 intercalation material) [7]. Goodenough’s work does not stand apart from all others: the concept of a rechargeable lithium battery was first demonstrated in the 1970s by Stanley Whittingham, using lithium metal and layered TiS_2 as the anode and cathode respectively [8, 9]. While it was an exciting proof-of-concept this lithium-metal cell had poor long-term performance. A great deal of work then centered around developing battery chemistries that were resilient over many cycles, i.e., that were suitably rechargeable. This ultimately led to the development of the lithium-graphite intercalation technologies used in modern batteries originally developed by Akira Yoshino [6, 10]. The significance of this technology is reflected by the fact that Yoshino, Goodenough and Whittingham were awarded Nobel Prize for Chemistry in 2019 for the development of lithium-ion battery technology[11].

To this day, the majority of lithium-ion batteries are based around

Figure 1.3: Schematic showing the architecture of a conventional lithium-ion cell. Lithium ions move down the lithium chemical potential gradient on discharge; while charging, the reverse process is driven by an external potential. Simultaneously, electrons flow round an external circuit driven by the electronically insulating nature of the electrolyte.



LiCoO₂ or its structural analogues [12]. The discharge process of a LiCoO₂ intercalation cell can be represented as the oxidation of the lithium in the anode



and the reduction of cathode,



² The reverse reactions, driven by an external potential occur on charging. While there are multiple commercial lithium battery cathodes, they all contain transition metals—known for their variable oxidation states—that are able to reversibly accommodate electrons facilitating lithium intercalation, analogous to the process described by Equation (1.2) [12, 14–16].

Despite the success of the lithium–cobalt–oxide/graphite cells, there are ever increasing demands on the energy density of battery technology: the portable electronics industry needs smaller, lighter batteries that can run ever more powerful components; electric vehicles need to increase their single-charge range to encourage consumers to move away from petrol-based vehicles; and batteries must become more efficient for cost-effective incorporation across energy grids [17–19]. To meet these challenges research has tried to identify different lithium battery chemistries that can improve on contemporary technology. One particularly tantalising route to improved energy density is to use a lithium-metal anode, doing away with the excess weight associated with carbon in graphite-intercalation anodes [1–3].³

Conventional electrolytes represent a significant bottleneck to stabilising lithium-metal anodes. The electrolyte is typically a mixture of a lithium salt, such as LiPF₆, and an organic solvent, often a mixture of ethylene carbonate and dimethyl carbonate (EC:DMC/LiFP₆). Such electrolytes are low cost, easy to prepare, and have high ionic conductivities ($\sim 0.01 \text{ S cm}^{-1}$) [21]. On the first cycle of a lithium-metal battery, they react to form a passivating layer on the surface of lithium, which ensures the cell remains chemically stable over multiple cycles.⁴ The issues arise on subsequent cycles. Repeatedly stripping and replating a lithium metal anode does not occur homogeneously across the anode surface. Over multiple cycles these inhomogeneities grow, forming lithium *dendrites*, which can eventually provide an electrical contact between the anode and the cathode, causing the cell to short-circuit. While the factors and mechanisms that control lithium dendrite growth are somewhat more complicated than this simple picture, it remains the case that conventional

² It is not actually possible to reversibly cycle a full lithium per formula unit from a LiCoO₂ cell, some fraction of lithium will instead be intercalated/deintercalated [13]

³ Consider simple theoretical capacities of a graphite anode as compared to a lithium anode: according to the equation

$$C_{\text{specific}} = \frac{xF}{nM}, \quad (1.3)$$

where x is number of transferred electrons, F is the Faraday constant, n is the number of moles of electroactive component and M is the molecular weight of that component [20]. LiC₆ has a specific capacity of 372 mA h g^{-1} , whereas the specific capacity of lithium metal anodes are approximately an order of magnitude higher at 3860 mA h g^{-1} .

⁴ a similar layer, known as the solid-electrolyte interface, or SEI, forms on graphite anodes also

⁵ Dendrite growth also occurs in intercalation batteries, but because lithium metal is not present in these systems, lithium dissolution needs to occur via some means first, which tends to significantly delay dendrite-driven cell failure.

liquid electrolytes offer little meaningful mechanical resistance to dendrite propagation [22].⁵

These organic-solvent-based electrolytes are also highly flammable, and battery fires are a common cause of concern [23]. If battery fires occur during the operating life of the battery they can put the end user at risk. This has caused a number of media scandals for portable electronics companies [23, 24]. End-of-life battery fires are another issue. Improper disposal of flammable batteries can not only lead to fires at waste disposal sites, but also, it makes it more challenging to recycle the increasingly precious elemental components of the battery [23, 25]. These concerns are particularly acute considering it is of great interest to society to see an increase in battery usage. Additionally, the batteries that are envisaged to power grid-based energy-storage systems and cars are far larger than the majority of lithium-ion batteries used today, and this physical scale-up exacerbates the safety concerns surrounding current battery technologies [3, 17, 19, 26].

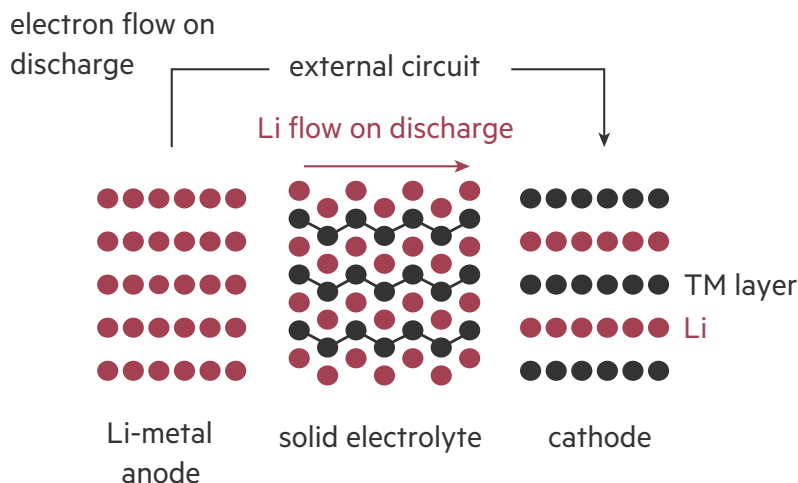
The fluid nature of liquid electrolytes also allows for the transport of species other than lithium ions. Cell degradation can occur via transition metal dissolution [27, 28]; transition metal ions can be solvated at the electrolyte-cathode interface and transported to the anode. Not only does this remove redox-active species from the cathode, reducing its ability to intercalate more lithium, but the deposited transition metal ions can take part in side reactions, which typically result in the loss of cyclable lithium [29, 30]. One final undesirable feature of fluid electrolytes we will discuss is the build-up of concentration gradients within the electrolyte. As both lithium and its counter-ion can move in a conventional electrolyte, high current densities can strongly polarise this solution: if the concentration of Li^+ counter-ion at either electrode surface reaches zero, lithium will cease to conduct and the battery will fail. Conversely, at the other electrode, if the concentration of salt becomes too high locally, it can precipitate out of the organic solvent. These processes limit—for example—the charging rate of a battery [31, 32].

In principle, all the issues outlined with these conventional electrolytes can be addressed by replacing them with a *solid-state* electrolyte [33]. Indeed this route to next-generation lithium energy storage is currently a huge area of research, which we will explore in the next section.

1.2 Solid electrolytes for next-generation energy storage

The ideal all-solid-state lithium battery offers great improvements over the current state-of-the-art lithium-ion batteries, including higher energy densities, increased safety, a wider range of operating conditions and longer

Figure 1.4: Schematic showing the architecture of a solid state lithium-metal cell. On discharge, lithium ions move through the *solid* electrolyte towards the electrode with the lower lithium chemical potential. Simultaneously, electrons flow round an external circuit owing to the electronically insulating nature of the solid electrolyte.



device lifetimes. Many of these advantages stem from the nature of solid inorganic ion conductors, which have been proposed as a replacement for conventional liquid electrolytes [27, 33].⁶ Consider the limitations of conventional electrolytes discussed in Chapter 1: there are issues surrounding dendrite propagation leading to cell failure, facilitated by the lack of mechanical resistance offered by the liquid electrolyte. Ceramic electrolytes have sufficient mechanical hardness to, in principle, suppress this growth [36]. Not only could this extend operating lifetimes of intercalation batteries, but also enable stable higher energy-density lithium-metal batteries. Additionally, solid electrolytes are typically comprised of a rigid host framework through which lithium ions can migrate [37, 38]. This framework should hold counter-ions fixed in place, preventing transition-metal dissolution and electrolyte polarisation [39]. Finally, ceramic solid electrolytes are highly thermally stable, suggesting they should be operative over a range of working conditions—such as conditions under which solvent electrolytes might freeze—and inflammable, circumventing the safety concerns with modern batteries. A schematic of an all solid-state battery is shown in Figure 1.4.

Despite this promise, solid-state batteries are yet to be widely commercially available. Solid-ion conduction was first observed by Michael Faraday in the 1830s after Alessandro Volta had shared with him the progenitor of modern batteries, the Voltaic pile [40]. It is only now, some thirty years after the commercialisation of the first lithium-ion batteries that commercial prototype solid-state batteries are beginning to be produced [41, 42]. This is because the road to lithium solid electrolytes that deliver on the promise outlined above has been long and arduous. A key reason for the late-term interest in lithium solid electrolytes was the comparatively slow development of the field of *solid state ionics*. After

⁶ All solid electrolytes discussed in this report are crystalline inorganic materials, other classes of solid electrolyte such as glasses [34] and polymer electrolytes [35] are also being investigated for commercial application.

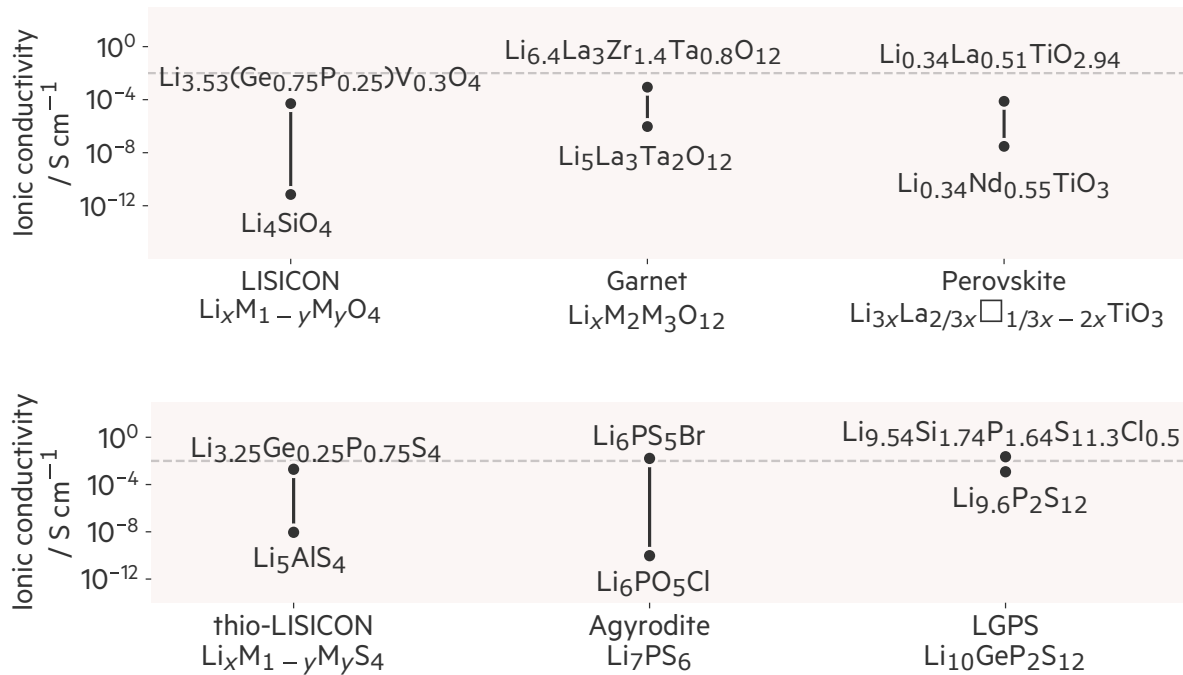


Figure 1.5: Ionic conductivities of a range of lithium solid electrolyte structural families, each with a general composition or key parent compound shown on the x -axis, as compared to the conductivity of a conventional liquid electrolyte, EC:DMC/LiFP₆, shown as a grey dashed line. The data used in this plot was taken from refs [49] and [37].

⁷ Ag₄RbI₅ itself has been used in a range of batteries [46, 47], though never deployed commercially.

early work by Faraday on the ionic conductivity of PbF₂ and Ag₂S [43] in the 19th century, it was not until the 20th century, after Carl Tubandt's characterisation of silver transport in AgI₂ in 1921 [44], that Ag₄RbI₅ was shown to have an ionic conductivity of 0.2 S cm⁻¹ in the 1960s [45]. This work set the precedent for solid ion-conductors that could be truly competitive with liquid conductors, and gave rise to the practical investigation of solid ion conductors for technological applications.⁷ Analogous lithium iodides were also investigated, and while their ionic conductivities were not considered high enough for widespread commercial deployment, LiI found use as an electrolyte in pacemaker batteries [48].

Over the subsequent decades, fast lithium ion-conductors have indeed been discovered and huge steps have been taken towards their optimisation for eventual use in a solid-state battery. One of the early promising examples was the lithium garnet Li₇La₃Zr₂O₁₂ (LLZO). First studied for battery application in 2007, the discovery of LLZO has paved the way for oxide lithium-ion conductors exhibiting fast-ion conduction ($\sim 1 \times 10^{-3}$ S cm⁻¹) [50]. Additionally, many fast-ion conducting lithium thiophosphates have been characterised as solid ion conductors, one of the most prominent perhaps being Li₁₀GeP₂S₁₂ (LGPS). First noted in 2011 [51], chemical derivatives of LGPS have now reached conductivities as high as $\sim 2.5 \times 10^{-2}$ S cm⁻¹ [52]. These are just two examples of many. Other notable materials include other oxides: perovskite based conductors [53], LISICON materials [54] and other garnets [55, 56]; and sulfide ion conductors including the agyrodites [57, 58] and thio-LISICONs

(such as LGPS) [59]. Additionally there is an exciting class of halide based lithium ion conductors [60] rediscovered as candidate solid-electrolytes after applying modern synthesis techniques to known materials [61], and some mixed anion ion-conductors such as the lithium antiperovskites [62, 63]. In addition, still more novel ion conductors are being discovered which present exciting optimisation challenges [64–66]. A range of solid lithium-ion conducting electrolyte families and their ionic conductivities are shown in Figure 1.5.

Despite their high ionic conductivities, it has not been simple to incorporate these known solid electrolytes into lithium batteries. For example, engineering suitable electrode–solid-electrolyte interfaces is highly challenging. For the few solid lithium ion conductors that are stable in contact with lithium metal, there is often a poor interface between the electrode and the electrolyte—solid electrolytes cannot “wet” the surface of lithium anode in the same way that a liquid electrolyte would, leading to high resistance at the solid-solid interface [67]. If, on the other hand, the solid electrolyte is *not* stable in contact with lithium metal, as with liquid electrolytes, reactions will occur at the interface. The products of these degradation reactions can reduce overall cell performance. The fast-lithium ion conductor LGPS, for example, degrades to Li_3P , Li_2S , and Li–Ge alloys at the Li-LGPS interface. This SEI-like layer of degradation products increases cell resistance [68].

Additionally, while the non-flammable nature of ceramics is a clear advantage over conventional electrolytes, the highly conductive sulphide solid electrolytes such as LGPS often decompose to form toxic and flammable H_2S [26, 69]. This serves as an illustration of some of the less obvious challenges of deploying solid-state batteries. Just because they are not flammable, does not mean that safety risks will not occur from products of their degradation during operation.

A final challenge involved in engineering a stable solid-state lithium cell has been lithium dendrite formation, despite the hope that the mechanical properties of solid electrolytes would suppress their growth and propagation. The widely invoked Monroe and Newman model suggests that a solid electrolyte with twice the shear modulus of lithium metal (4.8 GPa at 298 K) should prevent a dendrite-induced short-circuit [36], yet even LLZO, with a shear modulus of ~ 100 GPa [70], still seemingly cannot avoid this failure mechanism [71–73]. Counter-intuitively, polymer electrolytes with similar shear moduli to lithium metal have been engineered which can seemingly prevent dendrite growth [74], clearly showing that mechanical properties alone are not sufficient to prevent dendrite-driven cell failure, which has led to a host of dendrite formation mechanisms in ceramic electrolytes being proposed [75]. One such mechanism is dis-

cussed in Chapter 7.

All this paints a rather convoluted picture: on the one hand, solid-state batteries promise increased energy density over lithium-ion technology because their mechanical properties should suppress dendrite growth in lithium metal cells, and yet faced with the reality of an operative cell, these mechanical properties alone, clearly do not deliver. Additionally, the safety concerns around lithium-ion batteries are supposedly removed when using an inflammable ceramic electrolyte, and yet many of the fastest lithium conducting electrolytes evolve flammable, toxic gas on exposure to air and moisture. Despite this, the first prototype solid state batteries aimed at a wide market are being produced, and electronics industry giants continue to back the technology [76]. This situation is perhaps summed up best by Michael Faraday, a key enabler of both solid state ionics and battery technology, when he said

“ *But still try, for who knows what is possible.* ” [77]

A full understanding of solid-state electrolytes is clearly lacking, but their promise is great, and the weight of ongoing scientific research in this area relays a belief that the issues with these technologies can be solved. In the next chapter, we argue for a full understanding of point defect chemistry as a means to learn more about the performance of solid electrolytes, in the expectation that characterising these properties and processes will pave the way to the development of more robust lithium solid electrolytes.

Bibliography

- (1) Xu, W.; Wang, J.; Ding, F.; Chen, X.; Nasybulin, E.; Zhang, Y.; Zhang, J.-G. *Energy Environ. Sci.* **2014**, *7*, 513–537.
- (2) Lin, D.; Liu, Y.; Cui, Y. *Nat. Nanotechnol.* **2017**, *12*, 194–206.
- (3) Chen, S.; Dai, F.; Cai, M. *ACS Energy Lett.* **2020**, *5*, 3140–3151.
- (4) Whittingham, M., *Intercalation chemistry*; Academic Press: New York, 1982.
- (5) Schaffautl *J. Prakt. Chem* **1841**, *21*.
- (6) Yoshino, A. *Angew. Chem. Int.* **2012**, *51*, 5798–5800.
- (7) Mizushima, K.; Jones, P.; Wiseman, P.; Goodenough, J. *Mater. Res. Bull.* **1980**, *15*, 783–789.
- (8) Whittingham, M. S. *J. Electrochem. Soc.* **1976**, *123*, 315.
- (9) Whittingham, M. S. *Nat. Energy* **2021**, *6*, 214–214.
- (10) Yoshino, A. *Nat. Energy* **2021**, *6*, 449–449.

- (11) *Angew. Chem. Int. Ed.* **2019**, *58*, 16723–16723.
- (12) Manthiram, A.; Goodenough, J. B. *Nat. Energy* **2021**, *6*, 323–323.
- (13) Hausbrand, R.; Cherkashinin, G.; Ehrenberg, H.; Gröting, M.; Albe, K.; Hess, C.; Jaegermann, W. *Mater. Sci. Eng. B* **2015**, *192*, 3–25.
- (14) Manthiram, A. *Nat. Commun.* **2020**, *11*, 1550.
- (15) Thackeray, M. M.; Amine, K. *Nat. Energy* **2021**, *6*, 566–566.
- (16) Manthiram, A.; Goodenough, J. B. *Nat. Energy* **2021**, *6*, 844–845.
- (17) Dunn, B.; Kamath, H.; Tarascon, J.-M. *Science* **2011**, *334*, 928–935.
- (18) Thackeray, M. M.; Wolverton, C.; Isaacs, E. D. *Energy Environ. Sci.* **2012**, *5*, 7854.
- (19) Tian, Y.; Zeng, G.; Rutt, A.; Shi, T.; Kim, H.; Wang, J.; Koettgen, J.; Sun, Y.; Ouyang, B.; Chen, T.; Lun, Z.; Rong, Z.; Persson, K.; Ceder, G. *Chem. Rev.* **2020**.
- (20) Deng, D. *Energy Sci. Eng.* **2015**, *3*, 385–418.
- (21) Xu, K. *Chem. Rev.* **2004**, *104*, 4303–4418.
- (22) Liu, Y.; Liu, Q.; Xin, L.; Liu, Y.; Yang, F.; Stach, E. A.; Xie, J. *Nat. Energy*. **2017**, *2*.
- (23) Diaz, L. B.; He, X.; Hu, Z.; Restuccia, F.; Marinescu, M.; Barreras, J. V.; Patel, Y.; Offer, G.; Rein, G. *J. Electrochem. Soc.* **2020**, *167*, 090559.
- (24) Zhang, W. *Int. J. Bus. Manag.* **2020**, *15*, 68.
- (25) Gaines, L. *SMT* **2014**, *1-2*, 2–7.
- (26) Lotsch, B. V.; Maier, J. J. *Electroceramics* **2017**, *38*, 128–141.
- (27) Janek, J.; Zeier, W. G. *Nat. Energy* **2016**, *1*, 1–4.
- (28) Liu, Q.; Geng, Z.; Han, C.; Fu, Y.; Li, S.; He, Y.-b.; Kang, F.; Li, B. *J. Power Sources* **2018**, *389*, 120–134.
- (29) Amine, K.; Chen, Z.; Zhang, Z.; Liu, J.; Lu, W.; Qin, Y.; Lu, J.; Curtis, L.; Sun, Y.-K. *J. Mater. Chem.* **2011**, *21*, 17754.
- (30) Wandt, J.; Freiberg, A.; Thomas, R.; Gorlin, Y.; Siebel, A.; Jung, R.; Gasteiger, H. A.; Tromp, M. *J. Mat. Chem. A* **2016**, *4*, 18300–18305.
- (31) Krachkovskiy, S. A.; Bazak, J. D.; Werhun, P.; Balcom, B. J.; Halalay, I. C.; Goward, G. R. *J. Am. Chem. Soc.* **2016**, *138*, 7992–7999.
- (32) Yao, K. P. C.; Okasinski, J. S.; Kalaga, K.; Shkrob, I. A.; Abraham, D. P. *Energy Environ. Sci.* **2019**, *12*, 656–665.
- (33) Famprikis, T.; Canepa, P.; Dawson, J. A.; Islam, M. S.; Masquelier, C. *Nat. Mater.* **2019**, *21*, 1–14.

- (34) Cao, C.; Li, Z.-B.; Wang, X.-L.; Zhao, X.-B.; Han, W.-Q. *Front. Energy Res.* **2014**, *2*, 25.
- (35) Zhou, D.; Shanmukaraj, D.; Tkacheva, A.; Armand, M.; Wang, G. *Chem* **2019**, *5*, 2326–2352.
- (36) Monroe, C.; Newman, J. J. *Electrochem. Soc.* **2005**, 152.
- (37) Bachman, J. C.; Muy, S.; Grimaud, A.; Chang, H. H.; Pour, N.; Lux, S. F.; Paschos, O.; Maglia, F.; Lupart, S.; Lamp, P.; Giordano, L.; Shao-Horn, Y. *Chem. Rev.* **2016**, *116*, 140–162.
- (38) Zhang, Z.; Shao, Y.; Lotsch, B.; Hu, Y.-S.; Li, H.; Janek, J.; Nazar, L. F.; Nan, C.-W.; Maier, J.; Armand, M.; Chen, L. *Energy Environ. Sci.* **2018**, *11*, 1945–1976.
- (39) Takada, K. *Acta Mater.* **2013**, *61*, The Diamond Jubilee Issue, 759–770.
- (40) Volta, A. *Philos. Trans. R. Soc. Lond.* **1800**, *90*, 403–431.
- (41) *Colorado company makes progress toward the “holy grail” of electric transportation*, <https://dpo.st/3yJkXEU>, accessed 27/05/21.
- (42) *Battery startup backed by Bill Gates claims major breakthrough*, <https://bit.ly/2SB3Lkg>, accessed 27/05/21.
- (43) Faraday, M. *Philos. Trans. R. Soc. Lond.* **1839**, *129*, 1–12.
- (44) Tubandt, C. Z. *Anorg. Allg. Chem.* **1921**, *115*, 105–126.
- (45) Owens, B. B.; Argue, G. R. *Science* **1967**, *157*, 308–310.
- (46) Owens, B.; Patel, B.; Skarstad, P.; Warburton, D. *Solid State Ion.* **1983**, *9-10*, 1241–1245.
- (47) Ovsyannikov, N. A.; Nechaev, G. V.; Novikov, D. V.; Bel'mesov, A. A.; Pukha, V. E. *Russ. J. Electrochem.* **2019**, *55*, 565–572.
- (48) Owens, B. B. *J. Power Sources* **2000**, *90*, 2–8.
- (49) Ohno, S.; Banik, A.; Dewald, G. F.; Kraft, M. A.; Krauskopf, T.; Minafra, N.; Till, P.; Weiss, M.; Zeier, W. G. *Prog. Energy* **2020**, *2*, 022001–36.
- (50) Murugan, R.; Thangadurai, V.; Weppner, W. *Angew. Chem. Int. Ed.* **2007**, *46*, 7778–7781.
- (51) Kamaya, N.; Homma, K.; Yamakawa, Y.; Hirayama, M.; Kanno, R.; Yonemura, M.; Kamiyama, T.; Kato, Y.; Hama, S.; Kawamoto, K.; Mitsui, A. *Nat. Mater.* **2011**, *10*, 682–686.
- (52) Kato, Y.; Hori, S.; Saito, T.; Suzuki, K.; Hirayama, M.; Mitsui, A.; Yonemura, M.; Iba, H.; Kanno, R. *Nat. Energy* **2016**, *1*.
- (53) Yashima, M.; Itoh, M.; Inaguma, Y.; Morii, Y. *J. Am. Chem. Soc.* **2005**, *127*, 3491–3495.

- (54) Deng, Y.; Eames, C.; Fleutot, B.; David, R.; Chotard, J.-N.; Suard, E.; Masquelier, C.; Islam, M. S. *ACS Appl. Mater. Interfaces* **2017**, *9*, 7050–7058.
- (55) Cussen, E. J. *J. Mater. Chem.* **2010**, *20*, 5167.
- (56) Zeier, W. G. *Dalton Trans.* **2014**, *43*, 16133–16138.
- (57) Bai, X.; Duan, Y.; Zhuang, W.; Yang, R.; Wang, J. *J. Mater. Chem. A* **2020**, *8*, 25663–25686.
- (58) Zhou, L.; Minafra, N.; Zeier, W. G.; Nazar, L. F. *Acc. Chem. Res.* **2021**, *54*, 2717–2728.
- (59) Minafra, N.; Hogrefe, K.; Barbon, F.; Helm, B.; Li, C.; Wilkening, H. M. R.; Zeier, W. G. *Chem. Mater.* **2021**, *33*, 727–740.
- (60) Li, X.; Liang, J.; Yang, X.; Adair, K. R.; Wang, C.; Zhao, F.; Sun, X. *Energy Environ. Sci* **2020**, *13*, 1429–1461.
- (61) Asano, T.; Sakai, A.; Ouchi, S.; Sakaida, M.; Miyazaki, A.; Hasegawa, S. *Adv. Mater.* **2018**, *30*, e1803075.
- (62) Zhao, Y.; Daemen, L. L. *J. Am. Chem. Soc.* **2012**, *134*, 15042–15047.
- (63) Dawson, J. A.; Famprakis, T.; Johnston, K. E. *J. Mater. Chem. A* **2021**, *9*, 18746–18772.
- (64) Morscher, A.; Dyer, M. S.; Duff, B. B.; Han, G.; Gamon, J.; Daniels, L. M.; Dang, Y.; Surta, T. W.; Robertson, C. M.; Blanc, F.; Claridge, J. B.; Rosseinsky, M. J. *Chem. Mater.* **2021**, *33*, 2206–2217.
- (65) Kaup, K.; Bishop, K.; Assoud, A.; Liu, J.; Nazar, L. F. *J. Am. Chem. Soc.* **2021**, *143*, 6952–6961.
- (66) Zhou, L.; Kwok, C. Y.; Shyamsunder, A.; Zhang, Q.; Wu, X.; Nazar, L. F. *Energy Environ. Sci.* **2020**, *13*, 2056–2063.
- (67) Krauskopf, T.; Richter, F. H.; Zeier, W. G.; Janek, J. *Chem. Rev.* **2020**, *120*, 7745–7794.
- (68) Wenzel, S.; Randau, S.; Leichtweiß, T.; Weber, D. A.; Sann, J.; Zeier, W. G.; Janek, J. *Chem. Mater.* **2016**, *28*, 2400–2407.
- (69) Sahu, G.; Lin, Z.; Li, J.; Liu, Z.; Dudney, N.; Liang, C. *Energy Environ. Sci.* **2014**, *7*, 1053–1058.
- (70) Ni, J. E.; Case, E. D.; Sakamoto, J. S.; Rangasamy, E.; Wolfenstine, J. B. *J. Mater. Sci.* **2012**, *47*, 7978–7985.
- (71) Pesci, F. M.; Brugge, R. H.; Hekselman, A. K. O.; Cavallaro, A.; Chater, R. J.; Aguadero, A. *J. Mater. Chem. A* **2018**, *6*, 19817–19827.
- (72) Han, F.; Westover, A. S.; Yue, J.; Fan, X.; Wang, F.; Chi, M.; Leonard, D. N.; Dudney, N. J.; Wang, H.; Wang, C. *Nat. Energy* **2019**, *4*, 187–196.

- (73) Barai, P.; Ngo, A. T.; Narayanan, B.; Higa, K.; Curtiss, L. A.; Srinivasan, V. *J. Electrochem. Soc.* **2020**, *167*, 100537.
- (74) Khurana, R.; Schaefer, J. L.; Archer, L. A.; Coates, G. W. *J. Am. Chem. Soc.* **2014**, *136*, 7395–7402.
- (75) Cao, D.; Sun, X.; Li, Q.; Natan, A.; Xiang, P.; Zhu, H. *Matter* **2020**, *3*, 57–94.
- (76) Lee, Y.-G. et al. *Nat. Energy* **2020**, *5*, 299–308.
- (77) Jones, B.; Faraday, M., *The Life and Letters of Faraday*; Cambridge University Press: 2009.

Point defects in solid electrolytes

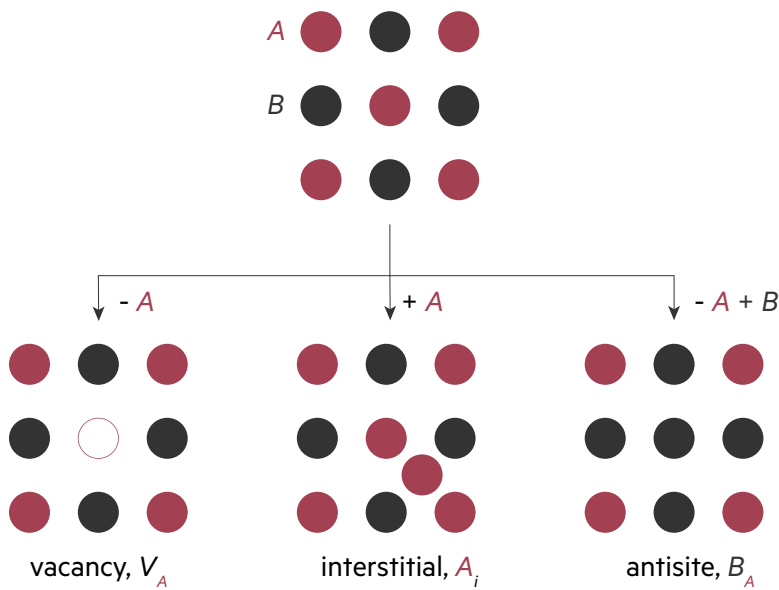


Figure 2.1: intrinsic point defects on a 2D lattice: a vacancy, an ion missing from its lattice site; an interstitial, an ion sitting on a site that does not constitute a formal lattice site; an antisite, an ion that has substituted for the species which usually occupies that site.

Crystals contain microscopic deviations from their underlying symmetry because of the entropic contribution of such defects to the free energy [1]. Defects that can be spatially associated with a single crystallographic site, or interstitial position between crystallographic sites, are termed *point defects*.¹ Examples of point defects include vacancies, a missing atom; interstitials, a species filling a void between crystallographic sites; or an antisite defect, a species that occupies a site with which it is not formally associated with.² These are all intrinsic defects and are illustrated in Figure 2.1. A dopant ion, whether it occupies an interstitial site, or replaces a native ion, is referred to as an extrinsic defect [1].

2.1 Defect engineering

Defect engineering, i.e., tailoring the nature and populations of point defects present in a material via different doping or synthesis strategies, can be used to optimise the performance of solid electrolytes. The classical pic-

¹ For the purposes of this dissertation, unless otherwise stated, the term defect refers to point (as opposed to extended) defects, and defects are discussed for the case of systems with a finite band gap (as opposed to metals).

² We highlight that sometimes an antisite is considered as a pair of substitutional defects, i.e. $X_Y + Y_X$. Throughout this work, we would refer to this as two antisite point defects as opposed to a single antisite.

ture of ion transport in solid electrolytes involves the continuous creation and annihilation of mobile-ion point defects in a percolating network [2]. These defects can either be transient, thermally generated defects or persistent defects created by off-stoichiometry in the host material. This off-stoichiometry may be intrinsic, i.e, a result of specific synthesis conditions, or a result of extrinsic doping. Within this defect-mediated transport model, the concentration of mobile defects, $[X_{\text{mobile}}]$, strongly affects ionic conductivity, σ_{ionic} ,

$$\sigma_{\text{ionic}} = [X_{\text{mobile}}]q\mu_X^{\text{mob}}. \quad (2.1)$$

In the above equation, q is the carrier-charge and μ_X^{mob} is the mobility of mobile-ion defects [3]. Attempts to optimise the ionic conductivity of solid-state electrolytes via defect engineering therefore often target increased concentrations of mobile-ion defects, $[X_{\text{mobile}}]$, or an increased mobility of the mobile ions μ_X^{mob} .

2.1.1 Increasing the concentration of mobile defects

One common strategy for increasing the concentration of mobile-ion defects is *aliovalent doping*. Aliovalent doping involves the substitution of native ions for extrinsic species of unlike charge. In solid electrolyte materials, it is typically assumed that aliovalent doping strategies drive the formation of charge-compensating mobile-ion vacancies or interstitials [4–8]. For example, silicon doping in the sodium-ion solid electrolyte Na_3PS_4 has been suggested to drive an increase in sodium interstitial concentration: substituting Si^{4+} for P^{5+} —a *subvalent* doping strategy—forms a Si_i^{\bullet} defect which is expected to be charge compensated by the formation of a Na_i^{\bullet} defect. A sufficient Si doping concentration is therefore expected to lead to meaningful increases in ionic conductivity via an increase of $[X_{\text{mobile}}]$ in Equation (2.1) [9, 10]. Doping Na_3PS_4 with chlorine to form Cl_s^{\bullet} defects or tungsten to form W_p^{\bullet} —*supervalent* doping—is similarly predicted to increase $[V'_{\text{Na}}]$ and therefore increase ionic conductivity. Both doping strategies have been shown to successfully increase Na-ion conductivity in Na_3PS_4 [9–12].

In LLZO, supervalent doping is broadly compensated by an increase in $[V'_{\text{Li}}]$, or equivalently a reduction in total lithium content. Not only does this increase the concentration of mobile-ion defects, but it has been argued reducing the lithium content causes a “frustration” in the geometric arrangement of lithium ions. This frustration stabilises the high-conductivity cubic phase relative to the low conductivity tetragonal phase as the lithium can no longer order in a way that is commensurate with the underlying structural symmetry, reducing the enthalpic stabilisation

of the tetragonal phase from lithium ordering [13]. This illustrates how changing the mobile-ion defect concentration can have implications for solid electrolyte performance beyond increases in the ionic conductivity via Equation (2.1).

2.1.2 Defect-driven carrier mobility changes

Varying the supervalent dopant species used to achieve a stable cubic-LLZO sample can have a notable effect on the distribution of lithium. This is true even in instances where the dopants share the same formal charge, such as Al^{3+} and Ga^{3+} used to form, e.g. $\text{Al}_{\text{Li}}^{\bullet\bullet}$ [14, 15]. Observations such as these imply that defect engineering, whether intentionally or otherwise, can also be used to modulate the underlying potential energy surface for mobile-ion transport in addition to tailoring the number of ionic charge carriers. In other words, rather than increasing $[X_{\text{mobile}}]$, we can target an increased value of μ_X^{mob} .³

Defect-driven modulations to the potential energy surface for mobile-ion transport can either be due to structural effects or interatomic interactions between stationary framework defects and mobile-ion defects. For example, intrinsic P_{Ge} antisites in LGPS cause local structural rearrangements which create “body-centred cubic-like” motifs and seem to increase lithium-ion conductivity [19, 20]. Body-centre cubic ion percolation networks have been noted as a key feature of high ionic conductivity lithium electrolytes as it allows for transport via a percolating network of tetrahedral sites, as opposed to alternating octahedral–tetrahedral hops. Alternating octahedral–tetrahedral hops are typically associated with higher energy intermediate positions, and therefore higher barriers for ion hopping [21]. It is also possible that this increase in lithium-ion conductivity observed on intrinsic antisite defect formation in LGPS is related to an increase in mobile ion conductivity often observed in solid electrolytes on increasing host-framework antisite disorder [22–25]. For example, based on *ab initio* molecular dynamics studies (AIMD) of the lithium agyrodite $\text{Li}_6\text{PS}_5\text{Br}$, Sadowski and Albe have proposed that $\text{Br}_{\text{S}}^{\bullet}$ antisites introduce an electrostatic perturbation which cause the formation of mobile lithium interstitials (and bound vacancies) activating long-range transport which is not observed in the anion-ordered system [26].

Of course, more direct electrostatic interactions between framework defects and mobile ion defects can also affect ion transport in solid electrolytes. For example an electrostatic “trapping” interaction between O'_{Cl} and Li_i^{\bullet} defects in the lithium antiperovskite ion conductor Li_3OCl are predicted to slow lithium ion-conductivity [5, 27]. A more subtle electrostatic interaction that we investigate directly in this dissertation (see

³ Doping strategies which directly substitute for the mobile ion, in this case lithium, have also been suggested to negatively impact the total ionic conductivity: sufficiently high concentrations of dopant will begin to block lithium transport if this substitution occurs within the percolation network [16, 17]. This can increase the *tortuosity* of lithium transport and decrease the fraction of lithium which is connected to the macroscopic transport network [18].

Chapter 8) is the so-called solid-electrolyte *inductive-effect*. This solid-electrolyte inductive-effect is often invoked to explain anomalous ionic conductivity trends in solid electrolyte materials including $\text{Na}_{11}\text{Sn}_2\text{PnS}_{12}$ ($\text{Pn} = \text{P}, \text{Sb}$) [28], $\text{Na}_3\text{P}_{1-x}\text{As}_x\text{S}_4$ [29], $\text{Li}_{4-x}\text{Sn}_{1-x}\text{Sb}_x\text{S}_4$ [30], and $\text{LiM}_2(\text{PO}_4)_3$ ($M = \text{Zr}, \text{Sn}$) [31]. This model stems from a growing base of evidence that the seemingly anomalous reduction in ionic conductivity on isovalent doping of Sn^{4+} for Ge^{4+} in LGPS could be explained by a differing electronegativities of germanium and tin. This model argues that a more electronegative cation (in this case Ge^{4+}), will draw more electron density from the sulfur ions, weakening the $\text{S}^{2-} - \text{Li}^+$ interaction, relative to a less electronegative cation (Sn^{4+}). The result is a reduced activation barrier for single lithium-ion hopping in the germanium system, or rather an increased value of μ_X^{mob} in Equation (2.1) relative to the tin system [32, 33].

2.2 Calculating defect concentrations

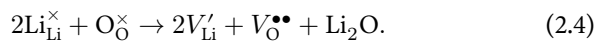
To understand what defects are important in impacting the material properties of solid electrolytes, we must ascertain which defects are present in high enough concentration to meaningfully impact performance. The concentration of a given defect is a function of its formation energy, $\Delta E_f^{X^q}$; the concentration of defect X in charge state q is given by

$$[X^q] = N_X g_{X^q} \exp\left(\frac{-\Delta E_f^{X^q}}{k_B T}\right) \quad (2.2)$$

where N_X is the density of sites on which the defect could form, g_{X^q} is the intrinsic degeneracy of the defect (e.g. spin degeneracy) [34], k_B is the Boltzmann constant, and T is the temperature. When studying the defect properties of crystalline materials it is common practice to calculate the energies of charge-neutral defect reactions such as the formation of a Frenkel pair, or a Schottky defect [5, 6, 27, 35, 36]. Taking Li_2O as an example, the formation of a lithium Frenkel pair, a stoichiometry-preserving vacancy–interstitial pair for a constituent element, is written as,



The formation of the Schottky pair, is written as,



It is clear that these reactions have a common product, V'_{Li} , and therefore they are thermodynamically coupled when forming in the same system. This coupling means we cannot reliably quantify defect concentrations

within a model in which all defects form in charged balanced reactions. For example, in the synthesis of an oxide conductor, if we alter the oxygen partial pressure during synthesis, it will change the formation energy of the oxygen vacancy [37], as this will change the Schottky pair formation energy, and both the Schottky and Frenkel pair share V'_{Li} as a common product, this must also affect the thermodynamic equilibrium of the Frenkel pair formation reaction.⁴

Instead of deriving charge-neutral defect reactions from chemical intuition and calculating their reaction energies, it is possible to calculate the formation energies of all point defects as a function of atomic chemical potentials during synthesis (or other representative conditions) [38]. In the general case, the formation energy of defect X in charge state q , is given by

$$\Delta E_f^{X^q} = E^{X^q} - E_{\text{host}} + \sum_i n_i \mu_i + q E_{\text{Fermi}}. \quad (2.5)$$

In the above, $E^{X^q} - E_{\text{host}}$ is the energy difference between defective and host materials, $\sum n_i \mu_i$ accounts for the energy cost to exchange n atoms of kind i with their reservoir chemical potential μ_i .⁵ μ_i is set by synthesis conditions (see Section 4.1.2). q and E_{Fermi} denote the defect charge state and the Fermi level respectively.⁶ This term is the electronic analogy of the previous term, and represents the energy cost for exchanging q elemental charges with the electronic chemical potential [38].⁷ The appropriate value of E_{Fermi} is derived by observing the condition of charge neutrality.

Determining the equilibrium Fermi energy consists of finding a self-consistent solution to Equation (2.2) for all defect species, under the constraint of overall charge neutrality at a given set of μ_i [39]. The condition of charge neutrality can be expressed as

$$0 = \sum_{X^q} q[X^q] + [e'] - [h^\bullet]. \quad (2.6)$$

The first term is the sum over the charge contributions from all defects, $[e']$ is the concentration of free electrons, and $[h^\bullet]$ the concentration of free holes. Electron and hole concentrations (which will be small, but cannot be assumed to be negligible in solid-state electrolytes [40–43]) are calculated as functions of the Fermi energy and the bulk density of states $g(E)$,

$$[e'] = \int_{E_g}^{\infty} \frac{1}{\exp[(E - E_{\text{Fermi}})/k_B T] + 1} g(E) dE \quad (2.7)$$

$$[h^\bullet] = \int_{-\infty}^{E_{\text{vbm}}} 1 - \frac{1}{\exp[(E - E_{\text{Fermi}})/k_B T] + 1} g(E) dE. \quad (2.8)$$

Taking all this together defines a set of coupled linear equations

⁴ We stress that despite difficulties calculating coupled defect concentrations within a “defect-reaction” model, defect reactions remain a powerful tool for understanding the defect chemistry of solid-state ionic systems. In Chapter 5, we discuss how key features of the defect and doping chemistry of antiperovskite solid electrolytes in the context of ionic conductivity can be ascribed to a preference for Schottky defect formation as opposed to Frenkel defect formation in these materials.

⁵ For example, this term for defect X_Y^q is $\mu_X - \mu_Y$.

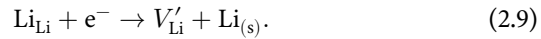
⁶ The Fermi energy is typically defined relative to the valence band maximum of the material in question, i.e. if $E_{\text{Fermi}} \approx 0$, it lies close to the valence band maximum. Alternatively, if $E_{\text{Fermi}} \approx E_g$, it lies near the conduction band minimum.

⁷ For example, for a $V_O^{\bullet\bullet}$ defect, this term would be $2E_{\text{Fermi}}$.

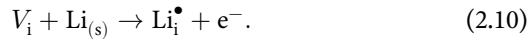
that need to be solved under the constraint of charge neutrality (Equation (2.6)) to solve for defect concentrations. In practice this can be achieved by determining the value of the Fermi energy at thermodynamic equilibrium by defining an initial value of the Fermi energy, solving Equations (2.2), (2.5), (2.7) and (2.8), assessing whether the condition of charge neutrality is met (Equation (2.6)), and if not, adjust the Fermi energy accordingly, until a satisfactory solution is found [44]. This calculation methodology often leads to this approach being labeled as determining a *self-consistent* Fermi energy. We will relate this model to a defect reactions model, and give a simple example of how we might determine the self-consistent Fermi energy in the next section.

2.3 Mapping the self-consistent Fermi energy model onto defect reactions

A hypothetical system in which only two defects of opposing charge can form can be used to show how the self-consistent Fermi energy model can reduce to a model which considers defect reactions. Consider a fictitious lithium solid electrolyte within which the only defects that can form are lithium vacancies and interstitials, or equivalently, Frenkel defects. The Frenkel-pair formation reaction can be broken down into two steps, or half-reactions: first, a lithium-ion is reduced, removed from a lattice site and moved to an external reference,



Second, a lithium atom is moved from the external reference, ionised, and occupies an interstitial site:



As reactions 2.3, 2.9 and 2.10 form a closed thermodynamic cycle, the energy of reaction 2.3 is given by the sum of the energies of reactions 2.9 and 2.10

$$\Delta E(2.3) = \Delta E(2.9) + \Delta E(2.10). \quad (2.11)$$

$\Delta E(2.9)$ and $\Delta E(2.10)$ are given by

$$\Delta E(2.9) = E_{V_{\text{Li}}'} - E_{\text{host}} + \mu_{\text{Li}} - E_{\text{Fermi}} \quad (2.12)$$

$$\Delta E(2.10) = E_{\text{Li}_{\text{i}}^{\bullet}} - E_{\text{host}} - \mu_{\text{Li}} + E_{\text{Fermi}}. \quad (2.13)$$

The first two terms in Equations (2.12) and (2.13) are the energies of the defective material and the host material respectively. μ_{Li} is the lithium

chemical potential, and E_{Fermi} the Fermi energy (c.f. Equation (2.5)). As before, the appropriate value of E_{Fermi} is derived by observing the condition of charge neutrality. In the present case where only lithium interstitials and vacancies can form, the material will be charge neutral when

$$[V_{\text{Li}}'] = [Li_i^{\bullet}] \quad (2.14)$$

in which case the Fermi energy is “pinned” at the value where⁸

$$\Delta E(2.9) = \Delta E(2.10) \quad (2.15)$$

or alternatively,

$$\Delta E_f^{V_{\text{Li}}'} = \Delta E_f^{Li_i^{\bullet}} \quad (2.16)$$

and therefore determining the Fermi energy is simply a case of solving a pair of linear simultaneous equations (see Figure 2.2).

2.4 Variable defect charge states

Until now, we have assumed that defects can only form in charge states which correspond to the charge of the atoms added to or removed from the system during defect formation, e.g., the removal of one O^{2-} results in a net positive charge of 2+, therefore, we have formed a $V_O^{\bullet\bullet}$ defect. Although solid electrolytes do not typically contain ions normally considered to have variable oxidation states⁹ this does not preclude them from containing defects with varied charge states. In Chapter 6 we discuss the variable charge state of oxygen vacancies in LLZO. Experimental work has previously noted the formation of colour centres in samples of LLZO prepared under highly reducing conditions, suggesting electrons trapped at V_O sites [45], i.e. stable $V_O^{\bullet} / V_O^{\times}$ defects. We confirm the stability $V_O^{\bullet} / V_O^{\times}$ defects under lithium-rich synthesis conditions, where the Fermi level is high, reducing the formation energies of the neutral and singly charged vacancy relative to the fully ionised defect (see Equation (2.5)) [46]. It has since been suggested that these trapped electrons could facilitate local electronic conductivity changes that could cause lithium deposits to form in the electrolyte which could eventually result in dendrite formation and cell failure [47].

Care must also be taken when assuming defect charge states in wide-bandgap oxides such as many solid electrolytes. Ionisation of such materials will often result in hole localisation on oxygen ions, corresponding to the reduction of an oxide ion from O^{II} to O^I [48, 49]. This process is observed in LLZO when calculating the properties of e.g. V_{Li} . At small values

⁸ assuming that the degeneracies of the two defects are equivalent

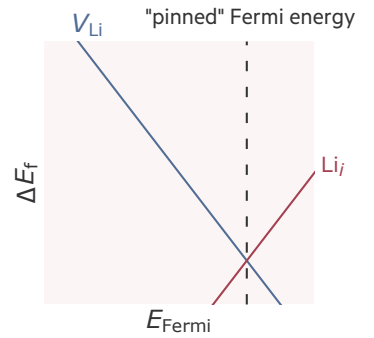


Figure 2.2: Defect formation energies as a function of Fermi energy for a system in which only lithium vacancies and interstitials can form. The vertical dashed line shows the pinned Fermi energy.

⁹ This is in part, by design, as redox active framework atoms would be associated with undesirable electronic conduction.

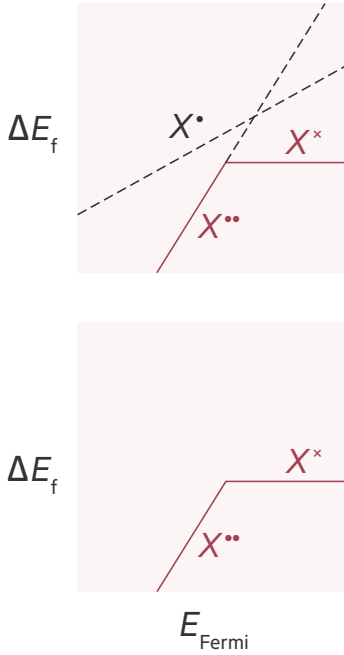


Figure 2.3: Example transition level diagram for a defect with three possible charge states: 0, +1 and +2. The **top** plot shows the $\Delta E_f^{X^q}(E_{\text{Fermi}})$ relationship for each of these charge states, the **bottom** plot shows how these data would conventionally be displayed on a transition level diagram: only the $\Delta E_f^{X^q}(E_{\text{Fermi}})$ relationship for the stable defect is shown at each value of E_{Fermi} .

of E_{Fermi} , V_{Li}^\times is stabilised relative to the “expected” V_{Li}' [46] this is because when the Fermi energy is small and the formation of negatively charged defects is disfavoured (see Equation (2.5)), and so as opposed to forming a V_{Li}' defect, the charge imbalance introduced on the formation of a lithium vacancy is accommodated by the oxidation of an oxide ion.

The potential for defects to show variable charge states suggests best practice approaches should consider a range of possible defect charge states and not just those expected from chemical intuition. The relative stability of different defect charge states can be assessed via their thermodynamic transition levels, which are defined as the energy at which the charge state of defect X transforms between q and q' , $(X, q/q')$. The transition level is calculated as

$$E(X, q/q') = \frac{\Delta E_f^{X^q} - \Delta E_f^{X^{q'}}}{q' - q}. \quad (2.17)$$

A plot of all defect formation energies, in all charge states as a function of Fermi energy is termed a transition level diagram. As these plots become increasingly difficult to interpret as more defects in more charge states are added, conventionally, one line is plotted per defect, and for any given Fermi energy, only the lowest energy charge state is shown. Figure 2.3 shows an example transition level diagram for defect X with three potential charge states, X^\times , X^\bullet and $X^{\bullet\bullet}$, of which X^\bullet is not stable at any value of E_{Fermi} .

2.5 Modelling aliovalent doping response

Studying the full point defect chemistry of a material, and modelling the aliovalent doping response provides a means to predict whether different doping strategies will prove successful in improving ionic conductivity. It can often be difficult to predict whether or not a particular aliovalent doping strategy for enhancing ionic conductivity in solid electrolytes will be successful *a priori* [50]. In Chapter 5 we discuss conditions for aliovalent doping to successfully increase the ionic conductivity of a lithium solid electrolyte in which the diffusion processes are mediated by the transport of mobile-ion defects in depth. One key condition for a successful aliovalent doping strategy discussed therein is that it should preferentially increase the concentrations of charge-carrying mobile defects ahead of immobile defects. We can assess whether this is the case by slightly modifying the methodology discussed so far in this chapter. We can include the charge contribution from a hypothetical dopant M with charge state r in

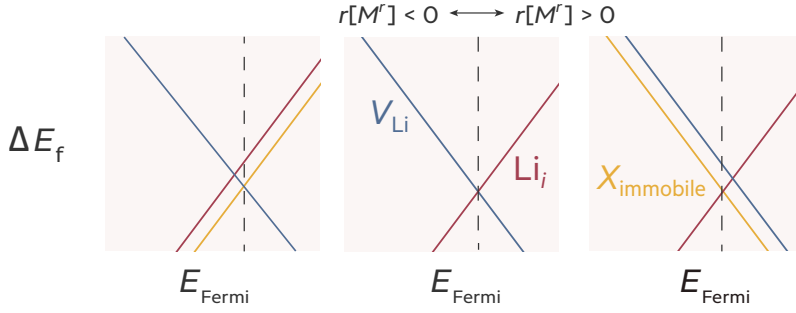


Figure 2.4: **Middle**, transition level diagram in which the Fermi energy is pinned by the formation of lithium Frenkel defects. In the absence of other complicating factors, it should be possible to dope this system to form either a lithium excess or deficit. The **left** panel shows a transition level diagram in which the Fermi energy is pinned by mobile lithium vacancies and some immobile framework defect, for example, a system in which a lithium-anion Schottky pair is lower energy than the Frenkel pair. This system could potentially be doped to achieve a lithium deficit, but doping to form a lithium excess will predominantly reduce $[V_{\text{Li}}]$ and increase $[X_{\text{immobile}}]$. The **right** panel shows a system in which the Fermi energy is pinned by lithium interstitials and a negatively charged immobile framework defect which could be doped effectively to form a lithium excess, but not a lithium deficit such as a system dominated by anti-Schottky defect chemistry.

the condition of charge neutrality, eq. (2.6),

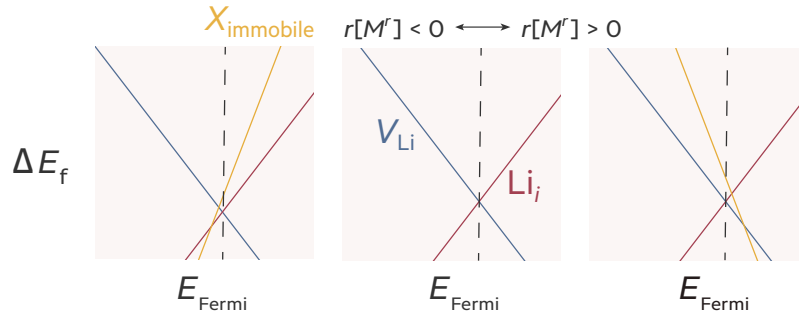
$$\rho = \sum_{X^q} q[X^q] + [e'] - [h^\bullet] + r[M^r] = 0. \quad (2.18)$$

Importantly in the dilute-defect-limit the doping response does not depend on the dopant species or insertion site, only the product $r[M^r]$. This allows us to approximate which defect concentrations change most dramatically when the material is doped on introducing a fixed concentration of dopant. If a dopant with excess charge is introduced, in effect, this adds an additional defect species to the self-consistent Fermi energy solution, which will mean that the other defect concentrations must change in order to restore charge neutrality. The formation energies of all charged defects are a function of the Fermi energy (Equation (2.5)), i.e., this doping response is not limited to mobile ion defects.

The net effect of adding a supervalent dopant is to increase the Fermi energy, which, in a lithium solid electrolyte, will indeed decrease the formation energy of the lithium vacancy and increase the formation energy of the interstitial (see Equations (2.9) and (2.10)) causing a net reduction in lithium content. Alternatively, one can increase the concentration of lithium interstitials by doping with a subvalent dopant, which will decrease the Fermi energy. However, as the Fermi energy is necessarily perturbed by the introduction of a charged dopant, the formation energy of *all* charged defects in the system must change (see Equation (2.5)), not just mobile-ion point defects. Therefore it cannot be assumed that under all accessible chemical potential synthesis regimes that a particular aliovalent doping strategy will cause an increase in ionic conductivity commensurate with the predicted change in ionic charge carrier concentration.

On doping a lithium ion solid electrolyte with dopant M with relative

Figure 2.5: The **middle** panel shows a transition level diagram in which the Fermi energy is pinned by lithium Frenkel defect formation. The **left** panel shows the same, however, an immobile defect X^q where $q > 1$ is lower energy at lower values of E_{Fermi} , and as such, after doping to form a lithium excess, eventually, this defect will form in preference to the lithium interstitial, reducing the expected increase in total lithium content. The **right** panel shows the opposite situation to the left hand panel: some defect $X^{q<-1}$ becomes lower energy at high values of E_{Fermi} , complicating the response to a doping strategy designed to reduce the total lithium content.



charge r , to assume

$$[M^r] \approx r[V_{\text{Li}}'] \quad (2.19)$$

where $r > 0$ and,

$$[M^r] \approx r[\text{Li}_i^\bullet] \quad (2.20)$$

where $r < 0$ is only appropriate if the Fermi energy is pinned by mobile-ion Frenkel disorder under all relevant synthesis chemical potential regimes.¹⁰ This cannot be guaranteed, and in the complex ternary or quaternary chemical space that many solid electrolytes inhabit, immobile defects with similar formation energies to mobile ion defects will “compete” to neutralise the dopant charge [46]. For example, in a material in which the Fermi level is pinned by the formation of a Schottky pair as opposed to the Frenkel pair, anion vacancies will form in preference to the lithium interstitial on subvalent doping. In LGPS, under many synthesis conditions, $\text{P}_{\text{Ge}}^\bullet$ defects have a lower formation energy than Li_i^\bullet defects at relevant Fermi energies [19, 20]. Under such conditions in LGPS, the predominant response to introducing a net negative charge via doping will be to form immobile framework defects as opposed to increasing the concentration of mobile ion point defects. These considerations are represented pictorially in Figure 2.4.

In Chapter 6, we discuss how in LLZO, under all synthesis conditions, the Fermi energy is pinned by Frenkel disorder, however, under select synthesis conditions, the formation energy of Li_{Zr}''' antisite is low enough such that an increase in Fermi energy will reduce its formation energy as to be lower than that of the V_{Li}' defect. As the gradient of the defect-formation-energy–Fermi-energy relationship is given by the defect charge (see Equation (2.5) or Figure 2.3), any increase in Fermi energy will reduce the formation energy of the Li_{Zr}''' defect by three times the amount that the lithium vacancy formation energy will be decreased by. In other words, even if a small amount of dopant causes a reduction in lithium con-

¹⁰ An example of this is Na_3PS_4 : as previously discussed both doping for interstitials and vacancies has proved successful in increasing ionic conductivity and theoretical studies of defects in Na_3PS_4 find that the Fermi energy is pinned by Frenkel disorder under all conditions [43].

tent, this will shortly be offset by an increase in $[Li_{Zr}''']$ on further doping [46], this scenario is outlined in Figure 2.5. All this said, it may be that the defect formation energies as a function of Fermi energy are such that approximations (19) and (20) hold, but this cannot be known for certain without modelling the defect response to doping. The approach outlined in this section should allow us to predict what doping strategies will be more effective for modulating the concentrations of mobile ion defects.

2.6 Closing remarks

The bulk of the original work in this thesis involves applying the methodologies discussed above to a variety of solid electrolytes:

- In Chapter 5, we establish the native defect chemistry of the lithium solid electrolyte Li_3OCl and model the response of the native defect concentrations to both supervalent and subvalent doping to compare the efficacy of the two doping strategies for improving ionic conductivity.
- In Chapter 6, we take a similar approach as we did for Li_3OCl to investigate the defect chemistry of LLZO, paying special attention to the defect chemistry of oxygen vacancies which have previously been proposed as having an impact on the total conductivity of LLZO [51].
- In Chapter 7 we extend our study of the defect chemistry of LLZO to examine how the defect chemistry affects *electronic* conductivity, which has been implicated in dendrite-driven failure mechanisms in LLZO based solid state batteries [40].
- Finally, in Chapter 8, we examine alterations to the mobile-ion defect mobility as a consequence of the solid electrolyte inductive effect in Sn-doped LGPS.

The next two chapters discuss the basics of the theory and methodology behind the quantum-mechanical approaches used to calculate the necessary inputs for the equations laid out in this chapter such as the defect formation energies. This is then followed by a discussion of some ancillary methodology used to further analyse the implications of the the presence of point defects in the materials studied.

Bibliography

- (1) West, A., *Basic solid state chemistry*; John Wiley & Sons: New York, 1999.
- (2) Howard, R. E.; Lidiard, A. B. *Rep. Prog. Phys.* **1964**, *27*, 161–240.

- (3) Famprikis, T.; Canepa, P.; Dawson, J. A.; Islam, M. S.; Masquelier, C. *Nat. Mater.* **2019**, *18*, 1278–1291.
- (4) Brugge, R.; Kilner, J.; Agüadero, A. *Solid State Ion.* **2019**, *337*, 154–160.
- (5) Li, P.; Hussain, F.; Cui, P.; Li, Z.; Yang, J. *Phys. Rev. Mater.* **2019**, *3*, 115402.
- (6) Clarke, M. J.; Dawson, J. A.; Mays, T. J.; Islam, M. S. *ACS Appl. Energy Mater.* **2021**, *4*, 5094–5100.
- (7) Kraft, M. A.; Gronych, L. M.; Famprikis, T.; Zeier, W. G. *ACS Appl. Energy Mater.* **2021**, *4*, 7250–7258.
- (8) Fuchs, T.; Culver, S. P.; Till, P.; Zeier, W. G. *ACS Energy Lett.* **2019**, *5*, 146–151.
- (9) Zhu, Z.; Chu, I.-H.; Deng, Z.; Ong, S. P. *Chem. Mater.* **2015**, *27*, 8318–8325.
- (10) Tanibata, N.; Noi, K.; Hayashi, A.; Tatsumisago, M. *RSC Adv.* **2014**, *4*, 17120–17123.
- (11) Yu, C.; Ganapathy, S.; de Klerk, N. J. J.; van Eck, E. R. H.; Wage-maker, M. *J. Mat. Chem. A* **2016**, *4*, 15095–15105.
- (12) Fuchs, T.; Culver, S. P.; Till, P.; Zeier, W. G. *ACS Energy Lett.* **2019**, *5*, 146–151.
- (13) Kozinsky, B.; Akhade, S. A.; Hirel, P.; Hashibon, A.; Elsässer, C.; Mehta, P.; Logeat, A.; Eisele, U. *Phys. Rev. Lett.* **2016**, *116*, 055901.
- (14) Rettenwander, D.; Redhammer, G.; Preishuber-Pflügl, F.; Cheng, L.; Miara, L.; Wagner, R.; Welzl, A.; Suard, E.; Doeff, M. M.; Wilkening, M.; Fleig, J.; Amthauer, G. *Chem. Mater.* **2016**, *28*, 2384–2392.
- (15) Daza, F. A. G.; Bonilla, M. R.; Llordés, A.; Carrasco, J.; Akhmatkaya, E. *ACS Appl. Mater. Interfaces* **2018**, *11*, 753–765.
- (16) Allen, J. L.; Wolfenstine, J.; Rangasamy, E.; Sakamoto, J. *J. Power Sources* **2012**, *206*, 315–319.
- (17) Mukhopadhyay, S.; Thompson, T.; Sakamoto, J.; Huq, A.; Wolfenstine, J.; Allen, J. L.; Bernstein, N.; Stewart, D. A.; Johannes, M. D. *Chem. Mater.* **2015**, *27*, 3658–3665.
- (18) O’Rourke, C.; Morgan, B. *J. Open Source Softw.* **2019**, *4*, 1306.
- (19) Oh, K.; Chang, D.; Lee, B.; Kim, D. H.; Yoon, G.; Park, I.; Kim, B.; Kang, K. *Chem. Mater.* **2018**, *30*, 4995–5004.
- (20) Gorai, P.; Long, H.; Jones, E.; Santhanagopalan, S.; Stevanović, V. *J. Mat. Chem. A* **2020**, *8*, 3851–3858.

- (21) Wang, Y.; Richards, W. D.; Ong, S. P.; Miara, L. J.; Kim, J. C.; Mo, Y.; Ceder, G. *Nat. Mater.* **2015**, *14*, 1026–1031.
- (22) Hull, S.; Keen, D. A.; Madden, P. A.; Wilson, M. *J. Phys.: Condens. Matter* **2007**, *19*, 406214.
- (23) Gombotz, M.; Hanghofer, I.; Eisbacher-Lubensky, S.; Wilkening, H. *Sol. Stat. Sci.* **2021**, *118*, 106680.
- (24) Gautam, A.; Sadowski, M.; Ghidui, M.; Minafra, N.; Senyshyn, A.; Albe, K.; Zeier, W. G. *Adv. Energy Mater.* **2020**, *11*, 2003369.
- (25) Morgan, B. *J. Chem. Mater.* **2021**, *33*, 2004–2018.
- (26) Sadowski, M.; Albe, K. *Philos. Trans. R. Soc. A* **2021**, *379*, 20190458.
- (27) Lu, Z.; Chen, C.; Baiyee, Z. M.; Chen, X.; Niu, C.; Ciucci, F. *Phys. Chem. Chem. Phys.* **2015**, *17*, 32547–32555.
- (28) Zhang, Z.; Ramos, E.; Lalère, F.; Assoud, A.; Kaup, K.; Hartman, P.; Nazar, L. F. *Energy Environ. Sci.* **2018**, *11*, 87–93.
- (29) Yu, Z.; Shang, S.-L.; Seo, J.-H.; Wang, D.; Luo, X.; Huang, Q.; Chen, S.; Lu, J.; Li, X.; Liu, Z.-K.; Wang, D. *Adv. Mater.* **2017**, *29*, 1605561.
- (30) Kwak, H.; Park, K. H.; Han, D.; Nam, K.-W.; Kim, H.; Jung, Y. S. *J. Power Sources* **2020**, *446*, 227338.
- (31) Li, X.; Liang, J.; Yang, X.; Adair, K. R.; Wang, C.; Zhao, F.; Sun, X. *Energy Environ. Sci.* **2020**, *13*, 1429–1461.
- (32) Krauskopf, T.; Culver, S. P.; Zeier, W. G. *Chem. Mater.* **2018**, *30*, 1791–1798.
- (33) Culver, S. P.; Squires, A. G.; Minafra, N.; Armstrong, C. W. F.; Krauskopf, T.; Böcher, F.; Li, C.; Morgan, B. J.; Zeier, W. G. *J. Am. Chem. Soc.* **2020**, *142*, 21210–21219.
- (34) Ashcroft, N., *Solid State Physics*; Cengage Learning: Andover England, 1976.
- (35) Zulueta, Y. A.; Nguyen, M. T.; Dawson, J. A. *Inorg. Chem.* **2020**, *59*, 11841–11846.
- (36) Kuganathan, N.; Rushton, M. J. D.; Grimes, R. W.; Kilner, J. A.; Gkanas, E. I.; Chroneos, A. *Sci. Rep.* **2021**, *11*.
- (37) Maier, J. *Angew. Chem. Int. Ed Engl.* **1993**, *32*, 313–335.
- (38) Zhang, S. B.; Northrup, J. E. *Phys. Rev. Lett.* **1991**, *67*, 2339–2342.
- (39) Buckeridge, J. *Comp. Phys. Commun.* **2019**, *244*, 329–342.
- (40) Han, F.; Westover, A. S.; Yue, J.; Fan, X.; Wang, F.; Chi, M.; Leonard, D. N.; Dudney, N. J.; Wang, H.; Wang, C. *Nat. Energy* **2019**, *4*, 187–196.

- (41) De Jonghe, L. C.; Feldman, L.; Beuchele, A. *J. Mater. Sci.* **1981**, *16*, 780–786.
- (42) Aguesse, F.; Manalastas, W.; Buannic, L.; Lopez del Amo, J. M.; Singh, G.; Lordés, A.; Kilner, J. *ACS Appl. Mater. & Inter.* **2017**, *9*, 3808–3816.
- (43) Gorai, P.; Famprakis, T.; Singh, B.; Stevanović, V.; Canepa, P. *Chem. Mater.* **2021**, *33*, 7484–7498.
- (44) Buckeridge, J. *Comput. Phys. Commun.* **2019**, *244*, 329–342.
- (45) Wolfenstine, J.; Allen, J. L.; Read, J.; Sakamoto, J. *J. Mater. Sci.* **2013**, *48*, 5846–5851.
- (46) Squires, A. G.; Scanlon, D. O.; Morgan, B. J. *Chem. Mater.* **2020**, *32*, 1876–1886.
- (47) Krauskopf, T.; Richter, F. H.; Zeier, W. G.; Janek, J. *Chem. Rev.* **2020**, *120*, 7745–7794.
- (48) Lany, S. *Phys. Status Solidi B* **2011**, *248*, 1052–1060.
- (49) Lany, S.; Zunger, A. *Phys. Rev. B* **2009**, *80*, 085202.
- (50) Ohno, S.; Banik, A.; Dewald, G. F.; Kraft, M. A.; Krauskopf, T.; Minafra, N.; Till, P.; Weiss, M.; Zeier, W. G. *Prog. Energy* **2020**, *2*, 022001–36.
- (51) Kubicek, M.; Wachter-Welzl, A.; Rettenwander, D.; Wagner, R.; Berendts, S.; Uecker, R.; Amthauer, G.; Hutter, H.; Fleig, J. *Chem. Mater.* **2017**, *29*, 7189–7196.

Practicable solutions to Schrödinger's wave equation for solid-state systems

The principle goal of the quantum mechanical calculations presented in this work is to facilitate the solution of the equations described in Chapter 2. Due to the work of many quantum physicists in the early twentieth century, these variable terms in these equations are calculable via the Schrödinger equation,

$$\widehat{H}\Psi(\{\mathbf{R}_I, \mathbf{r}_i\}) = E\Psi(\{\mathbf{R}_I, \mathbf{r}_i\}). \quad (3.1)$$

In the above, \widehat{H} is the Hamiltonian operator, E is the total energy, and $\Psi(\{\mathbf{R}_I, \mathbf{r}_i\})$ is the wave function [1]. The wave function describes a system of nuclei with positions $\{\mathbf{R}_I\}$ and electrons described by $\{\mathbf{r}_i\}$. Once the wave function is known, many useful physical properties of that system can be calculated. The significance of this work was perhaps best summarised by Paul Dirac when he declared,

“The underlying physical laws necessary for the mathematical theory of a large part of physics and the whole of chemistry are thus completely known ...” [2]

However, solving the Schrödinger equation for realistic materials is not trivial: the *many-body* Hamiltonian is comprised of terms that are simultaneously dependent on the interactions between all particles in the system:

$$\widehat{H} = - \overbrace{\sum_I \frac{\hbar^2}{2M_N} \nabla_I^2}^{\widehat{T}_{\text{nuc}}} - \overbrace{\sum_i \frac{\hbar^2}{2m_e} \nabla_i^2}^{\widehat{T}_{\text{elec}}} + \overbrace{\frac{1}{2} \sum_{i \neq j} \frac{e^2}{|\mathbf{r}_i - \mathbf{r}_j|}}^{V_{\text{elec-elec}}} - \overbrace{\sum_i \sum_I \frac{eZ_I}{|\mathbf{r}_i - \mathbf{R}_I|}}^{V_{\text{nuc-elec}}} + \overbrace{\frac{1}{2} \sum_{I \neq J} \frac{Z_I Z_J}{|\mathbf{R}_I - \mathbf{R}_J|}}^{V_{\text{nuc-nuc}}} \quad (3.2)$$

where \hbar is the reduced Planck's constant,¹ i is the electronic index, I is the nuclear index, ∇^2 is the Laplacian operator, e is the electron charge, m_e is the rest mass of an electron, Z is the nuclear charge and M_N is the mass of the nucleus. As more electrons and nuclei are added to our system, we

$${}^1 \hbar = \frac{h}{2\pi}$$

increase the number of coupled, non-linear equations that must be solved to reach a solution, vastly increasing calculation complexity and rendering analytical solutions impossible. Dirac's quote concludes

“... and the difficulty is only that the exact application of these laws leads to equations much too complicated to be soluble.”

Computationally tractable solutions must therefore make approximations.

The first approximation invoked is the *Born-Oppenheimer* approximation originating from the mass difference between a nucleon and an electron ($M_N \approx 2000 m_e$). Because of this large difference we consider nuclear motion to be negligible on the timescale of electronic motion [3]; $\Psi(\{\mathbf{R}_I, \mathbf{r}_i\})$ becomes $\Psi(\{\mathbf{r}_i\})$. \hat{T}_{nuc} is now zero and nuclear positions define the fixed external potential, $V_{\text{nuc-elec}}$. The Born-Oppenheimer Hamiltonian can be written as

$$\hat{H} = \hat{T}_{\text{elec}} + V_{\text{elec-elec}} + V_{\text{nuc-elec}}. \quad (3.3)$$

To further reduce the parameter space associated with an exact solution to the Schrödinger equation, early quantum chemical approaches were based on the assumption that the many-body wave function, $\Psi(\{\mathbf{r}_i\})$ can be approximated as the product of a set of non-interacting, one-electron wave functions, $\{\chi(\mathbf{r}_i)\}$

$$\Psi(\{\mathbf{r}_i\}) \approx \chi_1(\mathbf{r}_1)\chi_2(\mathbf{r}_2) \dots \chi_n(\mathbf{r}_n). \quad (3.4)$$

See Figure 3.1 for an illustration of this approach. This approximation is named for its progenitor, Douglas Hartree [4]. Each of these one-electron wave functions will be defined by a one-electron Hamiltonian, \hat{h} , such that

$$\hat{h}_i \chi_i(\mathbf{r}_i) = \varepsilon_i \chi_i(\mathbf{r}_i), \quad (3.5)$$

and \hat{h} has the form

$$\hat{h}_i = -\frac{\hbar^2}{2m_e} \sum_i \nabla_i^2 + \sum_I \frac{v_{\text{nuc-elec}}}{|\mathbf{r}_i - \mathbf{R}_I|}. \quad (3.6)$$

This has removed the $V_{\text{elec-elec}}$ term from our Born-Oppenheimer Hamiltonian (Equation (3.3)); the total energy of this non-interacting system is the sum of the one-electron energies.

Rather than ignoring electron-electron interactions entirely, we can instead treat our independent electrons moving in a Coulombic potential created by the presence of all the other electrons in the system. We can obtain an average interaction by using the electron density $\rho(\mathbf{r})$, given

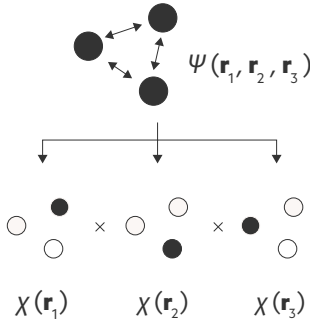


Figure 3.1: The Hartree approximation assumes that the $3n$ -dimensional wave function, $\Psi(\mathbf{r}_1, \mathbf{r}_2, \mathbf{r}_3)$ can be satisfactorily approximated by the product of n 3-dimensional single-particle wave functions, $\chi(\mathbf{r}_1)\chi(\mathbf{r}_2)\chi(\mathbf{r}_3)$.

by the square of the wave function. We label the energy contribution from this interaction the Hartree energy. In an illustrative helium-like (two-electron) system, the Hamiltonian in our eigenequation for electron one thus includes the terms in our previous Hamiltonian above, with an additional term to account for the interaction of electron one with this mean-field, v_{Hartree} ,

$$\widehat{H}_1 = \widehat{t}_{\text{elec}} + v_{\text{nuc-elec}} - \int \frac{\rho(\mathbf{r}_2)}{|\mathbf{r}_1 - \mathbf{r}_2|} d\mathbf{r} \quad (3.7)$$

$$\rho(\mathbf{r}_2) = |\chi_2|^2. \quad (3.8)$$

See Figure 3.2 for an illustration of this approach.

It is clear that solving the Schrödinger equation in this formalism is still non-trivial: to evaluate the Hamiltonian and determine the wave function of either electron we must know the potential produced by the other electron, which is dependent on its wave function. Solutions are obtained iteratively using the following procedure:

- Calculate the electron density, $\{\chi_i\}^2$, of our system given a set of trial one-electron wave functions, $\{\chi_i\}$.
- Solve Equation (3.7) given $\{\chi_i\}^2$.
- Solve Equation (3.6) for each one-electron Hamiltonian, producing $\{\varepsilon_i\}$ and a new trial wave function, $\{\chi_i'\}$.
- Repeat until $\{\chi_i\}$ and $\{\chi_i'\}$ match within some specified tolerance.

Solving the Schrödinger equation in such a manner relies on the variational principle: the ground state energy of the system is always lower than or equal to the energy produced by a trial Hamiltonian. This means that when we reach a self-consistent minimum (i.e when $\{\chi_i\} = \{\chi_i'\}$), we have reached the ground state.

To provide valid solutions to the Schrödinger equation, the system wave function must obey the Pauli exclusion principle, i.e. $\Psi(\{\mathbf{r}_i\})$ must change sign if any two electrons are exchanged [5]. The Hartree product (Equation (3.4)) does not obey the Pauli exclusion principle; work by John Slater and Vladimir Fock identified what would come to be known as a Slater determinant ensures conformity with the Pauli exclusion principle by construction [6, 7]. Slater determinants have the form

$$\Psi(\{\mathbf{r}_i\}) = \frac{1}{\sqrt{n!}} \begin{vmatrix} \chi_1(\mathbf{r}_1) & \chi_2(\mathbf{r}_1) & \dots & \chi_n(\mathbf{r}_1) \\ \chi_1(\mathbf{r}_2) & \chi_2(\mathbf{r}_2) & \dots & \chi_n(\mathbf{r}_2) \\ \vdots & \vdots & \ddots & \vdots \\ \chi_1(\mathbf{r}_n) & \chi_2(\mathbf{r}_n) & \dots & \chi_n(\mathbf{r}_n) \end{vmatrix} \quad (3.9)$$

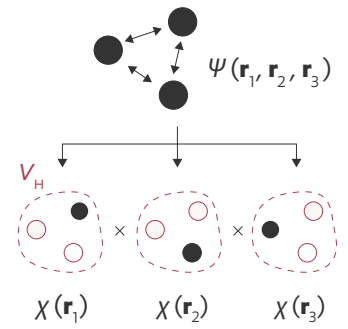


Figure 3.2: With reference to Figure 3.1, our independent electron treatment can be improved by a solution where each electron is influenced by the potential arising from its interaction with the mean-field created by all other electrons, V_H .

where $1/\sqrt{n!}$ is the normalisation factor for an n electron system. A given single-particle wave function can only be included once in a Slater determinant, otherwise, the determinant would become zero over all space. In other words, a Slater determinant requires that all orbitals are occupied by no more than two electrons of opposite spins.

Minimising the energy of a Slater determinant—observing that the orbitals must be normalised, and orthogonal²—with respect to the single particle wave functions yields the Hartree-Fock equations [7]:

$$[\hat{t}_{\text{elec}} + v_{\text{nuc-elec}} - v_{\text{Hartree}}] \chi_i(\mathbf{r}) - v_{\text{Ex}}(\mathbf{r}_i) \chi_j(\mathbf{r}_i) = \varepsilon_i \chi_i(\mathbf{r}) \quad (3.10)$$

$$v_{\text{Ex}}(\mathbf{r}_i) = e^2 \sum_{j \neq i} \int \frac{\chi_j^*(\mathbf{r}') \chi_i(\mathbf{r}')}{|\mathbf{r} - \mathbf{r}'|} d\mathbf{r}'. \quad (3.11)$$

$v_{\text{Ex}}(\mathbf{r}_i)$ is the *exchange* potential. Exchange interactions have no classical analogue, but for our purposes it can be considered as a stabilising contribution to the total energy on accounting for Pauli repulsion [8].

This mean-field approach has a key limitation. Electrons do not move independently of the other electrons in the system, there is *correlation* between the position of electrons due to their mutual Coulomb repulsion. Accounting for correlation further alters the energy from the purely classical interaction between electrons and the mean-field of the system and is not accounted for in pure Hartree-Fock approaches.

3.1 Density functional theory

Owing to the complexity of the many-body wave function, Hartree-Fock theory approximates a fully interacting system with a fictitious one in which there is no correlation between the spatial positions of electrons. Density Functional Theory (DFT) circumvents the need for such an approximation by presenting a method to calculate the exact system energy in terms of a 3-dimensional electron density as opposed to a $3n$ -dimensional wave function.

In the 1960s, Pierre Hohenberg and Walter Kohn established the relationship between electron density ($\rho(\mathbf{r})$) and total energy forming the theoretical basis for DFT by proving two key theorems [9],

- 1 An external potential, V_{ext} ($V_{\text{nuc-elec}}$ in Equation (3.3)), and hence the total energy, is a unique functional of the ground state electron density.

In other words, the electron density is uniquely defined by the interactions between electrons and nuclei: the external potential V_{ext} . Internal energy ($\hat{T}_{\text{elec}} + V_{\text{elec-elec}}$) is independent of this interaction, and therefore, the relationship between internal energy and electron density is defined by a

² These conditions are often combined into the term *orthonormality*.

universal functional $F[\rho(\mathbf{r})]$

$$E[\rho(\mathbf{r})] \equiv \int \rho(\mathbf{r})V_{\text{ext}}(\mathbf{r})d\mathbf{r} + F[\rho(\mathbf{r})]. \quad (3.12)$$

The second theorem states

- 2 The variational principle is valid for this energy functional, $E[\rho(\mathbf{r})]$, such that for the correct ground-state electron density, the energy functional is minimal and as such, equal to the total, exact ground state energy of the system.

This means that (unlike Hartree-Fock theory) DFT can be used to solve for total energy using a self-consistent field approach with respect to the electron density (as opposed to the wave function). Hohenberg and Kohn had proved that the exact energy could be solved using the electron density as opposed to the wave function, but they did not provide a means to do so.

A practical approach followed the next year developed by Kohn and Lu Jeu Sham. The Kohn-Sham approach proposes that the interacting many-body electron density, $\rho(\mathbf{r})$, which can be written as

$$\rho(\mathbf{r}) = \sum_i |\psi_i(\mathbf{r}_i)|^2, \quad (3.13)$$

can be represented by an auxiliary system of non-interacting “Kohn-Sham” single-electron orbitals, ϕ_i , with the same ground-state density as that of the interacting system [10]

$$\rho(\mathbf{r}) = \sum |\phi(\mathbf{r}_i)|^2. \quad (3.14)$$

Kohn-Sham orbitals need not resemble conventional electronic orbitals, they can be any set of functions that recover the many-body electron density.

Partitioning energy as a functional of density gives

$$E[\rho(\mathbf{r})] = T[\rho(\mathbf{r})] + E_{\text{ext}}[\rho(\mathbf{r})] + E_{\text{H}}[\rho(\mathbf{r})] + E_{\text{Ex}}[\rho(\mathbf{r})] + E_{\text{C}}[\rho(\mathbf{r})] \quad (3.15)$$

where $T[\rho(\mathbf{r})]$ is the electron kinetic energy, $E_{\text{ext}}[\rho(\mathbf{r})]$ is the external energy, $E_{\text{H}}[\rho(\mathbf{r})]$ is the Hartree energy, i.e. the energy contribution from the classical electrostatic interactions between electrons, and $E_{\text{Ex}}[\rho(\mathbf{r})]$ and $E_{\text{C}}[\rho(\mathbf{r})]$ are the exchange and correlation energies respectively. The form of the interacting density kinetic energy functional, $T[\rho(\mathbf{r})]$ is not known, however, the kinetic energy for the *non-interacting* Kohn-Sham single particle system ($T_{\text{KS}}[\rho(\mathbf{r})]$) can be calculated exactly as in the Hartree-Fock method, likewise for the Hartree energy. All remaining energy contribu-

tions arising from the non-classical interactions between electrons are collected in a single term $E_{\text{Ex-C}}[\rho(\mathbf{r})]$ (the *exchange-correlation* energy). In other words, the $E_{\text{Ex-C}}[\rho(\mathbf{r})]$ term contains the energy contributions from errors associated with the non-interacting Kohn-Sham model,

$$E_{\text{Ex-C}}[\rho(\mathbf{r})] = (\widehat{T}[\rho(\mathbf{r})] - \widehat{T}_{\text{KS}}[\rho(\mathbf{r})]) + (E_{\text{elec-elec}}[\rho(\mathbf{r})] - E_{\text{H}}[\rho(\mathbf{r})]) \quad (3.16)$$

Slater determinants are again used to describe the total wave function. The one-electron Kohn-Sham equations can be written similarly to the Hartree-Fock equations as

$$\overbrace{[\widehat{T}_{\text{KS}} + V_{\text{H}} + V_{\text{ext}} + V_{\text{Ex-C}}]}^{\widehat{H}_{\text{KS}}} \phi_i(\mathbf{r}) = \epsilon_i \phi_i(\mathbf{r}). \quad (3.17)$$

Unlike Hartree-Fock theory, *in principle* the effects of electron exchange and correlation are fully accounted for in DFT. In practice, however, the form of $V_{\text{Ex-C}}$ is unknown, and approximations must be made.

3.2 Approximating exchange & correlation energies

Selecting an appropriate exchange-correlation functional is one of the most important considerations at the beginning of any DFT study. Remarkably, relatively simple approximations to $E_{\text{Ex-C}}$ can produce sufficiently accurate results in many cases. The simplest of these approximations is the local density approximation (LDA). Under this regime, it is assumed that the exchange-correlation energy contribution is equal to that of a homogeneous electron gas (HEG) with the same local density as the system of interest [10]

$$E_{\text{Ex-C}}^{\text{LDA}} = \int E_{\text{Ex-C}}^{\text{HEG}}[\rho(\mathbf{r})] \mathbf{d}\mathbf{r}. \quad (3.18)$$

For a HEG, exchange can be calculated exactly [11, 12],

$$E_{\text{X}}^{\text{HEG}}[\rho(\mathbf{r})] = \frac{3}{4} \left(\frac{6}{\pi} \right)^{\frac{1}{3}} \rho^{\frac{4}{3}}(\mathbf{r}). \quad (3.19)$$

The equivalent calculation for correlation cannot be performed analytically. It is instead calculated by fitting to high-precision quantum Monte Carlo simulations of uniform electron gases [13]. Despite the inherently non-local nature of exchange and correlation, systems with well-distributed electron density, such as metals, are well modelled with LDA approaches.

For systems with electron density that varies more strongly over space, a range of “gradient-corrected” exchange-correlation functionals have been

developed to introduce a degree of non-locality into Kohn-Sham DFT. These functionals not only include a dependence on the local density, but also the first derivative of the density, giving rise to the name generalised gradient approximation (GGA) functionals, termed a “semi-local” functional. GGA functionals can be represented generally as

$$E_{\text{Ex-C}}^{\text{GGA}} = \int E_{\text{Ex-C}}^{\text{HEG}}[\rho(\mathbf{r})] F_{\text{Ex-C}}^{\text{HEG}}[\rho(\mathbf{r}), \Delta\rho(\mathbf{r})] d\mathbf{r} \quad (3.20)$$

where $F_{\text{Ex-C}}^{\text{HEG}}[\rho(\mathbf{r}), \Delta\rho(\mathbf{r})]$ is the gradient correction term. There are many different ways this term can be parameterised leading to a wide variety of GGA functionals that can be broadly categorised into those which are derived by fitting to experimental parameters, and those which are derived from physical constraints, such as the highly popular PBE [14] and PBEsol functionals [15]. GGA functionals perform well over a range of solids, reproducing properties such as lattice parameters with small errors [16]. This level of theory has a great appeal on modern computing architectures with a respectable accuracy–cost trade-off, enabling studies involving vast quantities of DFT calculations containing useful information with comparatively little computational and researcher effort [17–19].

3.3 Solving the Schrödinger equation for an infinite crystal: periodicity, Bloch theorem & plane waves

On an experimental length scale, a crystal will contain a vast number of electrons—easily on the order of Avagadro’s constant. Even within the approximate model of Kohn-Sham DFT, such a system cannot be modelled directly. To approximate behaviour on longer length scales, we can exploit the periodicity of crystalline materials and instead model an infinite system. Because our material is crystalline, a single unit cell should contain all the information necessary to represent the infinite material: the properties of all other unit cells are related by symmetry. This approximation holds as long as the system of interest has negligible size effects.³

The geometric arrangement of atoms in a macroscopic crystal is described by the positions of the atoms in the unit cell, the crystallographic basis, and the lattice vectors \mathbf{a} , \mathbf{b} and \mathbf{c} . The lattice vectors describe all possible periodic images of the unit cell

$$\mathbf{R} = n_1\mathbf{a} + n_2\mathbf{b} + n_3\mathbf{c} \quad (3.21)$$

where n_1 , n_2 and n_3 are integers. The lattice is unchanged when translated by the lattice vectors; if the positions of the crystallographic bases within

³ Astute readers will notice that the presence of point defects introduces size effects as it breaks the periodic symmetry assumed for a perfect crystal; dealing with point defects within periodic DFT is discussed in section 4.1.

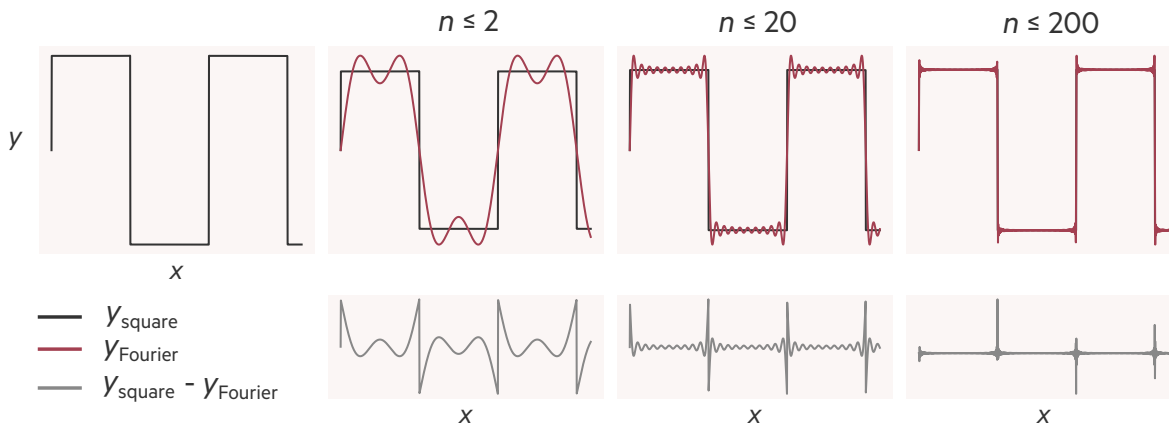


Figure 3.3: Modelling a periodic function with a Fourier series: the **left-most** panel shows a “square” function we are trying to model; the **second panel** from the left shows that function overlaid by a Fourier series of the form

$$\sum_n \frac{\sin(2n - 1x)}{2n - 1}$$

where $n \leq 2$; the **third panel** shows the same scenario for $n \leq 20$; the **right-most panel** shows the same again, but for $n \leq 200$. For each of the Fourier series, a difference plot (w.r.t to the function to be modelled) is included beneath.

the unit cell are \mathbf{r} , then

$$\mathbf{r} + \mathbf{R} = \mathbf{r}. \quad (3.22)$$

Likewise, any function $f(\mathbf{r})$ that shares the periodicity of the lattice translated by \mathbf{R} will not change:

$$f(\mathbf{r} + \mathbf{R}) = f(\mathbf{r}) \quad (3.23)$$

this includes, for example, the external potential exerted on the electrons by the nuclei.

In an infinite, periodic solid, electronic (Kohn-Sham) wave functions are no longer described by chemical orbitals, but are instead Bloch functions, $\psi_{\mathbf{k}}$ [20]:

$$\psi_{\mathbf{k}} = u(\mathbf{r})_{\mathbf{k}} \exp(\mathbf{i}\mathbf{k}\mathbf{r}). \quad (3.24)$$

The Bloch function is a product of the basis function $u(\mathbf{r})_{\mathbf{k}}$ which shares the periodicity of the crystal lattice, and $\exp(\mathbf{i}\mathbf{k}\mathbf{r})$, a plane wave.⁴ \mathbf{k} is the wave vector; the set of all values of \mathbf{k} form a space known as reciprocal-space. Like a real-space crystal lattice, the corresponding reciprocal space lattice is periodic, and as such, there is a discrete unit of reciprocal space that contains all values of \mathbf{k} that will return a unique solution to Equation (3.24). This is known as the *Brillouin zone*, and is the reciprocal space equivalent of the primitive cell. Further discussion of the physical significance of \mathbf{k} and the Brillouin zone can be found in Section 4.2.4.

Within periodic DFT, we solve for the set of periodic functions that minimises the total energy in a normalised sum over all values of \mathbf{k} . To ensure calculations remain accurate without excess computational cost, we exploit the fact that the wave function varies smoothly within reciprocal space: sampling an equally spaced grid of points (the Monkhorst-Pack

⁴ $\mathbf{i} = \sqrt{-1}$

method [21]), the \mathbf{k} -point mesh density is systematically increased until convergence criteria are met.

The periodic function $u(\mathbf{r})_{\mathbf{k}}$ can be constructed from a Fourier series (a superposition of harmonically related sine and cosine waves, plane waves). $u(\mathbf{r})_{\mathbf{k}}$ can be written as

$$u(\mathbf{r})_{\mathbf{k}} = \sum_{\mathbf{G}} c_{\mathbf{k},\mathbf{G}} \exp(i\mathbf{G}\mathbf{r}) \quad (3.25)$$

where $c_{\mathbf{k},\mathbf{G}}$ are the Fourier expansion coefficients, and $\exp(i\mathbf{G}\mathbf{r})$ is a plane wave with wave vectors \mathbf{G} that are reciprocal lattice vectors of the crystal. As more terms are added to the Fourier series, the “Bloch wave” and therefore the electron density are described with increasing accuracy (see Figure 3.3). The point at which the expansion is truncated is typically determined via convergence testing: some property of interest is calculated with respect to a plane wave cutoff kinetic energy, which is proportional to $|\mathbf{k} + \mathbf{G}|^2$,

$$\frac{1}{2}|\mathbf{k} + \mathbf{G}|^2 < E_{\text{cut}}. \quad (3.26)$$

E_{cut} is set at the value which further increases in the basis set size no longer return a meaningful change in a target property (typically total energy). Combining Equations (3.24) and (3.25), gives us an expression for the wave function of a periodic system

$$\psi_{\mathbf{k}} = u(\mathbf{r})_{\mathbf{k}} \exp(i\mathbf{k}\mathbf{r}), \quad (3.27)$$

$$= \sum_{\mathbf{G}} c_{\mathbf{k},\mathbf{G}} \exp(i\mathbf{G}\mathbf{r}) \exp(i\mathbf{k}\mathbf{r}) \quad (3.28)$$

$$= \sum_{\mathbf{G}} c_{\mathbf{k},\mathbf{G}} \exp[(i\mathbf{G} + \mathbf{k})\mathbf{r}]. \quad (3.29)$$

3.4 The core electrons

Sudden changes in electron density are hard to capture using a plane-wave basis set. This is illustrated in Figure 3.3 where it is clear that even when our Fourier series contains 200 plane waves, the areas surrounding the steep gradients in the function to be modelled are comparatively poorly described. This is problematic in chemical systems when describing the region around the nucleus where there are strong oscillations in the electronic wave functions (and therefore, the electron density).⁵ Modelling these core states directly is not only resource-intensive but also fairly uninformative for our purposes as the chemical properties of the elements are typically determined by their valence electrons. Therefore, rather than model these states directly, a *pseudopotential* can be used. The pseudopotential represents a “frozen-core” approximation for the nucleus and core

⁵ Orthonormal wave functions have a high number of nodes near the nucleus

electrons; the core acts as a combined potential that influences the valence electrons, generating a pseudo-wave-function $\tilde{\psi}$ that is smooth and nodeless [22] but accurately captures the wave function of the valence electrons. The pseudopotentials are constructed from all-electron calculations of independent atoms in such a way that they are transferable between other calculations, i.e. once a pseudopotential is parametersised for a given element with a given exchange-correlation functional, in principle, this calculation need not be repeated.

Within a true pseudopotential approach, information about the core electrons is lost, however, all-electron calculations are resource-intensive. A compromise between the two is found in the projector augmented wave (PAW) method, in which the pseudopotential is constructed in such a way that some transformation operator, τ , can recover the all electron (Kohn-Sham) wave function [23]

$$\phi(\mathbf{r}) = \tau\tilde{\phi}(\mathbf{r}). \quad (3.30)$$

The PAW method is adopted for all DFT calculations in this work.

3.5 Failings of DFT in the description of defective systems

Given an atom with n electrons, during ionisation or electron addition (common during the formation of charged defects), the intermediate state can be described as a statistical mixture of the n electron atom and the $n \pm 1$ electron atom,

$$E(n) = (1 - \omega)E_n + \omega E_{n+1} \quad (3.31)$$

where ω has a value of $0 \leq \omega \leq 1$ and represents the statistical weight of the E_{n+1} state. $E(n)$ is therefore linear between integer occupation numbers and discontinuous at integer values. LDA and GGA calculations do not capture this $E(n)$ dependence correctly owing to the *self-interaction* error present in local and semi-local Kohn-Sham-DFT. Within the Hartree potential, the classical electrostatic interaction between each Kohn-Sham electron $\phi(\mathbf{r}_i)$ and all other electrons $\{\phi(\mathbf{r}_{j \neq i})\}$ is dependent on the full electron density, $\{\phi(\mathbf{r}_i)\}^2$, including the density contribution of the electron $\phi(\mathbf{r}_i)$, hence the term self-interaction error. This behavior will artificially stabilise partially-occupied (delocalised) solutions to electron addition/removal in defect calculations as opposed to lower energy integer occupation solutions [24]. The $E_{\text{exact}}(n)$ and $E_{\text{DFT}}(n)$ relationships are compared in Figure 3.4.

The continuous nature of the $E_{\text{DFT}}(n)$ relationship foreshadows an additional issue inherent in local and semi-local DFT approaches. The

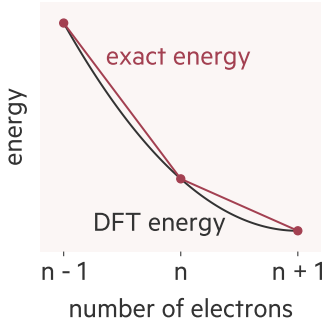


Figure 3.4: Plot showing the relationship between the DFT energy as a function of the number of electrons as compared to the exact $E(n)$ relationship.

band gap, E_g of a material can be written as,⁶

$$E_g^{\text{integer}} = [E(n-1) - E(n)] - [E(n) + E(n-1)]. \quad (3.33)$$

For the exact Ex-C functional, E_g^{integer} is equal to

$$E_g^{\text{derivative}} = \left[\frac{\partial E}{\partial n} \Big|_{n+\delta} - \frac{\partial E}{\partial n} \Big|_{n-\delta} \right]. \quad (3.34)$$

For local and semi-local DFT, $E_g^{\text{integer}} \neq E_g^{\text{derivative}}$, owing to the continuous nature of $E_{\text{DFT}}(n)$, which has its origins in the self-interaction error, and the fictitious nature of the Kohn-Sham orbitals [25]. The result is LDA and GGA are consistent in underestimating the band gaps of semiconductors. Corrections to the local and semi-local DFT approaches recovering the linear response of the $E(n)$ can improve both the relative stability of localised and delocalised solutions and the description of the band gap [26].

3.5.1 Hybrid-DFT

Where GGA artificially stabilises delocalised wave functions, Hartree-Fock theory over-stabilises localised solutions [24, 25]. Therefore, combining a fraction of exact Hartree-Fock exchange with the DFT Ex-C energy can theoretically restore the expected linear response to electron addition/ionisation [27]. This hybrid DFT-Hartree-Fock approach (hybrid-DFT) can improve both the description of the band gap and the relative stabilities of localised and delocalised solutions [28]. Hybrid-DFT functionals are generally described by

$$E_{\text{Ex-C}}^{\text{hybrid}} = \alpha E_{\text{Ex}}^{\text{HF}} + (1 - \alpha) E_{\text{Ex-C}}^{\text{DFT}} \quad (3.35)$$

where the α parameter is the fraction of exact exchange mixing. To reduce the expense associated with the calculation of exact exchange, a range approximation is often employed such that we assume the exchange energy at long distances can be satisfactorily described by a GGA functional, and consider exact exchange at only short ranges. Such screened hybrid functionals take the form

$$E_{\text{Ex-C}}^{\text{s-hybrid}}(\alpha, \omega) = \alpha E_{\text{Ex}}^{\text{HF}}(\omega) + (1 - \alpha) E_{\text{Ex}}^{\text{DFT,SR}}(\omega) + E_{\text{Ex}}^{\text{DFT,LR}}(\omega) + E_{\text{C}}^{\text{DFT}} \quad (3.36)$$

Where ω is a range-screening factor. Accordingly, these functionals tend to a full hybrid description as $\omega \rightarrow \infty$ and GGA as $\omega \rightarrow 0$; a very popular implementation for modelling defect chemistry in crystal systems is the

⁶ Equivalently, the band gap can be defined as

$$E_g = E_{\text{I}} - E_{\text{A}}. \quad (3.32)$$

where E_{I} and E_{A} are the ionisation and electron affinity energies respectively.

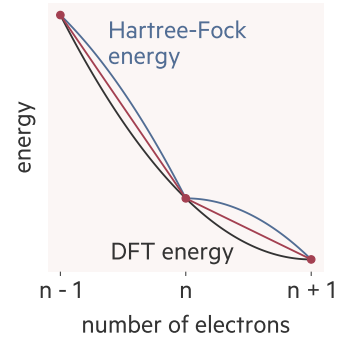


Figure 3.5: Plot showing the relationship between the Hartree-Fock (HF) energy as a function of the number of electrons as compared to the exact $E(n)$ relationship and the DFT reported energy.

Heyd–Scuseria–Ernzerhof functional (HSE06) [29, 30]. In HSE06 ω is 0.11 a_0^{-1} and α is 0.25 and the the PBE functional is used to calculated the GGA Ex-C contributions. While ultimately a form of error cancellation, hybrid functionals have been shown to provide significant improvements over purely local-based approaches. In particular, HSE06 can accurately reproduce the experimental band gaps of many semiconductors [31, 32], while also providing reasonable descriptions of localised charge carriers [33]. The disadvantage is that hybrid-DFT calculations demand significantly more computational resources, meaning their indiscriminate use is often prohibited.

Bibliography

- (1) Schrödinger, E. *Ann. Phys. (Berl.)* **1926**, 384, 361–376.
- (2) Dirac, P. *Proc. R. Soc. A* **1929**, 123, 714–733.
- (3) Born, M.; Oppenheimer, R. *Ann. Phys. (Berl.)* **1927**, 389, 457–484.
- (4) Hartree, D. R. *Math. Proc. Camb. Philos. Soc.* **1928**, 24, 111–132.
- (5) Pauli, W. *Z. Phys.* **1925**, 31, 765–783.
- (6) Slater, J. C. *Phys. Rev.* **1928**, 32, 339–348.
- (7) Fock, V. *Z. Phys.* **1930**, 61, 126–148.
- (8) Rackers, J. A.; Ponder, J. W. *J. Chem. Phys.* **2019**, 150, 084104.
- (9) Hohenberg, P.; Kohn, W. *Phys. Rev.* **1964**, 136, B864–B871.
- (10) Kohn, W.; Sham, L. J. *Phys. Rev.* **1965**, 140, A1133–A1138.
- (11) Dirac, P. A. M. *Math. Proc. Camb. Philos. Soc.* **1930**, 26, 376–385.
- (12) Beattie, A. M.; Stoddart, J. C.; March, N. H. *Proc. R. Soc. A* **1971**, 326, 97–116.
- (13) Ceperley, D. M.; Alder, B. J. *Phys. Rev. Lett.* **1980**, 45, 566–569.
- (14) Perdew, J. P.; Burke, K.; Ernzerhof, M. *Phys. Rev. Lett.* **1996**, 77, 3865–3868.
- (15) Perdew, J.; Ruzsinszky, A.; Csonka, G.; Vydrov, O.; Scuseria, G.; Constantin, L.; Zhou, X.; Burke, K. *Phys. Rev. Lett.* **2008**, 100, 136406.
- (16) Lejaeghere, K. et al. *Science* **2016**, 351, aad3000–aad3000.
- (17) Jain, A.; Ong, S. P.; Hautier, G.; Chen, W.; Richards, W. D.; Dacek, S.; Cholia, S.; Gunter, D.; Skinner, D.; Ceder, G.; Persson, K. a. *APL Mater.* **2013**, 1, 011002.
- (18) Kirklin, S.; Saal, J. E.; Meredig, B.; Thompson, A.; Doak, J. W.; Aykol, M.; Rühl, S.; Wolverton, C. *npj Comput. Mater.* **2015**, 1, 1–15.

- (19) Curtarolo, S.; Setyawan, W.; Wang, S.; Xue, J.; Yang, K.; Taylor, R. H.; Nelson, L. J.; Hart, G. L.; Sanvito, S.; Buongiorno-Nardelli, M.; Mingo, N.; Levy, O. *Comput. Mater. Sci.* **2012**, *58*, 227–235.
- (20) Bloch, F. *Z. Phys.* **1929**, *52*, 555–600.
- (21) Monkhorst, H. J.; Pack, J. D. *Phys. Rev. B* **1976**, *13*, 5188–5192.
- (22) Kaxiras, E., *Atomic and Electronic Structure of Solids*; Cambridge University Press: 2003.
- (23) Blöchl, P. E. *Phys. Rev. B* **1994**, *50*, 17953–17979.
- (24) Lany, S.; Zunger, A. *Phys. Rev. B* **2009**, *80*, 085202.
- (25) Mori-Sánchez, P.; Cohen, A. J.; Yang, W. *Phys. Rev. Lett.* **2008**, *100*.
- (26) Perdew, J. P.; Levy, M. *Phys. Rev. Lett.* **1983**, *51*, 1884–1887.
- (27) Wing, D.; Strand, J.; Durrant, T.; Shluger, A. L.; Kronik, L. *Phys. Rev. Mater.* **2020**, *4*.
- (28) Becke, A. D. *J. Chem. Phys.* **1993**, *98*, 1372–1377.
- (29) Heyd, J.; Scuseria, G. E.; Ernzerhof, M. *J. Chem. Phys.* **2003**, *118*, 8207–8215.
- (30) Krukau, A. V.; Vydrov, O. A.; Izmaylov, A. F.; Scuseria, G. E. *J. Chem. Phys.* **2006**, *125*.
- (31) Heyd, J.; Scuseria, G. E. *Journal Chem. Phys.* **2004**, *121*, 1187–1192.
- (32) Borlido, P.; Aull, T.; Huran, A. W.; Tran, F.; Marques, M. A. L.; Botti, S. *J. Chem. Theory Comput.* **2019**, *15*, 5069–5079.
- (33) Hoang, K.; Johannes, M. D. *J. Condens. Matter Phys.* **2018**, *30*, 293001.

Methodology

4.1 Methodological considerations for defect modelling

We now turn to the practicalities of solving the equations set out in Chapter 2 using DFT. Let us begin by restating the equations for the concentration and formation energy of defect X in charge state q ($[X^q]$ and $\Delta E_f^{X^q}$ respectively)¹

$$[X^q] = N_X g_q \exp\left(-\frac{\Delta E_f^{X^q}}{k_B T}\right) \quad (4.1)$$

$$\Delta E_f^{X^q} = \overbrace{(E_{\text{tot}}^{X^q} - E_{\text{tot}}^{\text{host}})}^{\Delta E^{X^q}} + \sum_i^{\mu_{\text{ion}}} n_i \mu_i + \overbrace{q E_{\text{Fermi}}^{\text{Fermi}}}^{E_{\text{Fermi}}^{\text{Fermi}}}. \quad (4.2)$$

In this section, we will discuss the practical approach taken to calculate defect formation energies in this work, including a discussion of potential sources of error in the methodology and how they are accounted for via a termwise examination of Equation (4.2).

4.1.1 “Raw” defect energies, ΔE^{X^q}

¹ A reminder of the terms in these equations

N_X site degeneracy

g_q (intrinsic) degeneracy

k_B Boltzmann constant

T temperature

$E_{\text{tot}}^{X^q}$ total energy of defective material

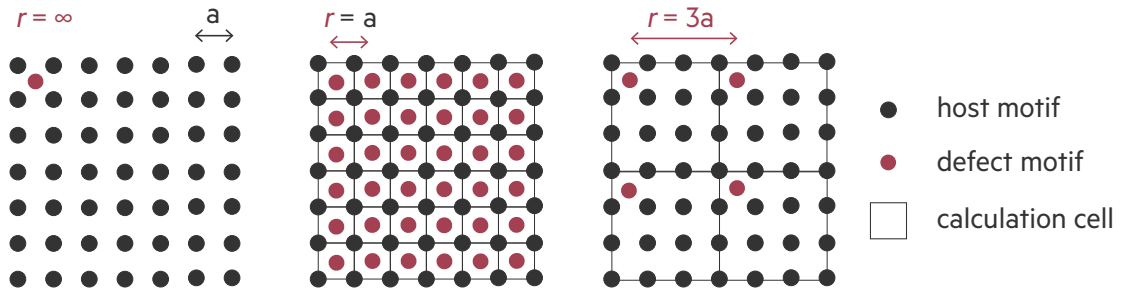
$E_{\text{tot}}^{\text{bulk}}$ total energy of the bulk material

n_i number of ions of kind i that form the defect

μ_i chemical potential of ions of kind i that form the defect

q defect charge state

$E_{\text{Fermi}}^{\text{Fermi}}$ Fermi energy



The use of periodic DFT and the study of point defects appear to be at odds with one another; typical DFT calculations of extended crystalline systems exploit symmetry to approximate experimentally relevant length-scales by modelling an infinite system (see Section 3.3). The use of a sym-

Figure 4.1: The **left-hand** panel shows a 2D representation of the system we are trying to model: $r_{\text{defect-defect}} = \infty$. The **middle** panel illustrates the issue with using a symmetry reduced structure to model the defect: it results in short defect-defect separations, and therefore large defect-defect interactions. The **right-hand** panel shows a compromise between the two approaches, a 3×3 supercell of the primitive cell.

metry reduced input structure will cause issues when modelling a defect: periodic repetitions of the calculation cell give rise to spurious energy contributions from the interactions between the periodic images of the defect. The energy contributions from these unphysical interactions will decay as the separation between defect images increases, meaning we can minimise these energy contributions using an expansion of smaller cells, a *supercell* (Figure 4.1). The supercell method is widely used for modelling point defects due to its conceptual simplicity and broad applicability to different materials [1–3].

In principle, we would incrementally increase the size of the supercell until the ΔE^{X^q} term in Equation (4.2) becomes constant with respect to further increases in supercell size. At this point, we would deem the interaction between defect images satisfactorily minimised. However, the Coulomb interaction between defect images is relatively long-ranged [4, 5], meaning impractically large calculation cells are needed to entirely remove this energy contribution (other interactions, such as structural effects, can be accommodated for on typical DFT calculation length scales [6]). Therefore, in addition to utilising a supercell, an *image-charge* correction is added to the calculated energy to restore the dilute limit.

Treating defect images as point charges, their interaction can be calculated as

$$E_M = -\frac{q^2\alpha}{2\epsilon r} \quad (4.3)$$

where q is the defect charge, α is the Madelung constant, r is the distance between the charges, and ϵ is the dielectric constant² [8]. This approximation allows us to directly calculate the electrostatic interaction between defect images, and include it in Equation (4.2). However, the finite size of our supercell perturbs the charge density from that of the bulk material meaning that the interaction between periodic images of the defect cannot be treated as point charges screened by the ideal dielectric medium of the bulk [9, 10]. A model proposed by Lany and Zunger, applies a scaling factor to Equation (4.3) accounting for this non-ideal screening [6].

$$E_{icc}^{LZ} = [1 + c_{sh}(1 - \epsilon^{-1})] \frac{q^2\alpha}{2\epsilon r}. \quad (4.5)$$

In the above c_{sh} is the “shape factor” of the cell, which has been calculated for a range of common supercells [11]. It was noted that for a cubic system, this prefactor often reduces $\approx 2/3$, leading to a pleasingly simple correction term, yet one that remains robust [6, 12]. This method was generalised for anisotropic systems by Murphy and Hine by utilising a dielectric tensor as opposed to a single dielectric constant [13]; both the Lany and Zunger image-charge correction and the Murphy and Hine

² The dielectric constant is comprised of charge screening contributions from the ions and electrons. These terms are additive within the Born-Oppenheimer approximation

$$\epsilon = \epsilon_{ionic} + \epsilon_{elec}. \quad (4.4)$$

The two terms are calculable within density functional perturbation theory [7].

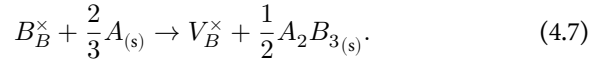
extension are used in this work.

4.1.2 Atomic chemical potentials, μ_{ion}

Synthesis conditions offer a means to control defect chemistry. Consider some material A_2B_3 : if the amount of element A were to be restricted during the synthesis of A_2B_3 , then the formation of V_B^\times may proceed as

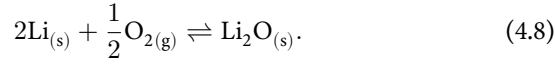


However, if A were in excess, the vacancy formation could instead proceed via the reaction



These two cases, each defined by the respective reactions, will give different vacancy formation energies. Within the models used for studying the defect properties of solid electrolytes in this dissertation, the variable ‘abundance’ of constituent elements during defect formation is accounted for by the μ_{ion} term in Equation (4.2) (the equation for the formation energy of defect X in charge state q). This is not a free variable, it is bounded by the stability limits of the host material [14].

Consider, as an example, Li_2O . Its formation is defined by the reaction



The chemical potential μ_i (where $i = \text{Li}$ or O) is the rate of change of free energy with the number of atoms of i that are added to the system. When reaction eq. (4.8) is in equilibrium, the free energy is at a minimum, and so the sum over chemical potentials is 0,

$$2\mu_{\text{Li}} + \mu_{\text{O}} - \mu_{\text{Li}_2\text{O}} = 0 \quad (4.9)$$

$$2\mu_{\text{Li}} + \mu_{\text{O}} = \mu_{\text{Li}_2\text{O}}. \quad (4.10)$$

We define our chemical potentials such that $\mu_i = E_i^0 + \Delta\mu_i$ where E_i^0 is the elemental reference energy (its DFT calculated energy in its standard state), and $\Delta\mu_i$ defines the deviation from this reference energy owing to differing growth conditions. We can then write

$$2(E_{\text{Li}}^0 + \Delta\mu_{\text{Li}}) + (E_{\text{O}}^0 + \Delta\mu_{\text{O}}) = (E_{\text{Li}_2\text{O}}^0 + \Delta\mu_{\text{Li}_2\text{O}}) \quad (4.11)$$

$$2\Delta\mu_{\text{Li}} + \Delta\mu_{\text{O}} = \underbrace{(E_{\text{Li}_2\text{O}}^0 + \Delta\mu_{\text{Li}_2\text{O}}) - 2E_{\text{Li}}^0 - E_{\text{O}}^0}_{\Delta E_{\text{f}}^{\text{Li}_2\text{O}}} \quad (4.12)$$

$$2\Delta\mu_{\text{Li}} + \Delta\mu_{\text{O}} = \Delta E_{\text{f}}^{\text{Li}_2\text{O}}. \quad (4.13)$$

Equation (4.13) highlights the mutual dependence of $\Delta\mu_{\text{Li}}$ and $\Delta\mu_{\text{O}}$. These elemental chemical potentials are also further bound by the constraints

$$\Delta\mu_{\text{Li}} \leq 0, \text{ and } \Delta\mu_{\text{O}} \leq 0. \quad (4.14)$$

Outside of these bounds Li_2O is unstable with respect to decomposition to form one of the pure elements. Taking Equations (4.13) and (4.14) together, we can therefore write the oxygen-rich–lithium-poor limit as

$$\Delta\mu_{\text{O}} = 0 \text{ eV}, \quad (4.15)$$

therefore,

$$\Delta\mu_{\text{Li}} = \frac{\Delta E_{\text{f}}^{\text{Li}_2\text{O}}}{2}. \quad (4.16)$$

and the lithium-rich–oxygen-poor limit as

$$\Delta\mu_{\text{Li}} = 0 \text{ eV}, \quad (4.17)$$

and

$$\Delta\mu_{\text{O}} = \Delta E_{\text{f}}^{\text{Li}_2\text{O}}. \quad (4.18)$$

The existence of competing phases adds further bounds on reasonable limits for $\Delta\mu_i$. In the present case, the formation of lithium peroxide should be avoided, and as such, $\Delta\mu_{\text{Li}}$ and $\Delta\mu_{\text{O}}$ are subject to the additional constraint

$$2\Delta\mu_{\text{Li}} + 2\Delta\mu_{\text{O}} \leq \Delta E_{\text{f}}^{\text{Li}_2\text{O}_2}. \quad (4.19)$$

For any binary compound A_xB_y , the limits described can be generalised as

$$x\Delta\mu_A + y\Delta\mu_B = \Delta E_{\text{f}}^{A_xB_y} \quad (4.20)$$

$$p\Delta\mu_A + q\Delta\mu_B \leq E_{\text{f}}^{A_pB_q} \quad (4.21)$$

$$\Delta\mu_A \leq 0 \quad (4.22)$$

$$\Delta\mu_B \leq 0. \quad (4.23)$$

For ternary systems and above, the number of independent variables and equations defining their limits increases. However, the solving for the chemical potential limits remains a number of simultaneous linear equations in a number of variables, and so is soluble and amenable to programmatic solution. We have used the Chemical Potential Limits Analysis Program (CPLAP) to automate the solution [15].

4.1.3 Electronic chemical potential E_{Fermi}

Defect formation does not, in general, only involve adding or removing neutral atoms. It may also involve adding or removing electrons, and the energetic cost of this must also be included in the defect formation energy. The chemical potential of the electrons added to or removed from the system during defect formation is given by the Fermi energy. It is both conventional and useful to define the Fermi energy in reference to the energy of the highest occupied state in the valance band of the host material, the valence band maximum (VBM), such that $\Delta E_{\text{Fermi}} = E_{\text{Fermi}} - E_{\text{vbm}}^{\text{host}}$. Charged point defect calculations in periodic DFT, however, introduce a mismatch between the Kohn-Sham eigenvalues in the host and defect cells. When calculating the energy of a system with a net charge ($q \neq 0$) a uniform charge applied over the whole calculation cell is introduced that neutralises the overall charge of the cell, while only interacting weakly with the “real” charge associated with the defect.³ The result is that the energies of the defective cell and the host cell are solved with respect to a different reference electrostatic potential, causing the mismatch in the band energies of the material [10]. This shift is unphysical; we would expect the bulk-like properties of the defect cell to be identical to the host cell (see Figure 4.2). A correction must therefore be applied to align the position of the VBM in the two calculations, restoring the bulk characteristics of the region in the defect supercell that is far from the defect. Potentials, V , can be aligned according to

$$E_{\text{pot}}^{X,q} = q[V^{X,q} - V^{\text{bulk}}], \quad (4.24)$$

allowing direct comparison of the total energies of the two systems. In practice, to obtain these potentials, an average is taken over core potentials of all ions not in the immediate vicinity of the defect in both cells [6].

4.1.4 Reevaluating the equation for defect formation energy

We can now reformulate Equation (4.2) to include terms that account for the methodology used in this work,

$$\Delta E_{\text{f}}^{X,q} = \Delta E^{X,q} + \sum_i n_i (E_i^0 + \Delta\mu_i) + q(E_{\text{Fermi}} + E_{\text{vbm}}^{\text{host}} + E_{\text{pot}}^{X,q}) + E_{\text{icc}} \quad (4.25)$$

where the changes as compared to the previous version are the decomposition of μ_i into the reference energy of the element E_i^0 and the shift in chemical potential due to growth conditions $\Delta\mu_i$. Similarly, the electron chemical potential is now made up of contributions from a reference

³ This uniform background charge is known as a jellium.

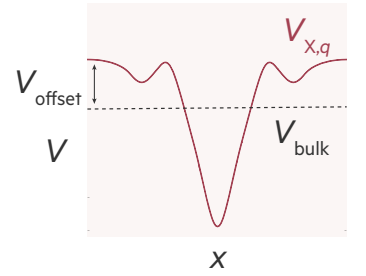


Figure 4.2: In some arbitrary material, the average electrostatic potential of a bulk calculation in x is shown by a dotted grey line. The potential of the same cell containing defect X^q is shown in red, where the offset between the electrostatic potential in host cell and the bulk region of the defective cell is labelled as V_{offset} .

energy, $E_{\text{vbm}}^{\text{host}}$ and a shift in that energy ΔE_{Fermi} , corrected for the misalignment of electronic energy levels $E_{\text{pot}}^{X^q}$, and with an image charge correction added, E_{icc} .

4.2 Additional methods

4.2.1 Structure optimisation

Kohn-Sham DFT relies on approximations for the quantum mechanical properties of electrons: the charge density returned by a Kohn-Sham DFT calculation is sensitive to the choice of functional (along with many other calculation parameters), and as such, the forces between atoms are unlikely to match experimentally reported structures, even at 0 K. It is therefore best practice to relax our calculation cell using our chosen exchange-correlation functional before attempting to extract meaningful data. This will prevent contributions to the DFT-calculated total energy arising from spurious forces between the atoms. To ensure we are solving a local minimisation problem we take an experimental structure as our trial structure, calculate the force on each atom, perturb the ionic configuration to reduce the calculated forces, and repeat until the forces are reduced to within some specified tolerance ($\sim 0 \text{ eV \AA}^{-1}$).⁴

⁴ A typical value used in this work is $0.001 \text{ eV \AA}^{-1}$

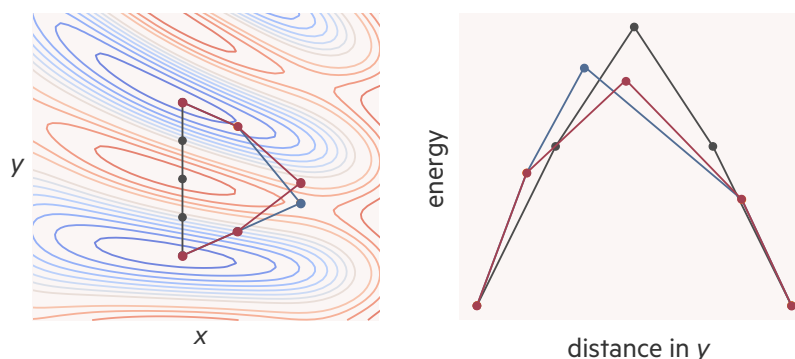
The Hellmann-Feynman theorem states that the force on any fixed nucleus in a system of nuclei and electrons can be obtained from classical electrostatics [16, 17]. The force can therefore be estimated directly from the charge density, which is available from DFT. Once there are zero net forces on each ion, the minimum energy ionic configuration has been reached. The Hellmann-Feynman theorem also allows for the optimisation of cell shape and volume, as well as ionic positions.

One must be careful when following such a ‘complete’ structural relaxation owing to the potential inadvertent introduction of *Pulay stress*: lattice volume changes can result in an incomplete plane-wave basis set introducing small errors into the stress tensor [18]. Pulay stress can be avoided in one of two ways, both of which have been employed in different instances in this work: the energy of a series of fixed-volume DFT calculations can be fit to an equation of state to obtain an equilibrium volume, sidestepping the issue of using a volume dependent basis set entirely, or the plane-wave energy cutoff is raised significantly above the value determined during convergence testing, minimising Pulay stress.

4.2.2 Nudged elastic band

The nudged elastic band (NEB) method is used to investigate potential energy surfaces, typically concerned with finding transition states energies

Figure 4.3: **Left** An arbitrary potential energy surface in which a more red contour indicates a higher energy, and blue contours indicate a low energy traversed with a linear interpolation (grey), a nudged elastic band minimised pathway, using the interpolated path as an initial guess (blue), and the same pathway subjected to a climbing image algorithm to find a local maxima in the pathway (red); **right** the energy associated with that pathway, with the energy profile represented by the same colour as the pathway shown on the plot above.



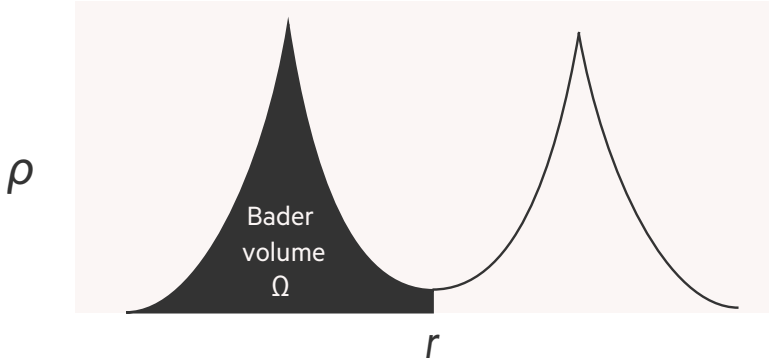
and structures. It is often used as a means to investigate the motion of point defects. It requires a reasonable “guess” at what the pathway for ionic motion might look like. A typical NEB workflow involves defining endpoints for ionic motion and relaxation of those endpoints. Once the endpoint geometries are known, some interpolation scheme is used to generate images along a pathway between them. This interpolation is often linear, however, some more sophisticated methods are available including pre-minimisation using simple potential models [19, 20].

The images along the pathway are then allowed to relax. To prevent the structures from simply collapsing into the endpoints, the images are linked to their adjacent images by a spring force, much like they were held together by a taut elastic band. The minimisation of the replicas takes place simultaneously, resulting in the ‘band’ locating the pathway of minimum energy for the migrating ion. The minimisation is guided by a force projection comprised of the spring forces along the band, and the ‘real’ forces acting on the ions perpendicular to the band. The highest energy image is often subject to an inverse force when it is close to the transition state to find the true minimum energy pathway for single ion migration, this is known as ‘climbing image’ NEB (CI-NEB) [21]. The differences between NEB and CI-NEB are represented pictorially in Figure 4.3.

4.2.3 Bader charge partitioning

DFT calculations output the electron density, which means to assign charges to atoms, we need to associate some volume of the charge density with each atom. There are a range of charge-partitioning schemes, the one used in this thesis is Bader charge analysis [22]. Within this scheme, we define an atomic volume as a region of space that lies within all zero-flux surfaces surrounding a maximum in the charge density, taken as the position of the nucleus. We can then assign the atomic partial charge as the difference between the integral of the charge density over space

Figure 4.4: 2D representation of the Bader charge partitioning scheme.



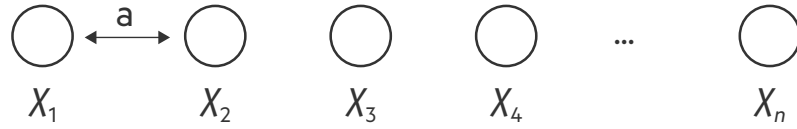
that occupies each atomic volume (number of electrons) and the nuclear charge,

$$q = Z - \int_{\Omega} \rho(r) dr \quad (4.26)$$

where Ω is the atomic volume. This approach to partitioning charge is illustrated in Figure 4.4.

4.2.4 Band structure

Figure 4.5: 1D chain of 1s basis functions where n is the lattice point index and χ is a 1s basis function associated with each lattice point (as indicated) by the subscript index.



A band structure refers to a plot of the electronic eigenvalues (energies) as a function of the wave vector \mathbf{k} . Consider a 1D chain of hydrogen atoms with spacing a and lattice points indexed by n , each 1s basis function is labelled χ_n . This scenario is illustrated in Figure 4.5. The Bloch sum over these bases is given by

$$\psi_{\mathbf{k}} = \sum_n \exp(i\mathbf{k}na) \chi_n. \quad (4.27)$$

When $\mathbf{k} = 0$,

$$\psi_0 = \sum_n \exp(0) \chi_n = \sum_n \chi_n = \chi_0 + \chi_1, \dots, + \chi_n \quad (4.28)$$

we reach a solution where all basis functions are in-phase, which corresponds to a maximally bonding interaction. Taking \mathbf{k} as π/a ,

$$\psi_{\frac{\pi}{a}} = \sum_n \exp(\pi in) \chi_n = \sum_n (-1)^n \chi_n, \quad (4.29)$$

all basis functions are out of phase with their nearest neighbours, which

corresponds to a maximally antibonding solution. Evaluating \mathbf{k} for any value outside the range $|\mathbf{k}| \leq \pi/a$ returns a non-unique result: this range of \mathbf{k} is the first Brillouin zone (see Section 3.3).

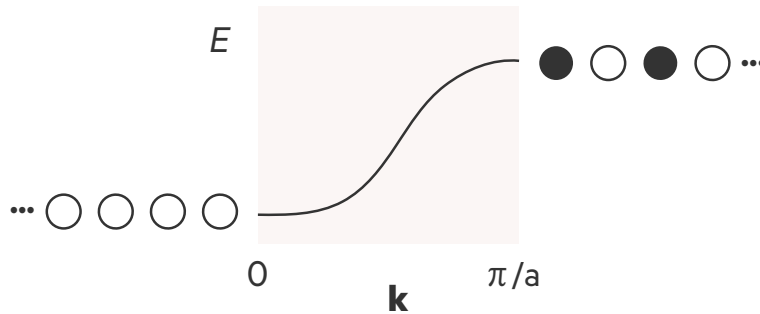


Figure 4.6: Band structure for a 1D hydrogen chain. Values of $\mathbf{k} \sim 0$ are low energy in-phase solutions, values at $\sim \pi/a$ are high energy out-of-phase interactions.

The band structure for a 1D hydrogen chain is shown in Figure 4.6. The band structure contains useful information for understanding electronic conductivity. The curvature or dispersion of a band can be used to calculate electronic carrier effective mass m^* , which is related to the mobility of an electron (or hole) μ by

$$\mu = \frac{e\tau}{m^*} \quad (4.30)$$

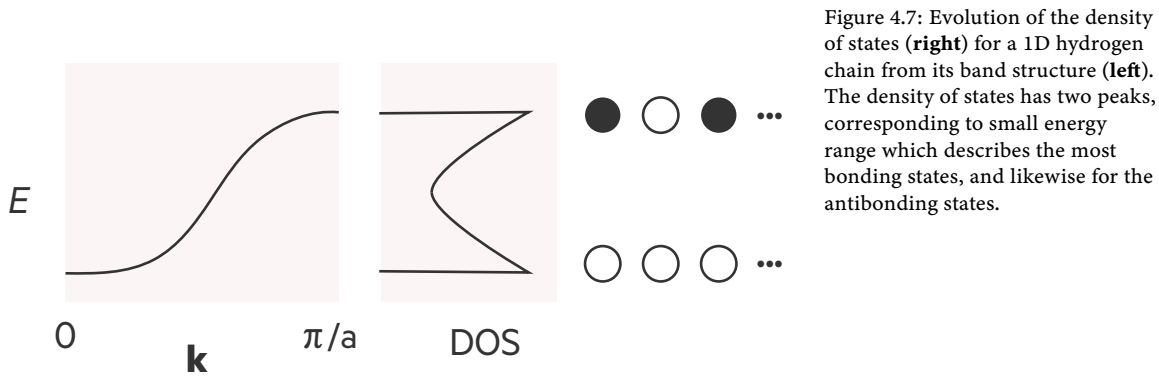
where τ is the average scattering time [23, 24]. The calculation of τ is non-trivial, and so effective masses are often taken as an indicator of potential electron and hole mobility (see Chapter 7 for more discussion of electron and hole mobility in solid state electrolytes). m^* is often calculated as

$$\frac{\hbar}{m^*} = \frac{d^2 E(\mathbf{k})}{d\mathbf{k}^2}, \quad (4.31)$$

where $d^2 E(\mathbf{k})/d\mathbf{k}^2$ is the curvature of the band relevant for the charge carrier in question, i.e. for a dilute concentration of free electrons, we would take the band curvature at the conduction band minimum [24]. The band dispersion is determined by the overlap between neighboring bases. Simply, if we compress the distance between lattice points, the bonding interactions will strengthen, and the antibonding interactions will destabilize further. This will result in larger changes in energy for the same change in \mathbf{k} .

4.2.5 Density of states

We can collect the states over a given energy range together, and sum them to give a *Density of States* (DOS) ($g(E)$) which gives us another way to represent the electronic structure of our material. Pictorially, we can see how a DOS arises from a band structure in Figure 4.7: it is proportional to



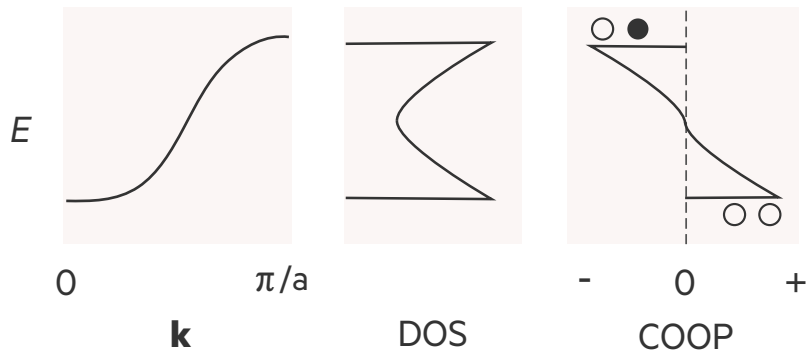
the reciprocal gradient of the band structure,

$$g(E) \sim \left(\frac{dk}{dE} \right)^{-1}. \tag{4.32}$$

This also means that qualitative information can be drawn from the DOS about band dispersion, and electron mobility: a wide, flat DOS indicates a sharp gradient in the band dispersion, indicating disperse bands with mobile electrons, whereas sharp changes in the DOS indicate flat bands and localised states.

4.2.6 Bonding analysis

Figure 4.8: Relationship between the COOP (right), density of states (middle) and band structure (left) for a 1D hydrogen chain. The COOP is positive for bonding interactions, negative for anti-bonding interactions, and ~ 0 for non-bonding interactions.



DFT is a somewhat “bonding-agnostic” approach, in that the outputted charge density does not tell us anything directly about the nature of the bonding interactions in the calculated system. In addition, assigning chemical character to the Bloch functions is not intuitive: despite the useful nature of modelling an infinite system in Bloch functions, how these relate to a chemical picture is not obvious.

Considering that both a linear combination of atomic orbitals (LCAO) and a set of plane waves are an appropriate basis set for solving the Schrödinger equation, and the Hohenburg and Kohn theorems tell us that there is only one ground state electron density, despite the fact it is

expressed in a different basis, there must be some transformation that can be applied between these descriptions [25],

$$\Psi_{\text{plane-wave}} = \Psi_{\text{LCAO}} = \sum_i \sum_n^m c_i \phi_i. \quad (4.33)$$

In the LCAO basis, n is the n^{th} basis function in the set of all basis functions m , and $c_{n,i}$ is the mixing coefficient of the hydrogenic orbital, ϕ_i . Within an LCAO basis set, orbitals can be related to different atoms explicitly, which allows us write an atom or orbital projected density of states (pDOS) as

$$\text{pDOS}_i(E) = \sum_n^m |c_i^n|^2 \delta(E - E_i). \quad (4.34)$$

Additionally, we can define an overlap population between orbitals i and j , P_{ij} ,

$$P_{ij} = S_{ij} \sum_n^m c_{ij}^* c_{nj} \quad (4.35)$$

where S_{ij} is the overlap integral between ϕ_i and ϕ_j . An overlap population weighted DOS, or ‘‘Crystal Orbital Overlap Population’’ (COOP) can then be written as

$$\text{COOP}_{ij}(E) = S_{i,j} \sum_n^m f c_{ni}^* c_{nj} \delta(E - E_i) \quad (4.36)$$

in which f is the occupation number of orbitals we compute the COOP between [26]. The relationship between the band structure, density of states, and COOP of a linear chain of hydrogen is shown in Figure 4.8. To show how orbital topology can affect the COOP, we also compare the schematic COOP for a linear hydrogen chain, and a ‘‘kinked’’ hydrogen chain in Figure 4.9.

To summarise the general characteristics of these curves, positive regions are bonding, negative regions are antibonding, the amplitudes are related to the number of states in that energy interval and the magnitude of the overlap (illustrated by the smaller maxima for the 1-3 interactions in Figure 4.9) The integral up to the Fermi energy (iCOOP) gives a proxy metric for bond-order. Equivalently, we can consider the energy contribution associated with each bond to the total energy, and we resolve a related metric, the ‘‘Crystal Orbital Hamilton Population’’ (COHP), the integral of which (iCOHP) up to the Fermi level gives a proxy metric for the bond energy [27]. To access this information starting from a periodic Kohn-Sham orbital description, the output wave function is first converted to a linear combination of atomic orbitals solution using the code `LOBSTER`

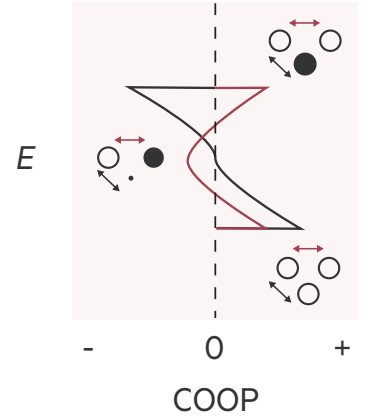


Figure 4.9: Comparison of the COOP between nearest neighbour (1-2) interactions (black) and next-nearest neighbour (1-3) interactions (red) for a ‘‘kinked’’ hydrogen chain. The maxima of the red curve are lower, as the distance between centres are increased, reducing the magnitude of the overlap population.

[25].

Bibliography

- (1) Buerger, M. J. *J. Chem. Phys.* **1947**, *15*, 1–16.
- (2) Freysoldt, C.; Grabowski, B.; Hickel, T.; Neugebauer, J.; Kresse, G.; Janotti, A.; Van de Walle, C. G. *Rev. Mod. Phys.* **2014**, *86*, 253–305.
- (3) Kim, S.; Hood, S.; Park, J.; Whalley, L.; Walsh, A. *J. Phys.: Energy* **2020**.
- (4) Hine, N. D. M.; Frensch, K.; Foulkes, W. M. C.; Finnis, M. W. *Phys. Rev. B* **2009**, *79*, 024112.
- (5) Goedecker, S. *Rev. Mod. Phys.* **1999**, *71*, 1085–1123.
- (6) Lany, S.; Zunger, A. *Phys. Rev. B* **2008**, *78*, 235104.
- (7) Baroni, S.; de Gironcoli, S.; Dal Corso, A.; Giannozzi, P. *Rev. Mod. Phys.* **2001**, *73*, 515–562.
- (8) Leslie, M.; Gillan, N. J. *J. Phys. C Solid State Phys.* **1985**, *18*, 973–982.
- (9) Makov, G.; Payne, M. C. *Phys. Rev. B* **1995**, *51*, 4014–4022.
- (10) Durrant, T. R.; Murphy, S. T.; Watkins, M. B.; Shluger, A. L. *J. Chem. Phys.* **2018**, *149*, 024103.
- (11) Lany, S.; Zunger, A. *Model. Simul. Mater. Sci. Eng.* **2009**, *17*, 084002.
- (12) Lambert, D. S.; Murphy, S. T.; Lennon, A.; Burr, P. A. *RSC Adv.* **2017**, *7*, 53810–53821.
- (13) Murphy, S. T.; Hine, N. D. M. *Phys. Rev. B* **2013**, *87*, 094111.
- (14) Zhang, S. B.; Northrup, J. E. *Phys. Rev. Lett.* **1991**, *67*, 2339–2342.
- (15) Buckeridge, J.; Scanlon, D.; Walsh, A.; Catlow, C. *Comput. Phys. Commun.* **2014**, *185*, 330–338.
- (16) Hellmann, H. *Angew. Chem.* **1941**, *54*, 156–156.
- (17) Feynman, R. P. *Phys. Rev.* **1939**, *56*, 340–343.
- (18) Francis, G. P.; Payne, M. C. *J. Condens. Matter Phys.* **1990**, *2*, 4395–4404.
- (19) Kolsbjerg, E. L.; Groves, M. N.; Hammer, B. *J. Chem. Phys.* **2016**, *145*, 094107.
- (20) Rong, Z.; Kitchaev, D.; Canepa, P.; Huang, W.; Ceder, G. *J. Chem. Phys.* **2016**, *145*, 074112.
- (21) Henkelman, G.; Uberuaga, B. P.; Jónsson, H. *J. Chem. Phys.* **2000**, *113*, 9901–9904.

- (22) Bader, R. F. W., *Atoms in Molecules*, 1990.
- (23) Drude, P. *Annalen der Physik* **1900**, 306, 566–613.
- (24) Ashcroft, N. W., *Solid State Physics*; Cengage Learning: 1976.
- (25) Deringer, V. L.; Tchougreff, A. L.; Dronskowski, R. *J. Phys. Chem. A* **2011**, 115, 5461–5466.
- (26) Hoffmann, R. *Angew. Chem. Int. Ed Engl.* **1987**, 26, 846–878.
- (27) Dronskowski, R.; Bloechl, P. E. *J. Phys. Chem.* **1993**, 97, 8617–8624.

Statement of Authorship

The following chapter concerns the article entitled **Aliovalent doping response and impact on ionic conductivity in the antiperovskite solid electrolyte Li_3OCl** currently **in review** and has been made available on ChemRxiv (available under the DOI [10.33774/chemrxiv-2021-hzr1s](https://doi.org/10.33774/chemrxiv-2021-hzr1s)).

This preprint reports on original research I conducted during the period of my Higher Degree by Research candidature.

Personal contributions: Formulation of ideas (80%): I conceptualised the work, and designed the initial study with input from Dr Benjamin Morgan, Jacob Dean later highlighted that it would be interesting to directly estimate conductivities from the defect-concentration data. Design of methodology (80%): After carrying out the defect calculations and modelling the aliovalent doping chemistry, appropriate approximations for modelling the ionic conductivity were discussed between all authors. Experimental work (100%): I carried out all practical aspects of the work. Presentation of data in journal format (70%): The first drafts of the preprint were written by myself with input from Dr Benjamin Morgan. The finalised manuscript was prepared by Dr. Benjamin Morgan and myself with input from all co-authors.

Signed:



Date:

15 / 3 / 22

Context

This work concerns the defect chemistry and aliovalent doping response of the antiperovskite-structured candidate solid–electrolyte Li_3OCl . Despite potential issues surrounding synthesability [1], this material serves as exemplar for studying the defect chemistry and doping response of antiperovskite solid-electrolytes owing to the apparent commonality between key features of the defect chemistry of this material and other compositions with the same structure. In antiperovskite solid-electrolytes and structurally related materials, it is often found that the charge-carrying interstitial has a much higher mobility than the vacancy, but the mobile-ion Frenkel pair typically has a significantly higher formation energy than the mobile-ion Schottky defect [2–7]. This suggests the concentration of vacancies is higher than the concentration of interstitial in undoped antiperovskites. These observations have led to the suggestion of two different doping strategies to increase ionic conductivity: increase the concentration of the majority charge carrier—the mobile-ion vacancy—via supervalent doping [8], or to increase the concentration of the mobile-ion interstitial to the point where it becomes the majority charge carrier to exploit its high mobility via subvalent doping [9]. In this chapter we assess the expected efficiency of these two proposed doping strategies for increasing the ionic conductivity. We also touch on whether the general features of the defect chemistry of Li_3OCl are indeed applicable to other antiperovskite solid electrolytes.

We argue that the asymmetric doping response of Li_3OCl is a consequence of a lower energy Schottky defect as opposed to Frenkel pair, or rather than the Fermi energy is pinned by the formation of V_{Li}' and V_{Cl}^\bullet defects. With the caveat that the lowest energy negative defect can also be O_{Cl}' . Crucially, the V_{Li}' remains low energy at the self consistent Fermi energy, whereas the energy of the lithium interstitial is typically ~ 1 eV higher, therefore, subvalent doping will primarily be charge compensated by the formation of V_{Cl}^\bullet defects, and supervalent doping will be compensated by a combination of V_{Li}' and O_{Cl}' defects, depending on the chemical potential regime. As the low energy Schottky defect appears common across antiperovskites solid electrolytes, this result, in the absence of other complicating factors, should be general. Harnessing the high mobility of the mobile interstitial within this structural family remains tantalising for battery applications, yet proves challenging.

This chapter follows the same structure as the associated preprint (see statement of authorship), however, it has been edited to remove information that is redundant within the context of this thesis and to better reflect the overall narrative of this dissertation.

5.1 Introduction

The effectiveness of aliovalent doping to enhance ionic conductivity in lithium-ion solid electrolytes through increasing the concentrations of charge-carrying mobile defects depends on two conditions. First, aliovalent doping should preferentially increase the concentrations of charge-carrying mobile defects ahead of competing immobile defects: doping should preferentially increase the concentration of either lithium vacancies or lithium interstitials. Second, any increase in the concentration of charge-carrying defects should produce a corresponding increase in ionic conductivity. This may not be the case if the ionic conductivity has some dependence on defects other than those being targeted through doping. In solid electrolytes that contain more than one charge-carrying defect species, increasing the concentration of the minority defect species may have little practical effect on the overall ionic conductivity. Alternatively, where there are strong interactions between dopant atoms and oppositely charged mobile defect species, these mobile defects may be kinetically trapped, resulting in a net decrease in ionic conductivity [8, 9]. These potential complications mean that aliovalent doping of solid electrolytes is not guaranteed to produce a significant increase in ionic conductivity, and predicting the effectiveness of a specific aliovalent doping strategy requires characterising the response to doping of all relevant defects in the system of interest.

One lithium-ion solid electrolyte for which a number of aliovalent doping schemes have been proposed is the antiperovskite Li_3OCl [8–12] (Fig. 5.1). Li_3OCl has been widely studied following initial reports of room-temperature ionic conductivities up to $\sim 1 \times 10^{-3} \text{ S cm}^{-1}$ [13]. This reported high ionic conductivity is notable because the lithium ions in Li_3OCl are crystallographically ordered; this is in contrast to other high-ionic-conductivity lithium-ion solid electrolytes, such as lithium thiophosphates, in which lithium is typically disordered, with this disorder thought to be integral to their fast ion diffusion [14–19].

In Li_3OCl , ionic conductivity is attributed to the diffusion of mobile point defects—specifically lithium vacancies and lithium interstitials [2, 20–22]. Lithium vacancies and interstitials in Li_3OCl are both predicted to be mobile at room temperature, with calculated diffusion barriers of $\sim 0.3 \text{ eV}$ and $\sim 0.15 \text{ eV}$, respectively [2, 20–22]. While these diffusion barriers indicate that lithium interstitials are significantly more mobile than lithium vacancies, calculated defect-pair formation energies give a lower formation energy for $V_{\text{Li}} + V_{\text{Cl}}$ Schottky pairs (1.0–1.6 eV) than for $V_{\text{Li}} + \text{Li}_i$ Frenkel pairs (1.9–2.5 eV) [21, 23, 24], making lithium vacancies the expected dominant charge-carrying defect species in undoped Li_3OCl .

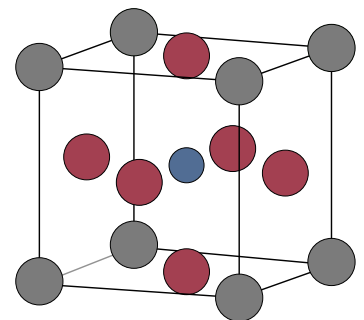


Figure 5.1: The antiperovskite crystal structure. In the case of Li_3OCl , the red sites are occupied by lithium ions, the grey sites by chlorine, and the blue by oxygen.

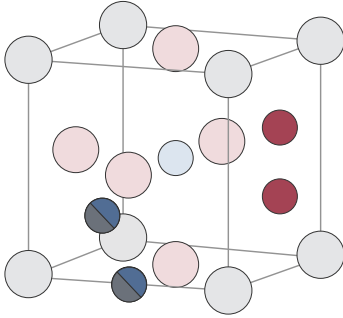


Figure 5.2: The interstitial sites considered in the antiperovskite crystal structure. Anion interstitials are shown in split grey-blue at $(\frac{1}{4}, \frac{1}{4}, \frac{1}{4})$ and $(\frac{1}{2}, 0, 0)$, and the lithium “dumbbell” interstitialcy defect as described by Emly *et al.* [21] is shown in red. For consistency with the literature we refer to this defect simply as a lithium interstitial.

Both supervalent and subvalent doping strategies have been proposed to enhance the ionic conductivity of Li_3OCl [8, 9, 12, 20, 21, 25, 26]. Supervalent doping—e.g., where a cation such as Mg^{2+} or Al^{3+} replaces Li^+ —has been proposed as an effective route to increase the concentration of lithium vacancies [8, 12, 20, 21, 25, 26], while subvalent doping—e.g., where an anion such as S^{2-} replaces Cl^- —has been proposed as an effective route to increase the concentration of lithium interstitials [9].

Several of the characteristic properties of Li_3OCl —a high degree of crystallographic ordering of mobile ions; low Schottky-pair formation energies, giving much higher concentrations of mobile vacancies than mobile interstitials; and higher mobilities for these interstitials than for corresponding vacancies—are shared by a number of other antiperovskite and structurally-related solid electrolytes [2–7]. Understanding the effectiveness of different aliovalent doping schemes in Li_3OCl is useful, therefore, not only because it may help direct the optimisation of ionic conductivity for this one material, but also because it can provide more general insights into doping responses for this class of solid electrolytes.

In this chapter, we describe a hybrid density-functional theory (DFT) study of Li_3OCl that considers all native vacancy, interstitial, and anion antisite defects [27, 28], which we have performed in order to characterise the native defect chemistry of Li_3OCl , and to model the effect of supervalent and subvalent doping on native defect concentrations and ionic conductivity. The positions of the interstitial defects considered are shown in fig. 5.2. Under all considered synthesis conditions, we predict lithium vacancies to be present in much greater concentrations than lithium interstitials, in qualitative agreement with previous studies [3, 8, 9, 24, 29, 30], and confirming V_{Li} as the dominant charge carrier in nominally stoichiometric samples.

For doped Li_3OCl , supervalent doping is predicted to increase the concentration of both V_{Li} and O_{Cl} , with the preferentially formed defect depending on synthesis conditions, while subvalent doping is predicted to preferentially increase the concentration of V_{Cl} ahead of Li_i under all considered synthesis conditions. Supervalent doping is predicted to be effective at increasing the ionic conductivity, particularly under Li-poor synthesis conditions. Subvalent doping at moderate doping levels, however, is predicted to *decrease* the room-temperature ionic conductivity, due to two complementary effects. First, subvalent doping at low-to-moderate dopant concentrations decreases the concentration of lithium vacancies more rapidly than it increases the concentration of lithium interstitials. Second, increasing the number of lithium interstitials formed under synthesis conditions causes increased “quenching” of lithium vacancies when cooling to room temperature through recombination of V_{Li} as $V_{\text{Li}} + \text{Li}_i$

Frenkel pairs. Although sufficiently high levels of subvalent doping are predicted to increase ionic conductivity relative to undoped Li_3OCl , the ionic conductivity thus obtained is significantly lower than predicted for supervalent doping at equivalent dopant concentrations. We therefore do not expect subvalent doping to be a practical doping strategy for increasing the ionic conductivity of Li_3OCl .

5.2 DFT calculation methodology

To calculate defect formation energies in Li_3OCl , we have performed a series of hybrid-DFT calculations using the plane-wave DFT code `VASP` [31, 32] using the HSE06 hybrid functional [33]. All calculations used a plane-wave basis cutoff of 520 eV and defect calculations were performed using a $3 \times 3 \times 3$ supercell of the Li_3OCl unit cell. Interactions between core and valence electrons were described using the projector augmented wave method [34] with cores of [H] for Li, [He] for O and [Ne] for Cl. To avoid spurious forces associated with Pulay stress, equilibrium volumes were calculated using a series of constant volume calculations and fitted to the Murnaghan equation of state [35]. Geometry optimisations were deemed converged when all atomic forces were smaller than 1×10^{-3} eV/Å. Supercell calculations used a $2 \times 2 \times 2$ Monkhorst-Pack grid for sampling \mathbf{k} -space.

Our calculations predict a lattice parameter for Li_3OCl of 3.82 Å, which slightly underestimates the experimental value of 3.91 Å [13] but is in good agreement with previous DFT calculations [12]. Our calculated value for the band gap of Li_3OCl of 6.6 eV compares well to previously calculated values of 6.4 eV [12, 21]; To the best of our knowledge the band gap of Li_3OCl has not yet been measured experimentally.

5.3 Defining a “synthetically accessible” chemical potential space for Li_3OCl

To calculate defect formation energies, and hence predict defect concentrations, it is necessary to define the accessible ranges of chemical potentials for the elemental species involved in the formation of each defect. In most defect studies, the relevant region of chemical potential space is constrained by the thermodynamic stability limits of the system under study with respect to competing phases [27]. Li_3OCl , however, is not thermodynamically stable, but is metastable with respect to formation of Li_2O and LiCl [21, 36]. Here, we follow the approach of Emly *et al.* and assume that the degradation of Li_3OCl to form Li_2O is kinetically suppressed, and therefore construct a metastable phase diagram with Li_2O removed as a competing phase [21]. The assumption that Li_3OCl is metastable

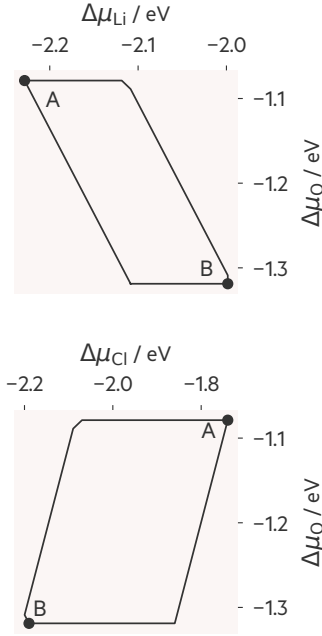


Figure 5.3: Two-dimensional projections of the “synthetically accessible” 3D chemical potential space for Li₃OCl. a) $\{\Delta\mu_{\text{Li}}, \Delta\mu_{\text{O}}\}$ projection. b) $\{\Delta\mu_{\text{Cl}}, \Delta\mu_{\text{O}}\}$ projection. For our defect and doping response calculations we consider the maximally lithium-rich and lithium-poor limits: Li-rich $\rightarrow \{\Delta\mu_{\text{Li}} = -2.00 \text{ eV}, \Delta\mu_{\text{Cl}} = -2.19 \text{ eV}, \Delta\mu_{\text{O}} = -1.32 \text{ eV}\}$; Li-poor $\rightarrow \{\Delta\mu_{\text{Li}} = -2.23 \text{ eV}, \Delta\mu_{\text{Cl}} = -1.75 \text{ eV}, \Delta\mu_{\text{O}} = -1.08 \text{ eV}\}$.

with respect to decomposition to Li₂O and LiCl is supported by a recent force-field-based atomistic modelling study that predicts excellent kinetic stability of Li₃OCl with respect to this decomposition pathway [37], although experimental synthesis of phase-pure crystalline Li₃OCl remains extremely challenging [5]. We have used the code `CPLAP` to identify this initial chemical potential region [38].

Li₃OCl is typically synthesised at 300–360 °C and under vacuum [13], therefore, to define a “synthetically accessible” chemical potential range for Li₃OCl we further restrict the region of predicted metastability by considering chemical potentials corresponding to these synthesis conditions, via

$$\Delta\mu_{\text{O}}(T, P) = \frac{1}{2} \left\{ C_p(T - T_0) - T \left[S_0 + C_p \ln \frac{T}{T_0} + k_B \ln \frac{P}{P_0} \right] \right\} \quad (5.1)$$

where T and P are synthesis temperatures and pressures respectively and k is the Boltzmann constant. We use the experimental value for the oxygen standard entropy, $S_0 = 205 \text{ J/mol/K}$ [39], and assume that oxygen behaves as an ideal gas and use $C_p = \frac{7}{2}k_B$ for the constant-pressure specific heat capacity per diatomic molecule [39–41]. The resulting “synthetically accessible” range of elemental chemical potentials defines a three-dimensional region of $\{\mu_{\text{O}}, \mu_{\text{Cl}}, \mu_{\text{Li}}\}$ chemical-potential space with six vertices (fig. 5.3). Within these six limiting conditions, we explicitly consider the maximally lithium-rich and lithium-poor conditions, corresponding to $\{\Delta\mu_{\text{Li}} = -2.00 \text{ eV}, \Delta\mu_{\text{Cl}} = -2.19 \text{ eV}, \Delta\mu_{\text{O}} = -1.32 \text{ eV}\}$ (Li-rich) and $\{\Delta\mu_{\text{Li}} = -2.23 \text{ eV}, \Delta\mu_{\text{Cl}} = -1.75 \text{ eV}, \Delta\mu_{\text{O}} = -1.08 \text{ eV}\}$ (Li-poor).

5.4 Intrinsic defect chemistry of undoped Li₃OCl

We first consider the formation energies and equilibrium concentrations of native defects in undoped, nominally stoichiometric, Li₃OCl. Figure 5.4 shows formation energies of native defects in Li₃OCl as a function of Fermi energy (transition level diagrams), under Li-poor and Li-rich conditions (upper panels), and the corresponding equilibrium defect concentrations (lower panels). Under Li-poor conditions, the dominant defect species are lithium vacancies, V_{Li} , and chlorine vacancies, V_{Cl} , which is qualitatively consistent with previous predictions of Li₃OCl as being predominantly $V_{\text{Li}} + V_{\text{Cl}}$ Schottky-disordered [21, 23, 24]. The dominant $V_{\text{Li}} + V_{\text{Cl}}$ Schottky disorder can also be assigned directly from the defect formation energies plot (fig. 5.4(a)), which shows the equilibrium Fermi energy is pinned by the $V_{\text{Li}}' - V_{\text{Cl}}^\bullet$ defect pair. Under Li-rich conditions, chlorine vacancies, V_{Cl}^\bullet , are the dominant positively charged defect species. The dominant negatively charged defect, however, is the oxygen-

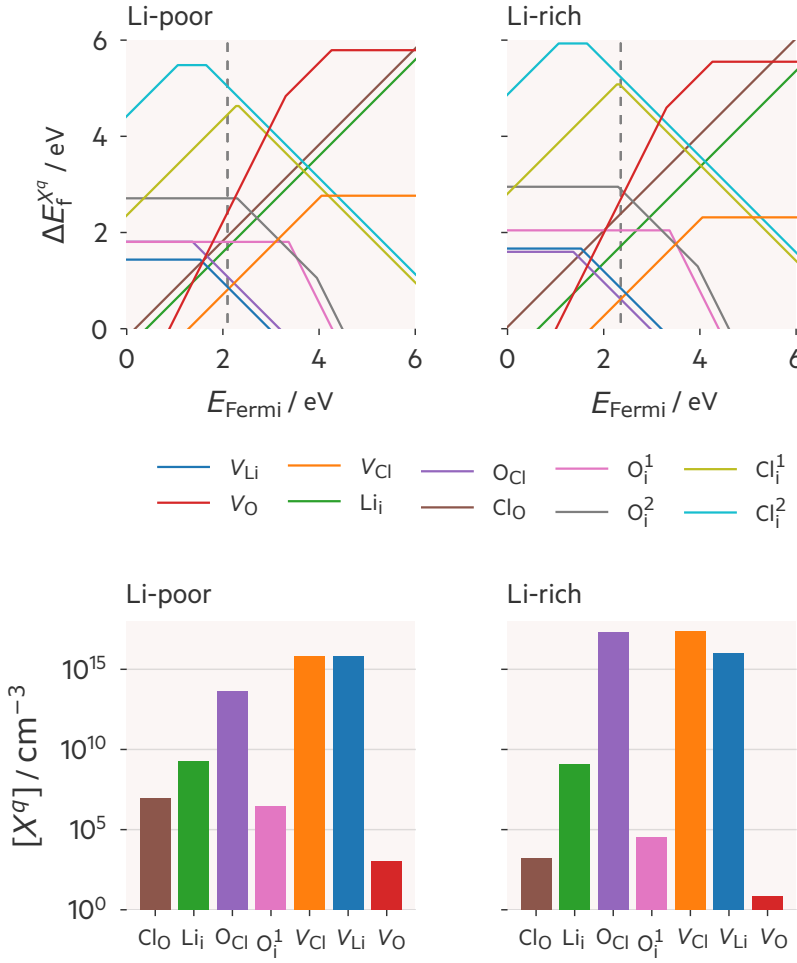
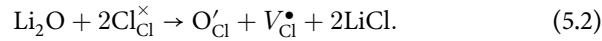


Figure 5.4: Transition level diagrams (**top row**) and defect concentrations (**bottom row**) for defects in Li_3OCl under Li-poor (**left column**) and Li-rich (**right column**) synthesis conditions (see fig. 5.3), at 360 °C. The dashed line marked on the transition level diagrams is the position of the self-consistently determined Fermi energy; defect charge states are given by the gradient. For the defect concentration plots we show only those defect species with concentrations $[X] > 1 \times 10^2 \text{ cm}^{-3}$ under Li-rich or Li-poor conditions. Defect species with concentrations $[X] < 1 \times 10^2 \text{ cm}^{-3}$ under all conditions are not shown in the bottom plots.

chlorine antisite, O'_{Cl} . From a charge- and mass-balanced defect reaction perspective the system is no longer best characterised by $V_{\text{Li}} + V_{\text{Cl}}$ Schottky disorder, and the lowest energy defect-formation reaction is



This different classification can again be assigned from the plot of Fermi-energy dependent defect formation energies, where the Fermi energy is now pinned by the $\text{O}'_{\text{Cl}} - V_{\text{Cl}}^{\bullet}$ defect pair (fig. 5.4, right hand column).

The presence of anion disorder in Li_3OCl in the form of O'_{Cl} antisites, particularly under Li-rich conditions, has potential implications for lithium transport. $\text{O}'_{\text{Cl}} + \text{Cl}_{\text{O}}^{\bullet}$ antisite pairs have been predicted via *ab initio* molecular dynamics to enhance lithium diffusion relative to a perfectly anion-ordered reference system [20]. Anion framework disorder has also been associated with increased ionic conductivity in other antiperovskites [42, 43] and in other lithium-ion solid electrolytes [18, 44, 45]. Synthesis protocols that increase the degree of host-framework-disorder in Li_3OCl , or in other antiperovskites, may therefore provide alternative routes to improving the ionic conductivities of these materials beyond purely modi-

ifying lithium stoichiometry.

Although symmetric O/Cl disorder has been predicted to give increased lithium transport [20], our calculations predict that O–Cl antisites in Li_3OCl do not form in stoichiometry-preserving $\text{Cl}_\text{O}^\bullet + \text{O}'_\text{Cl}$ pairs, but instead there is a large excess of O'_Cl antisites. Previous *ab initio* molecular dynamics simulations have predicted that isolated O'_Cl defects electrostatically trap lithium interstitials, thereby suppressing lithium diffusion [9, 24]. In undoped Li_3OCl , however, lithium vacancies are the dominant charge-carrying lithium defect species under all conditions, with lithium interstitial concentrations several orders of magnitude lower. Any trapping of lithium interstitials by O'_Cl is therefore expected to have a negligible effect on the net ionic conductivity of undoped Li_3OCl .

5.5 Supervalent and subvalent doping response in Li_3OCl

We now consider how the intrinsic native defect concentrations in Li_3OCl respond to aliovalent doping. Figure 5.5 shows, again, the Fermi-energy dependent defect formation energies and equilibrium defect concentrations in as-synthesised Li_3OCl , but now compares these “stoichiometric” defect concentrations with those predicted for an effective supervalent dopant concentration of $r[M^r] = 10^{18} \text{ cm}^{-3}$. Supervalent doping under Li-poor conditions principally increases the concentration of lithium vacancies, which are the lowest formation energy negatively-charged defect species in the parent undoped material—the system therefore behaves qualitatively as predicted by simple lithium-defect charge-compensation models. Supervalent doping under Li-rich conditions principally increases the concentration of the O'_Cl antisite, which is now the lowest formation energy negatively-charged defect species. Under Li-rich conditions, therefore, supervalent doping produces a smaller increase in lithium vacancy concentration than predicted by simple models that assume direct charge-compensation by lithium defects.

The equivalent analysis for the case of subvalent doping is also shown in fig. 5.5. Under both Li-rich and Li-poor synthesis conditions, subvalent doping gives only a modest increase in the concentration of lithium interstitials, and the principal effect is instead to increase $[\text{V}'_\text{Cl}]$. We also observe a significant decrease in the lithium vacancy concentration. Although lithium interstitials are expected to be more mobile than lithium vacancies, this analysis suggests the potential for a regime where subvalent doping causes a net *decrease* in ionic conductivity due to the decrease in the dominant charge-carrying lithium-defect species, i.e., lithium vacancies. We return to this point in more detail in section 5.6 where we quantify how ionic conductivities are predicted to vary as a function of

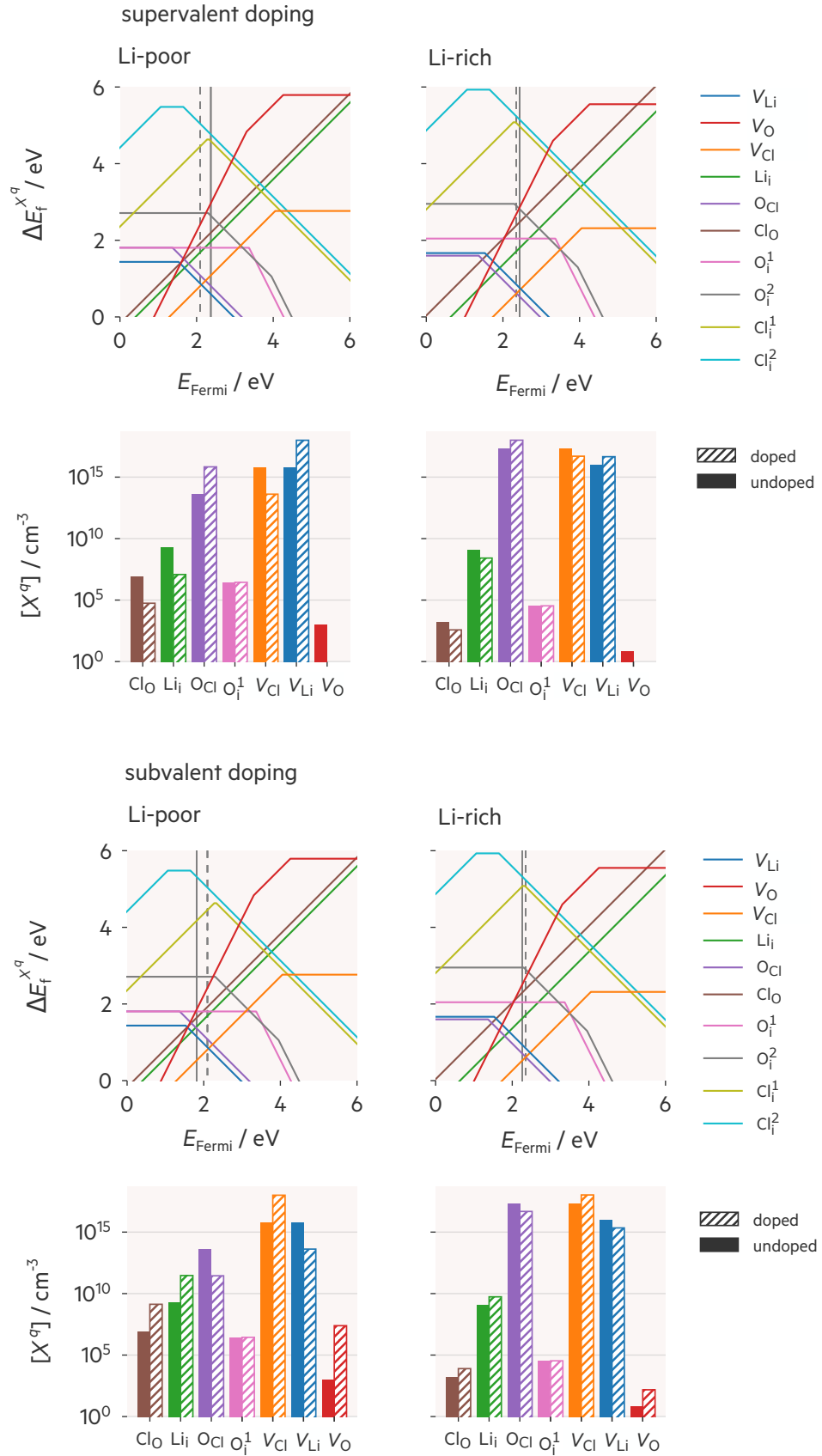


Figure 5.5: **Top four panels** transition level diagrams (**top row**) and defect concentrations (**bottom row**) for defects in undoped and supervalent doped Li_3OCl under lithium poor (**left column**) and lithium rich (**right column**) conditions (see fig. 5.3), at 360°C . In the upper panels, the vertical dashed line shows the equilibrium Fermi energy in the undoped system, and the vertical solid line shows the equilibrium Fermi energy when doping at an effective dopant concentration of $r[M^r] = 10^{18} \text{ cm}^{-3}$. Defect species with concentrations $[X] < 1 \times 10^2 \text{ cm}^{-3}$ under all conditions are not shown in the bottom plots. The **bottom four panels**, show the same again, but for subvalent doping (i.e. $r[M^r] = -10^{18} \text{ cm}^{-3}$).

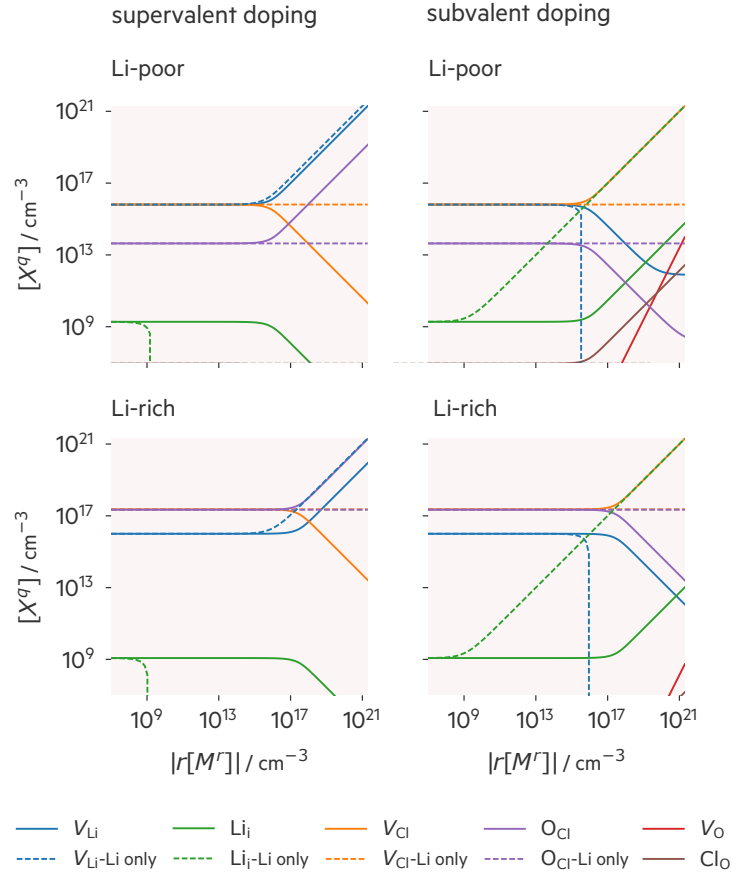
supervalent or subvalent dopant concentrations.

To illustrate the difference in predicted behaviour between a mobile-point defect charge-compensation model and our self-consistent model, we consider the doping response of Li_3OCl as a function of effective dopant concentration, $r[M^r]$, for both a simple “lithium-only” charge compensation model, where only charge-carrying lithium defects change concentration in response to doping, and for our full model, where all defects re-equilibrate. Figure 5.6 shows the predicted doping response for these two models, for supervalent doping and subvalent doping at a range of dopant concentrations, under Li-rich and Li-poor synthesis conditions. Here, we have considered a maximum dopant concentration equivalent to $\sim 4\%$ of lithium sites, which is a similar dopant/defect concentration to that used in previous *ab initio* molecular dynamics studies of doping in Li_3OCl [9, 20]. Because our model assumes that defects behave ideally our results are expected to be quantitatively accurate only at low dopant and defect concentrations. At high dopant or high defect concentrations, non-ideal defect–defect interactions may make a significant contribution to defect chemical potentials, causing defect concentrations to deviate from the dilute-limit behaviour modelled here [46, 47]. We expect, however, that general trends regarding the relative response of different defects to doping will be qualitatively correct even at these high dopant concentrations.

The only case where the simple “lithium-only” defect model gives approximate quantitative agreement with the full model, with respect to the change in concentrations of charge-carrying lithium defect species, is for supervalent doping under Li-poor synthesis conditions (fig. 5.6). In this case, the lowest formation energy negatively-charged defect species in the undoped system is the lithium vacancy, which therefore shows the strongest enhancement in concentration under supervalent doping. Under Li-poor conditions, the dominant negatively-charged defect species in the undoped system is the oxygen–chlorine O'_{Cl} antisite, which is now preferentially enhanced by supervalent doping. This suppresses the increase in lithium vacancy concentration relative to that predicted by the simple “lithium-only” model.

Under subvalent doping, the two models give even more strongly divergent predictions; the lithium-only defect model underestimates the doping threshold at which a significant increase in concentration of lithium interstitials is observed by several orders of magnitude. This effect can be understood by considering the conventional “Schottky pair” description of defect chemistry in Li_3OCl ; the dominant positively charged defect species is the chlorine vacancy, V_{Cl}^\bullet , and subvalent doping therefore principally increases the concentration of this non-charge-carrying

Figure 5.6: Defect concentrations as a function of effective dopant concentration ($r[M^r]$) shown for both supervalent dopants (**left column**), and subvalent dopant (**right column**), for Li-poor (**top row**) and Li-rich (**bottom row**) synthesis conditions, at 360 °C. The solid lines show defect concentrations when all defect concentrations are allowed to vary as the dopant concentration is increased, the dotted lines show the case when only the concentration of lithium defects are allowed to change.



host-framework defect ahead of the minority Li_i^\bullet defects.

5.6 Defect mediated ionic conductivity in Li_3OCl

We next consider how the variation in native defect concentrations under different synthesis conditions, and the associated varying response to supervalent and subvalent doping, affects the ionic conductivity of doped Li_3OCl . We assume lithium diffusion is effected by dilute populations of lithium vacancies and lithium interstitials, which allows us to neglect correlation effects and also allows us to express the total ionic conductivity as a sum over contributions from lithium vacancies and lithium interstitials respectively:

$$\sigma = \frac{[V_{\text{Li}}]}{k_{\text{B}}T} D_{V_{\text{Li}}}^* + \frac{[\text{Li}_i]}{k_{\text{B}}T} D_{\text{Li}_i}^*, \quad (5.3)$$

The self-diffusion coefficients for each defect species are estimated from the dilute limit expression for independent defect hopping

$$D_X^* = \frac{1}{6} \nu_0 a^2 \exp\left(\frac{-\Delta E_X}{k_{\text{B}}T}\right), \quad (5.4)$$

where ν_0 is the attempt frequency, which we set as a characteristic value of 1×10^{13} Hz for both lithium vacancies and lithium interstitials, and a is

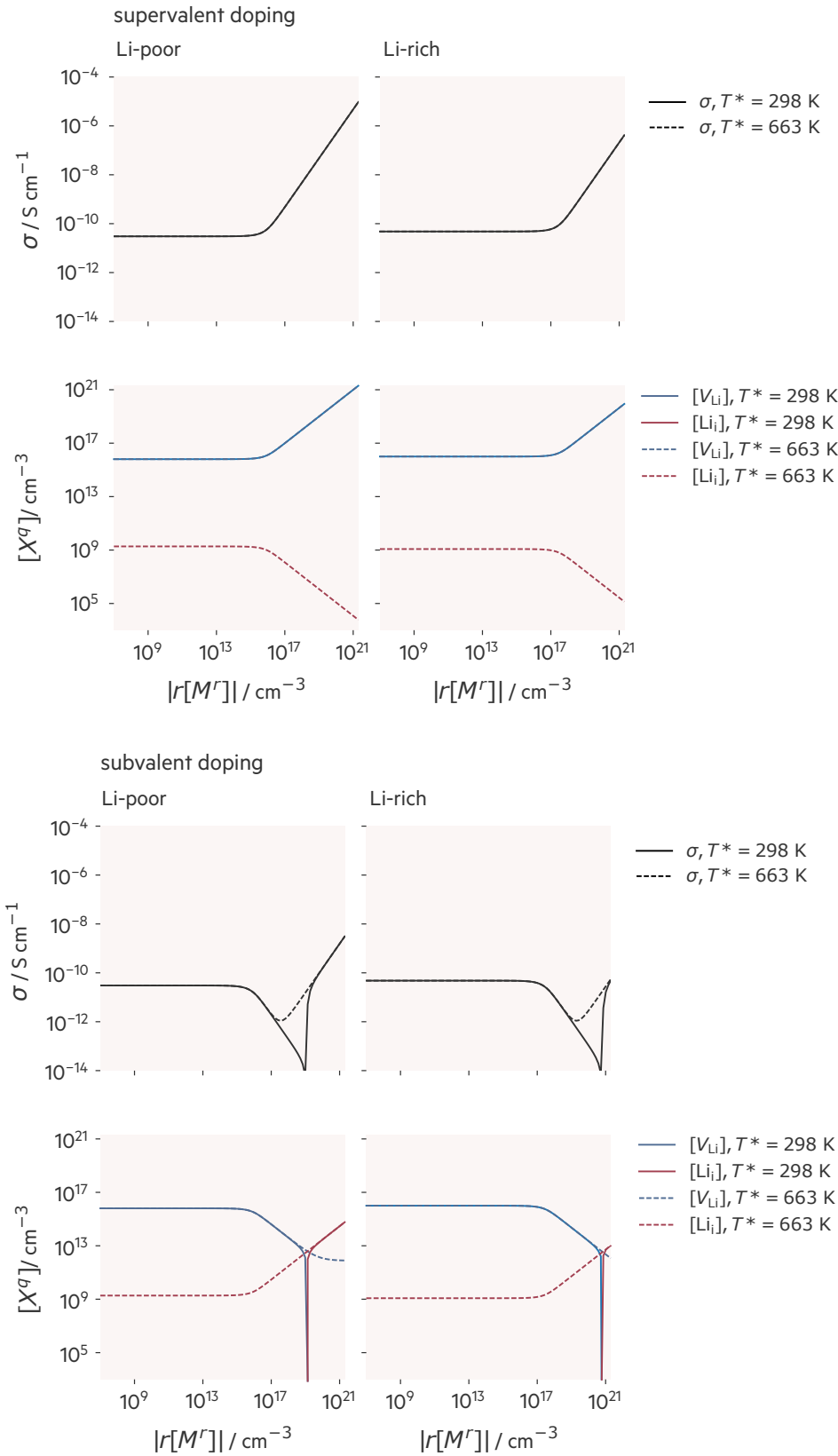


Figure 5.7: The **top four panels** show, under supervalent doping, ionic conductivities (**top row**) and lithium interstitial and lithium vacancy concentrations (**bottom row**) as a function of effective doping concentration $r[M^r]$ for Li-rich and Li-poor synthesis conditions and for supervalent and subvalent doping. Dashed lines show equilibrium data calculated for synthesis conditions at 663 K. Solid lines show pseudo-equilibrium data calculated at 298 K allowing lithium interstitials and lithium vacancies to re-equilibrate under fixed total lithium content, while other defects are “frozen in” at their synthesis concentrations. The **bottom four panels** show the same under subvalent doping.

the hop distance [48] which we take as nearest-neighbour Li–Li distance of 2.67 Å. ΔE_X is the potential energy barrier for defect species X to hop between adjacent defect sites, for which we use the barrier heights calculated by Emly *et al.* of $\Delta E_{\text{Li}_i} = 0.17$ eV, $\Delta E_{V_{\text{Li}}} = 0.34$ eV [21], which gives a ratio $D_{\text{Li}_i}^*/D_{V_{\text{Li}}}^* \approx 10^3$ at $T = 298$ K.

To calculate the ionic conductivity of Li_3OCl using eq. (5.3) we require the lithium vacancy and lithium interstitial concentrations under typical operating conditions. Crucially, these defect concentrations can differ from the values predicted under typical synthesis conditions (300–360 °C under vacuum) that we have presented in sections 5.4 and 5.5. Both lithium vacancies and lithium interstitials are highly mobile even at room temperature, and some proportion of lithium vacancy–interstitial pairs will recombine as the temperature is decreased. Electron and hole pairs may also recombine upon cooling, although in a wide-gap system such as Li_3OCl , this is expected to have a negligible effect on the Fermi level position and therefore on defect populations.

To model the change in lithium defect concentration upon cooling from synthesis temperatures to room temperatures, we perform a two-stage calculation. We first calculate equilibrium concentrations for all defect species at a typical synthesis temperature of 360 °C. We then fix the concentrations of all anionic defect species, which are considered to be “frozen in” during cooling [37, 49], and recalculate the lithium vacancy and interstitial concentrations and electron and hole concentrations a pseudo-equilibrium temperature $T^* = 298$ K.

Figure 5.7 shows calculated lithium vacancy and lithium interstitial concentrations and corresponding ionic conductivities (via eq. (5.3)) for Li_3OCl synthesised under Li-poor and Li-rich conditions, as a function of supervalent and subvalent effective dopant concentrations. To illustrate the effect of cooling from synthesis conditions to room temperature on lithium defect concentrations and on the ionic conductivity, we show data calculated for full equilibration under synthesis conditions ($T = 663$ K; dashed lines) and for partial re-equilibration at room temperature ($T^* = 273$ K; solid lines).

For undoped Li_3OCl we predict ionic conductivities of 4.2×10^{-10} S cm $^{-1}$ under Li-poor synthesis conditions and 6.7×10^{-10} S cm $^{-1}$ under Li-rich synthesis conditions. In both cases the contribution to the ionic conductivity from lithium interstitials is negligible ($\sim 10^{-14}$ S cm $^{-1}$). Our calculated ionic conductivities ($\sim 5 \times 10^{-10}$ S cm $^{-1}$) are much lower than those previously reported for experimental samples of nominally stoichiometric Li_3OCl (10^{-3} – 10^{-6} S cm $^{-1}$) [13, 50]. One possible reason for this discrepancy is that previous experimental data might not have been obtained for phase-pure “stoichiometric” Li_3OCl . Li_3OCl is extremely challenging

to synthesise, as indicated by the small calculated region of metastability under typical synthesis conditions (fig. 5.3), and it has been suggested that samples reported in the literature as Li_3OCl may in fact be competing hydrated phases, such as Li_2OHCl [1, 5], which are predicted to have higher total conductivities than pristine Li_3OCl [51].

Considering the effect of aliovalent doping on ionic conductivity, supervalent doping produces a monotonic increase in the concentration of lithium vacancies, and therefore also produces a monotonic increase in ionic conductivity. The quantitative effect of supervalent doping on ionic conductivity depends on synthesis conditions. Under Li-poor conditions, where lithium vacancies are the highest concentration native defect species, the ionic conductivity behaves almost entirely as predicted by assuming direct charge-compensating formation of lithium vacancies. Under Li-rich conditions, however, where the dominant negatively charged native defect species is the oxygen-chlorine antisite O'_{Cl} , this non-charge-carrying defect species is preferentially formed. The positive effect of supervalent doping on ionic conductivity is therefore suppressed, and higher effective dopant concentrations are needed for a given increase in ionic conductivity than predicted by a simple lithium-defect charge-compensation model.

In contrast to the monotonic increase in ionic conductivity produced by supervalent doping, subvalent doping causes the ionic conductivity to *decrease* at moderate effective dopant concentrations under all synthesis conditions. High dopant concentrations are needed to achieve a net increase in ionic conductivity relative to undoped Li_3OCl through subvalent doping. This behaviour is a consequence of two factors. First, although subvalent doping increases the concentrations of all positively-charged defect species, it also decreases the concentrations of all negatively-charged defect species, including lithium vacancies. Because, in the undoped systems, the concentration of lithium vacancies is significantly higher than that of lithium interstitials, low-to-moderate levels of subvalent doping decrease the concentration of lithium vacancies by a much greater extent than they increase the concentration of lithium interstitials. In as-synthesised Li_3OCl , this effect gives a minimum in ionic conductivity when $[V_{\text{Li}}] D_{V_{\text{Li}}}^* = [Li_{\text{i}}] D_{Li_{\text{i}}}^*$ [52].

The second cause of a reduced room-temperature ionic conductivity under subvalent doping is recombination of $V'_{\text{Li}} + Li_{\text{i}}^\bullet$ Frenkel pairs when the system is cooled. The Frenkel pair formation energy in Li_3OCl is high (our calculated value is 2.6 eV), which indicates a strong enthalpic driving force for lithium vacancy-interstitial pairs to recombine. Because lithium vacancies and lithium interstitials recombine in a 1:1 ratio, this Frenkel-pair recombination is limited by the concentration of the minority lithium

defect species. In undoped Li_3OCl , the concentration of lithium interstitials is low and lithium vacancies are present in large excess. Frenkel-pair recombination therefore has a negligible effect on the lithium vacancy concentration and a corresponding negligible effect on the net ionic conductivity. Subvalent doping, however, under all synthesis conditions, increases the concentration of lithium interstitials and decreases the concentration of lithium vacancies. As the concentrations of these two defects become more equal, an increasing proportion of lithium vacancies are removed through Frenkel-pair recombination, and the ionic conductivity is progressively reduced. This effect is strongest when the concentrations of lithium vacancies and lithium interstitials are equal; nearly all the lithium vacancies and interstitials recombine, greatly reducing the concentrations of these charge carrying defects, and giving a sharp decrease in ionic conductivity. For effective dopant concentrations above this threshold, the concentration of lithium interstitials under synthesis conditions now exceeds that of lithium vacancies, and the room temperature lithium interstitial concentration and ionic conductivity both increase with effective dopant concentration.

The different ionic conductivity responses to supervalent versus subvalent doping, under lithium-rich and lithium-poor conditions, are compared graphically in fig. 5.8. As noted above, subvalent doping is predicted to give no net increase in ionic conductivity except at very high dopant levels. Even at sufficient subvalent doping levels to produce a net increase in ionic conductivity, the resulting conductivity increase remains orders of magnitude smaller than for supervalent doping at comparable dopant concentrations, and we conclude, therefore, that subvalent doping to increase lithium interstitial concentrations is not an effective strategy for enhancing the ionic conductivity of Li_3OCl . Our analysis also indicates that subvalent doping will be maximally effective under Li-poor synthesis conditions, due to the associated low formation energy of V_{Li}' .

5.7 Summary and Discussion

To characterise the native defect chemistry of Li_3OCl , and to quantify the effect of supervalent and subvalent doping on native defect concentrations and on ionic conductivity, we have performed a hybrid density-functional-theory study of the defect chemistry and aliovalent-doping response of Li_3OCl that considers all native vacancy, interstitial, and anion antisite defect species within a self-consistent thermodynamic model. In undoped Li_3OCl , under Li-poor conditions, the dominant negatively charged defect species is V_{Li}' and the dominant positively charged defect species is V_{Cl}^\bullet , which is qualitatively consistent with previous descriptions of Li_3OCl

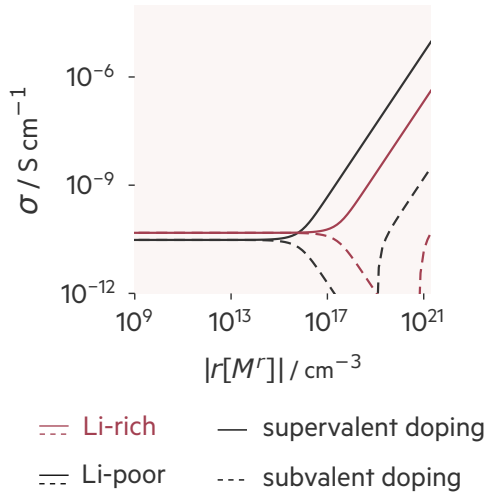


Figure 5.8: Predicted room-temperature ionic conductivity of Li_3OCl under Li-rich and Li-poor synthesis conditions as a function of supervalent or subvalent effective dopant concentration, $r[M^r]$.

as being $[V_{\text{Li}} + V_{\text{Cl}}]$ Schottky-disordered [3, 21, 30, 53]. Under Li-rich conditions, the dominant defect species are O'_{Cl} and V_{Cl}^\bullet . The change in highest concentration negatively-charged defect from V_{Li} to O'_{Cl} illustrates the potential limitations of considering the defect chemistry of solid electrolytes only in terms of simple Schottky or Frenkel-pair defect formation reactions.

Supervalent doping is predicted to most strongly increase the concentrations of both V_{Li} and O'_{Cl} . The defect species with the higher concentration in the relevant undoped system undergoes the largest increase, and supervalent doping is therefore predicted to most effectively increase the concentration of lithium vacancies under Li-poor synthesis conditions. Subvalent doping principally increases the concentration of chlorine vacancies ahead of lithium interstitials under all considered synthesis conditions, due to the much higher concentration of chlorine vacancies with respect to lithium interstitials in undoped Li_3OCl .

The quantitatively different response of these competing defect species to supervalent or subvalent doping can be characterised in terms of a “doping-response efficiency”, η_X , which we define as the change in concentration of a defect species, $\Delta[X]$, for a fixed effective dopant concentration, $r[M^r]$, divided by the change in concentration if the doping response were purely due to defect X in charge state q' , i.e.,

$$\eta_X = -\frac{q' \Delta[X]}{r[M^r]}. \quad (5.5)$$

This gives a measure of how many additional defects of defect species X are introduced or removed per dopant. Figure 5.9 shows calculated values of η_X for V_{Li} and O_{Cl} with $q' = -1$ and for V_{Cl} and Li_i^\bullet with $q' = +1$ for an effective dopant concentration of $r[M^r] = \pm 10^{18} \text{ cm}^{-3}$ for both supervalent and subvalent doping. The calculated values of $\eta_{V_{\text{Li}}}$ and $\eta_{\text{Li}_i^\bullet}$ reflect

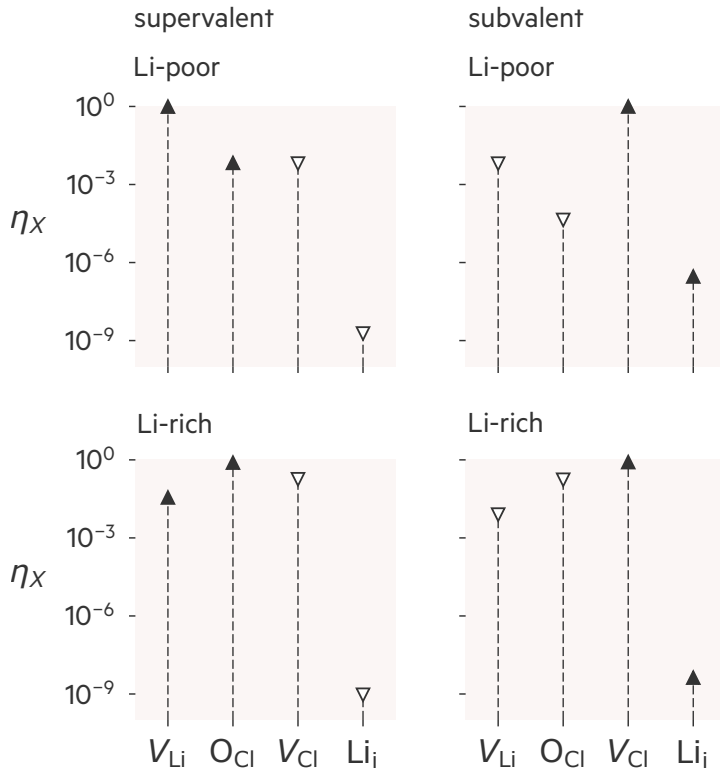


Figure 5.9: Doping-response efficiency, η_X , (eq. (5.5)) for V_{Li} , O_{Cl} , V_{Cl} and Li_i under lithium poor conditions (top row) and lithium rich conditions (bottom row) for supervalent doping (left hand column) and subvalent doping (right hand column) at an effective dopant concentration $r[M^r] = \pm 10^{18} \text{ cm}^{-3}$. \uparrow indicates defect concentrations that increase upon doping, and \downarrow indicates defect concentrations that decrease upon doping.

the strong asymmetry in the doping response of the lithium vacancy and interstitial. Supervalent doping under lithium-poor conditions strongly increases the concentration of lithium vacancies, indicated by $\eta_{V_{\text{Li}}} \approx 1$. For supervalent doping under lithium-rich conditions, $\eta_{V_{\text{Li}}}$ remains high, but is now smaller than $\eta_{O_{\text{Cl}}}$, reflecting the preferential formation of O_{Cl} antisites. For subvalent doping, $\eta_{\text{Li}_i} < 10^{-8}$ under all conditions; at these dopant concentrations, subvalent doping has a negligible effect on the concentration of lithium interstitials and instead principally increases the concentration of Cl vacancies ($\eta_{V_{\text{Cl}}} \approx 1$). In the case of Li_3OCl , then, the doping-response efficiency, η_X , provides an intuitive description of the strongly asymmetric response to supervalent versus subvalent doping.

One practical consequence of the asymmetric doping response of Li_3OCl is the qualitatively different response of the ionic conductivity under supervalent versus subvalent doping. Supervalent doping produces a monotonic increase in lithium vacancy concentration, and a corresponding monotonic increase in ionic conductivity. Subvalent doping, in contrast, produces a *decrease* in ionic conductivity at low-to-moderate dopant levels due to two complementary effects. First, at low-to-moderate subvalent doping levels the primary effect of subvalent doping is to decrease the concentration of lithium vacancies, rather than increase the concentration of lithium interstitials (Figure 5.9). Second, by increasing the number of lithium interstitials formed under synthesis conditions, a greater number

of lithium vacancies are removed when cooling to room temperature due to recombination of V_{Li} as $V_{\text{Li}} + \text{Li}_i$ Frenkel pairs. For sufficiently high dopant levels, subvalent doping is predicted to give an increase in ionic conductivity relative to undoped Li_3OCl . This net positive contribution to the ionic conductivity, however, only occurs when the effective dopant concentration is much larger than the lithium vacancy concentration in the undoped material, $r [M^r] \gg [V_{\text{Li}}]_{\text{undoped}}$.

The strongly asymmetric doping response of Li_3OCl with respect to supervalent versus subvalent doping can be understood as a consequence of the low formation energy of positively charged V_{Cl} defects with respect to Li_i defects (fig. 5.4); equivalently, this effect can be considered to be a consequence of the dominant $V_{\text{Li}} + V_{\text{Cl}}$ Schottky disorder that characterises the lithium defect chemistry in this system. Under Li-poor conditions, the Fermi energy is pinned by the $V_{\text{Li}} + V_{\text{Cl}}$ pair; V_{Li} and V_{Cl} are present in approximately equal concentrations, and Li_i concentrations are several orders of magnitude lower, corresponding to a classical Schottky-disordered system. Under Li-rich conditions, the Fermi energy is pinned by the $\text{O}_{\text{Cl}} + V_{\text{Cl}}$ pair and the dominant defect species are O_{Cl} and V_{Cl} rather than lithium disorder. Under these conditions, however, the concentration of V_{Li} is still several orders of magnitude larger than the concentration of Li_i , and the lithium defect chemistry can still be considered within the schema of $V_{\text{Li}} + V_{\text{Cl}}$ Schottky disorder.

Because the response of a specific defect species to aliovalent doping scales with the concentration of that defect species in the undoped system, Schottky disorder implies a much higher doping-response efficiency, η_X , for V_{Li} than for Li_i —which is indeed the case for Li_3OCl (cf. fig. 5.9). This leads to $[V_{\text{Li}}]$ decreasing much more rapidly than $[\text{Li}_i]$ increases under subvalent doping. Schottky disorder also indicates a relatively high $V_{\text{Li}} + \text{Li}_i$ Frenkel pair formation energy, which means a strong enthalpic driving force for Frenkel-pair recombination when cooling from synthesis temperatures to room temperature. Both of the effects that cause ionic conductivity to decrease or only moderately increase in response to subvalent doping are therefore consequences of Li_3OCl being a “Schottky-disordered” solid electrolyte. By extension, we therefore expect other principally Schottky-disordered solid electrolytes, including other antiperovskite solid electrolytes [2–7], to have analogous asymmetric doping responses.

One of the limitations of the study presented here is that we consider dopants as ideal, i.e. they affect the defect chemistry of Li_3OCl only through their effect on the the Fermi energy. In reality, direct dopant–defect interactions may be significant [8, 9, 54, 55]. For example, supervalent dopants, such as Mg^{2+} , are predicted to kinetically trap lithium

vacancies [8], which will reduce ionic conductivities relative to the values presented in this work. Despite this limitation, we expect our results to accurately describe quantitative trends for different synthesis conditions and doping strategies for Li_3OCl .

This study also illustrates how the defect chemistry and doping response of solid electrolytes may be more complex than implied by simple mass- and charge-compensating defect formation schemes, and demonstrates how a more complete description that accounts for varying synthesis conditions and thermodynamic competition between defect species can be found by considering a full set of defects within a self-consistent thermodynamic model.

Bibliography

- (1) Hanghofer, I.; Redhammer, G. J.; Rohde, S.; Hanzu, I.; Senyshyn, A.; Wilkening, H. M. R.; Rettenwander, D. *Chem. Mater.* **2018**, *30*, 8134–8144.
- (2) Wang, Z.; Xu, H.; Xuan, M.; Shao, G. *J. Mater. Chem. A* **2018**, *6*, 73–83.
- (3) Dawson, J. A.; Chen, H.; Islam, M. S. *J. Phys. Chem. C* **2018**, *122*, 23978–23984.
- (4) Wan, T. H.; Lu, Z.; Ciucci, F. *J. Power Sources* **2018**, *390*, 61–70.
- (5) Dawson, J. A.; Famprakis, T.; Johnston, K. E. *J. Mater. Chem. A* **2021**, *9*, 18746–18772.
- (6) Fujii, S.; Gao, S.; Tassel, C.; Zhu, T.; Broux, T.; Okada, K.; Miyahara, Y.; Kuwabara, A.; Kageyama, H. *J. Am. Chem. Soc.* **2021**, *143*, 10668–10675.
- (7) Gao, S.; Broux, T.; Fujii, S.; Tassel, C.; Yamamoto, K.; Xiao, Y.; Oikawa, I.; Takamura, H.; Ubukata, H.; Watanabe, Y.; Fujii, K.; Yashima, M.; Kuwabara, A.; Uchimoto, Y.; Kageyama, H. *Nat. Commun.* **2021**, *12*, 201.
- (8) Clarke, M. J.; Dawson, J. A.; Mays, T. J.; Islam, M. S. *ACS Appl. Energy Mater.* **2021**, *4*, 5094–5100.
- (9) Li, P.; Hussain, F.; Cui, P.; Li, Z.; Yang, J. *Phys. Rev. Mater.* **2019**, *3*, 115402.
- (10) Braga, M. H.; Stockhausen, V.; Oliveira, J. C.; Ferreira, J. A. *MRS Proc.* **2013**, *1526*, 905.
- (11) Li, Y.; Zhou, W.; Xin, S.; Li, S.; Zhu, J.; Lü, X.; Cui, Z.; Jia, Q.; Zhou, J.; Zhao, Y.; Goodenough, J. B. *Angew. Chem. Int. Edit.* **2016**, *55*, 9965–9968.

- (12) Stegmaier, S.; Voss, J.; Reuter, K.; Luntz, A. C. *Chem. Mater.* **2017**, *29*, 4330–4340.
- (13) Zhao, Y.; Daemen, L. L. *J. Am. Chem. Soc.* **2012**, *134*, 15042–15047.
- (14) Burbano, M.; Carlier, D.; Boucher, F.; Morgan, B. J.; Salanne, M. *Phys. Rev. Lett.* **2016**, *116*, 135901–6.
- (15) Kozinsky, B.; Akhade, S. A.; Hirel, P.; Hashibon, A.; Elsässer, C.; Mehta, P.; Logéat, A.; Eisele, U. *Phys. Rev. Lett.* **2016**, *116*, 055901–5.
- (16) Ohno, S.; Banik, A.; Dewald, G. F.; Kraft, M. A.; Krauskopf, T.; Minafra, N.; Till, P.; Weiss, M.; Zeier, W. G. *Prog. Energy* **2020**, *2*, 022001–36.
- (17) Kozinsky, B. In *Handbook of Materials Modeling*; Springer International Publishing: 2018, pp 1–20.
- (18) Morgan, B. J. *Chem. Mater.* **2021**, *33*, 2004–2018.
- (19) Zhou, L.; Minafra, N.; Zeier, W. G.; Nazar, L. F. *Acc. Chem. Res.* **2021**, *54*, 2717–2728.
- (20) Zhang, Y.; Zhao, Y.; Chen, C. *Phys. Rev. B* **2013**, *87*, DOI: 10.1103/physrevb.87.134303.
- (21) Emly, A.; Kioupakis, E.; Van der Ven, A. *Chem. Mater.* **2013**, *25*, 4663–4670.
- (22) Deng, Z.; Radhakrishnan, B.; Ong, S. P. *Chem. Mater.* **2015**, *27*, 3749–3755.
- (23) Mouta, R.; Melo, M. Á. B.; Diniz, E. M.; Paschoal, C. W. A. *Chem. Mater.* **2014**, *26*, 7137–7144.
- (24) Lu, Z.; Chen, C.; Baiyee, Z. M.; Chen, X.; Niu, C.; Ciucci, F. *Phys. Chem. Chem. Phys.* **2015**, *17*, 32547–32555.
- (25) Braga, M. H.; Ferreira, J. A.; Stockhausen, V.; Oliveira, J. E.; El-Azab, A. *J. Mater. Chem. A* **2014**, *2*, 5470–5480.
- (26) Braga, M. H.; Grundish, N. S.; Murchison, A. J.; Goodenough, J. B. *Energy Environ. Sci.* **2017**, *10*, 331–336.
- (27) Zhang, S. B.; Northrup, J. E. *Phys. Rev. Lett.* **1991**, *67*, 2339–2342.
- (28) Buckeridge, J. *Comp. Phys. Commun.* **2019**, *244*, 329–342.
- (29) Wu, M.; Xu, B.; Lei, X.; Huang, K.; Ouyang, C. *J. Mater. Chem. A* **2018**, *6*, 1150–1160.
- (30) Baktash, A.; Demir, B.; Yuan, Q.; Searles, D. J. *Energy Stor. Mater.* **2021**, *41*, 614–622.
- (31) Kresse, G.; Furthmüller, J. *Phys. Rev. B.* **1996**, *54*, 11169–11186.

- (32) Kresse, G.; Furthmüller, J. *Comput. Mater. Sci.* **1996**, *6*, 15–50.
- (33) Krukau, A. V.; Vydrov, O. A.; Izmaylov, A. F.; Scuseria, G. E. *J. Chem. Phys.* **2006**, *125*.
- (34) Blöchl, P. E. *Phys. Rev. B* **1994**, *50*, 17953–17979.
- (35) Murnaghan, F. D. *Proc. Natl. Acad. Sci.* **1944**, *30*, 244–247.
- (36) Chen, M.-H.; Emly, A.; Van der Ven, A. *Phys. Rev. B* **2015**, *91*, 214306.
- (37) Serejo, J. A. S.; Pereira, J. S. S.; Mouta, R.; Rego, L. G. C. *Phys. Chem. Chem. Phys.* **2021**, *23*, 6964–6973.
- (38) Buckeridge, J.; Scanlon, D. O.; Walsh, A.; Catlow, C. R. *Comput. Phys. Comm.* **2014**, *185*, 330–338.
- (39) *CRC Handbook of Chemistry and Physics, 100th Edition*; CRC Press: 2019.
- (40) Finnis, M.; Lozovoi, A.; Alavi, A. *Annu. Rev. Mater. Res.* **2005**, *35*, 167–207.
- (41) Morgan, B. J.; Watson, G. W. *J. Phys. Chem. C* **2010**, *114*, 2321–2328.
- (42) Hull, S.; Keen, D. A.; Madden, P. A.; Wilson, M. *J. Phys.: Condens. Matter* **2007**, *19*, 406214.
- (43) Gombotz, M.; Hanghofer, I.; Eisbacher-Lubensky, S.; Wilkening, H. *Sol. Stat. Sci.* **2021**, *118*, 106680.
- (44) Gautam, A.; Sadowski, M.; Ghidui, M.; Minafra, N.; Senyshyn, A.; Albe, K.; Zeier, W. G. *Adv. Energy Mater.* **2020**, *11*, 2003369.
- (45) Sadowski, M.; Albe, K. *Philos. Trans. R. Soc. A* **2021**, *379*, 20190458.
- (46) Gray-Weale, A.; Madden, P. A. *J. Phys. Chem. B* **2004**, *108*, 6624–6633.
- (47) Gray-Weale, A.; Madden, P. A. *J. Phys. Chem. B* **2004**, *108*, 6634–6642.
- (48) Howard, R. E.; Lidiard, A. B. *Rep. Prog. Phys.* **1964**, *27*, 161–240.
- (49) Sasaki, K.; Maier, J. *J. Appl. Phys.* **1999**, *86*, 5422–5433.
- (50) Lü, X.; Wu, G.; Howard, J. W.; Chen, A.; Zhao, Y.; Daemen, L. L.; Jia, Q. *Chem. Commun.* **2014**, *50*, 11520–11522.
- (51) Dawson, J. A.; Attari, T. S.; Chen, H.; Emge, S. P.; Johnston, K. E.; Islam, M. S. *Energy Environ. Sci.* **2018**, *11*, 2993–3002.
- (52) Maier, J., *Physical Chemistry of Ionic Materials*; John Wiley & Sons, Ltd: 2004.

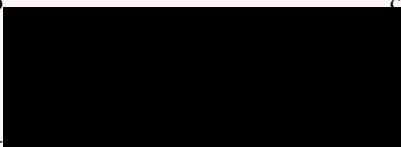
- (53) Zhang, Y.; He, X.; Chen, Z.; Bai, Q.; Nolan, A. M.; Roberts, C. A.; Banerjee, D.; Matsunaga, T.; Mo, Y.; Ling, C. *Nature Commun.* **2019**, *10*, 5260.
- (54) Mottet, M.; Marcolongo, A.; Laino, T.; Tavernelli, I. *Phys. Rev. Mater.* **2019**, *3*, 035403.
- (55) Culver, S. P.; Squires, A. G.; Minafra, N.; Armstrong, C. W. F.; Krauskopf, T.; Böcher, F.; Li, C.; Morgan, B. J.; Zeier, W. G. *J. Am. Chem. Soc.* **2020**, *142*, 21210–21219.

Statement of Authorship

The following chapter concerns the article entitled **Native Defects and Their Doping Response in the Lithium Solid Electrolyte $\text{Li}_7\text{La}_3\text{Zr}_2\text{O}_{12}$** published in Chemistry of Materials (*Chem. Mater.* 2020 32 (5), 1876-1886).

This paper reports on original research I conducted during the period of my Higher Degree by Research candidature.

Personal contributions: Formulation of ideas (70%): I have been heavily involved with all decisive stages of development of the project with guidance from Dr Benjamin Morgan on the motivation for the work. Design of methodology (70%): I designed the individual calculations and wrote bespoke post-processing code to analyse the results with input on best practice from Dr Benjamin Morgan and Prof. David Scanlon. Experimental work (100%): I carried out all practical aspects of the work. Presentation of data in journal format (80%): The first drafts of the manuscript were written by me, with input from Dr Benjamin Morgan and Prof. David Scanlon at each stage of revision. The finalised manuscript was prepared by Dr. Benjamin Morgan and me, with input from all co-authors.

Reproduced in part with permission from *Chem. Mater.* 2020 32 (5), 1876-1886. Co  ciety.

Signed: 

Date: 15 / 3 / 22

Context

Similarly to Chapter 5, this chapter discusses the defect chemistry and doping response of a lithium solid-electrolyte. In this instance we investigate the garnet-structured material LLZO. This study is not exactly analogous to the previous chapter for a number of reasons. First, we do not attempt to directly draw a relationship between ionic conductivity and defect concentration. While it is true that modulating the concentration of mobile ion point defects in LLZO will likely influence the ionic conductivity [1, 2], in the previous chapter we assumed defect-mediated ionic conductivity in which it is appropriate to approximate conductivity as a series of discrete hops of point defects. The lithium transport mechanism in LLZO is thought to be highly correlated, complicating the relationship between charge carrier concentration and ionic conductivity [3, 4]. Additionally, we do not model the response to subvalent doping. Most doping strategies used for LLZO-based solid electrolytes are supervalent, which is typically used to stabilise the high-conductivity cubic phase of LLZO [5].

One key point of note in both this chapter and the next, is that we study the defect chemistry of the tetragonal phase of LLZO. Tetragonal LLZO is crystallographically ordered whereas the higher conductivity cubic phase has a disordered arrangement of lithium ions. We do this because in an ordered system, we can capture the formation energies of all symmetrically equivalent defects from a single formation energy calculation. In a disordered material, defect formation energies should be computed as some kind of average over all accessible microstates, which rapidly becomes computationally intractable, especially when using a hybrid DFT functional to accurately capture the properties of defect states (see Section 3.5). Studying the defect chemistry of a disordered material using hybrid DFT represents a large overhead in both researcher and computational effort, as not only are the calculations much more resource intensive, but each defect calculation needs to be inspected to ensure, e.g., reasonable electron/hole localisation behaviour. We choose to characterise the defect chemistry of the ordered tetragonal phase of LLZO with hybrid-DFT which should accurately capture defect and electronic structure properties. We assume that this gives insight into the defect chemistry of cubic LLZO also, even if the results are only quantitatively accurate for the ordered material.

This chapter follows the same structure as the associated paper (see statement of authorship), however, it has been edited to remove information that is redundant within the context of this thesis and to better reflect the overall narrative of this dissertation.

6.1 Introduction

The lithium-stuffed garnets with the formula $\text{Li}_x\text{M}_3\text{M}'_2\text{O}_{12}$ (structure shown in Figure 6.1) are promising lithium solid electrolytes with ionic conductivities as high as $1 \times 10^{-3} \text{ S cm}^{-1}$ and good electrochemical stability [5, 6]. The garnet crystal structure has an unusual network of lithium diffusion pathways, consisting of interlocking rings. Each ring comprises alternating tetrahedral and octahedral lithium sites for a total of 12 sites, with the tetrahedral sites connecting adjacent rings [7]. These “ring-like” features are highlighted in Figure 6.2. The possible combinations of cations M and M' and potential different differing lithium content represents a large chemical space, with an equally large range of properties [8]. Identifying chemical compositions with optimal conductivities, however, remains a challenge, and requires an understanding of both lattice-cation substitution and lithium stoichiometry, and how these compositional parameters together affect lithium transport [2, 9–11].

Aliovalent doping is often used to optimise the ionic conductivity of lithium garnets. Supervalent doping of garnets has been particularly successful in $\text{Li}_7\text{La}_3\text{Zr}_2\text{O}_{12}$ (LLZO) following the realisation that inadvertent aluminium doping from synthesis apparatus produces a dramatic increase in room-temperature ionic conductivity by stabilising a high ionic conductivity cubic phase (typically unstable at temperatures below 600 K [12]) with respect to the poorly conducting tetragonal phase [3]. The transition from the tetragonal to cubic phase of LLZO is associated with a redistribution of the lithium sublattice within a single lithium “ring” (see Figure 6.2) and the onset of lithium disorder; the lithium sublattices in the cubic and tetragonal phases of LLZO are illustrated in Figure 6.3. This effect was explained by aluminium substituting for lithium, introducing a doubly positive net charge, which would be compensated by the formation of lithium vacancies [13],

$$[\text{Al}_{\text{Li}}^{\bullet\bullet}] = 2[V'_{\text{Li}}]. \quad (6.1)$$

Subsequent efforts to optimise the ionic conductivity of doped LLZO have seen a number of supervalent dopants proposed. These include other small cations, such as gallium, that directly substitute lithium [14]; larger cations, such as tantalum or niobium, that substitute zirconium or lanthanum on the M or M' sites [15]; and anions, such as fluorine, that substituted for oxygen [16]. All of these doping strategies can be classified as supervalent doping and target the same doping response: an increased lithium vacancy concentration.

Despite the attractive simplicity of this direct-charge-compensation model, it ignores other defect species that may form under specific synthesis conditions or in response to doping. A number of studies have

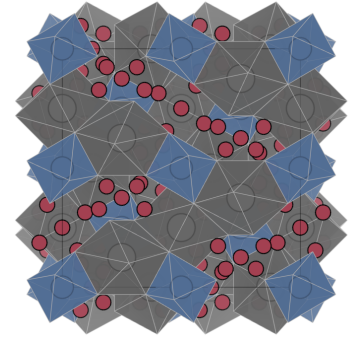


Figure 6.1: Structure of the lithium stuffed garnet $\text{Li}_x\text{M}_3\text{M}'_2\text{O}_{12}$ as shown down the b -axis. All lithium sites are shown in red (in realistic materials, some subset of these sites will be occupied), MO_8 polyhedra is shown in grey, and $\text{M}'\text{O}_6$ polyhedra are shown in blue.

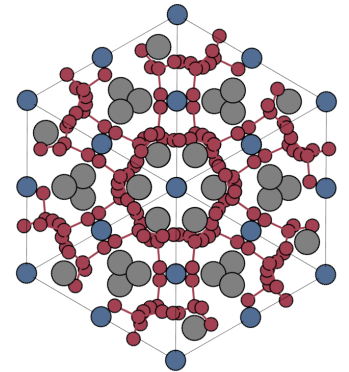


Figure 6.2: $\text{Li}_x\text{M}_3\text{M}'_2\text{O}_{12}$ as shown down the 111 crystal axis. All lithium sites are shown in red (in realistic materials, some subset of these sites will be occupied), atoms are shown in grey, and M' atoms are shown in blue. The connectivity of the lithium percolation network is shown with red lines.

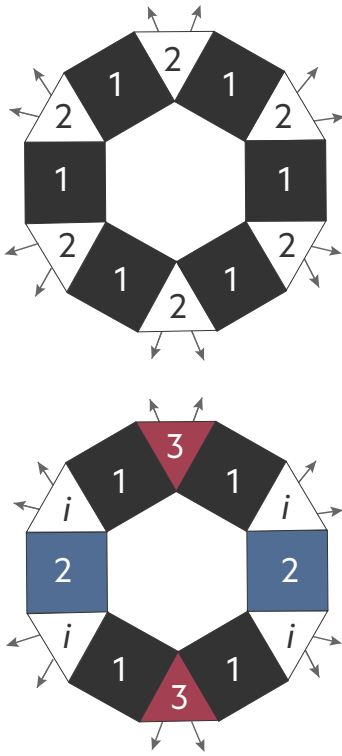
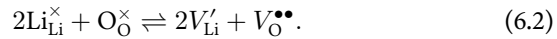


Figure 6.3: lithium distribution in the two polymorphs of LLZO. In cubic-LLZO, **top panel**, all sites are partially occupied. The **bottom panel** shows the lithium distribution in tetragonal-LLZO. Symmetrically distinct sites are labelled with different numbers, interstitial sites are denoted with *i*, and the connectivity between rings is shown with grey arrows. This figure is redrawn from [2]

suggested that oxygen vacancies may play a significant role in the defect chemistry of lithium garnets [17, 18], and Kubicek *et al.* have confirmed the presence of oxygen vacancies in a range of nominal LLZO compositions, using isotope-exchange techniques, with estimated oxygen vacancy concentrations as high as 2.5% [19]. In much the same way as a $[Al_{Li}^{\bullet\bullet}]$ defect, a charged oxygen vacancy will require a compensating defect to form to maintain macroscopic charge neutrality. The presence of oxygen vacancies has been proposed to affect lithium stoichiometry through a Schottky pair mechanism:



This defect equilibrium suggests that low $\Delta\mu_{O}$ synthesis conditions (high temperatures or low oxygen-partial-pressures) may produce lithium deficient materials. Furthermore, the appearance of V_{Li}' in both Eqns. 6.1 and 6.2 highlights the coupling between the intrinsic defect chemistry of lithium-stuffed garnets and their response to supervalent doping.

In previous studies of defects in lithium garnets, framework cationic defects, such as M and M' vacancies, are often assumed to be negligible [18] but this is not *a priori* guaranteed under all synthesis conditions. In addition, simple defect-charge-compensation models usually assume defects exist in only one formal charge state—e.g. -1 for lithium vacancies, or $+2$ for oxygen vacancies—[20] when in reality defects may adopt a range of charge states as a function of Fermi energy [21–24]. A more complete thermodynamic defect model should therefore consider a broad range of native defects in all accessible charge states.

To better understand the native defect chemistry and doping response of lithium garnet solid electrolytes, we have performed a computational study of a broad range of defects in LLZO. We have used hybrid DFT to calculate formation energies for a range of intrinsic defects, including lithium, oxygen and zirconium vacancies and interstitials, lanthanum vacancies, and cation antisites. These defect formation energies are used to construct a self-consistent thermodynamic model of defect concentrations as a function of synthesis conditions. We find a rich defect chemistry that includes not just lithium and oxygen defects, but also significant numbers of cation antisite defects. Oxygen vacancies exhibit 0, +1, and +2 charge states, and under reducing conditions act as colour-centers by trapping electrons. We have also modelled the response to supervalent doping and find that lithium vacancies do not exclusively compensate these charged species under all chemical potential regimes: under Li-rich/Zr-poor conditions donor doping is primarily compensated by Li_{Zr} antisites, and lithium stoichiometries can strongly deviate from the values predicted by a “vacancy-compensation” model.

6.2 Methods

Calculations presented in this chapter used the screened hybrid functional HSE06 [25]. All calculations were carried out in the 96 atom primitive cell of tetragonal LLZO. While typically we would use a supercell expansion to minimise the interaction between defect images in periodic DFT calculations (see Section 4.1), a large primitive cell combined with computationally intensive hybrid functionals put the consideration of larger expansions beyond reasonable computational limits. LLZO calculations used a $2 \times 2 \times 2$ Monkhorst-Pack \mathbf{k} -point mesh. For our defect calculations, we have considered lithium vacancies and interstitials, V_{Li} and Li_i ; oxygen vacancies and interstitials, V_{O} and O_i ; lanthanum and zirconium vacancies, V_{La} and V_{Zr} ; zirconium interstitials, Zr_i ; and a range of cation anti-sites: La_{Zr} , $\text{Zr}_{\text{Li}}^{\text{oct}}$, $\text{Zr}_{\text{Li}}^{\text{tet}}$, Zr_{La} , Li_{La} , $\text{La}_{\text{Li}}^{\text{oct}}$ and Li_{Zr} . A superscript oct or tet denotes a defect located at an octahedral or tetrahedral lithium site, respectively. Preliminary calculations using the GGA functional PBEsol [26] gave a difference in formation energy for $V_{\text{Li}}^{\text{oct}}$ and $V_{\text{Li}}^{\text{tet}}$ of <0.05 eV, and we therefore considered these Li vacancies to be energetically equivalent for our subsequent HSE06 calculations.

To restrict the available chemical potential space to values that are, in principle, experimentally accessible, we consider only chemical potentials for which LLZO is thermodynamically stable with respect to competing phases. We have considered the set of competing phases identified by Canepa *et al.* [27], and have calculated the thermodynamic stability regime using the code CPLAP [28].

DFT calculations were performed with valence electrons described by a plane-wave basis set with a cutoff of 520 eV. Interactions between core and valence electrons were described using the projector-augmented wave (PAW) method [29], with cores of [H] for Li, [Xe] for La, [Kr] for Zr and [He] for O. Optimised lattice parameters for LLZO, competing phases, and elemental references were obtained by performing a series of constant-volume geometry optimisation calculations, and fitting the resulting energy–volume data to the Murnaghan equation of state [30].

6.3 Intrinsic defect chemistry

The predicted region of thermodynamic stability of LLZO spans a range of values that can be broadly characterised along an oxygen-rich/metal-poor to oxygen-poor/metal-rich axis. Figure 6.4 shows calculated defect concentrations at three illustrative sets of chemical potentials, in each case, we also show a defect transition-level diagram (bottom panels). Defect concentrations are calculated at a representative synthesis temperature

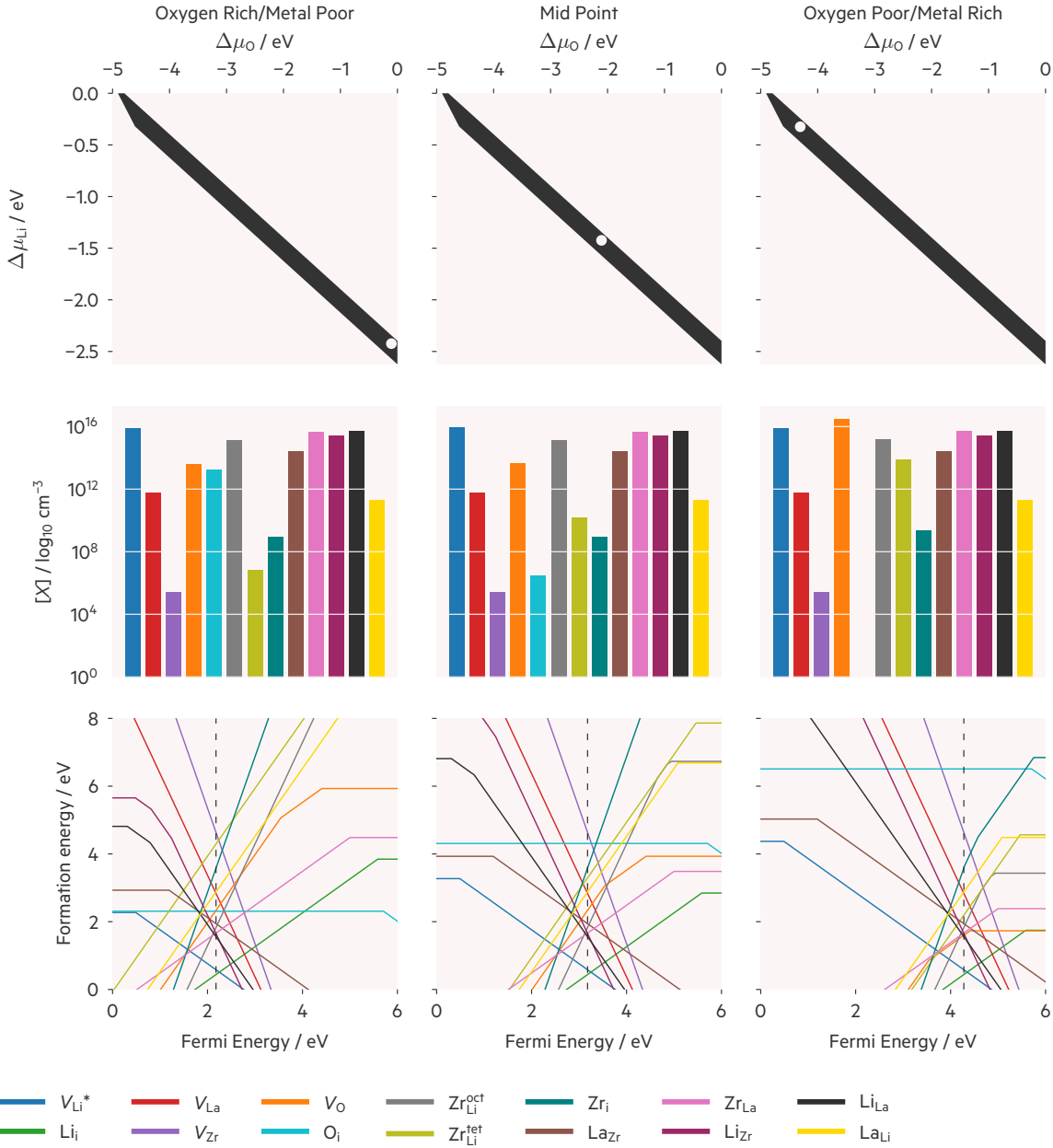


Figure 6.4: Equilibrium defect concentrations (**middle row**) and defect formation-energies as a function of Fermi energy (**bottom row**) at three sets of elemental chemical potentials (**top row**) within the LLZO thermodynamic stability region (**bottom row**). Defect concentrations are calculated at $T = 1500 \text{ K}$. In each case, the bottom panel also shows the corresponding self-consistent Fermi energy (vertical dotted line). $[V_{\text{Li}}^*]$ denotes the net lithium vacancy concentration, i.e. $[V_{\text{Li}}^*] = [V_{\text{Li}}] - [\text{Li}_{\text{i}}]$.

of 1500 K [5]. We assume that defect populations at synthesis are “frozen in” when the system is cooled to operating temperatures. This is justified on the grounds that, with the exception of the lithium interstitials and vacancies, kinetic barriers for defect reorganisation are large, preventing the system from re-equilibrating at low temperatures [31]. Lithium ions are mobile at operating temperatures, and we can therefore expect some recombination of lithium interstitials and vacancies, reducing the populations of these defects, to reflect this, reported lithium defect concentrations are given as a net value, i.e. $[V_{\text{Li}}^*] = [V_{\text{Li}}] - [\text{Li}_i]$. Unless lithium can exchange with an external source, however, the net lithium stoichiometry, and the equilibrium Fermi energy, are both fixed at their high temperature values.

Under oxygen-rich conditions the defects with the highest concentrations are V_{Li} , Li_{La} , La_{Zr} , Li_{Zr} , and Zr_{Li} . Intermediate chemical potentials give similar defect concentrations, with lithium vacancies and metal anti-sites dominating. Under oxygen-poor/metal-rich conditions the concentration of V_{O} increases, becoming the dominant defect species. Lithium vacancy and metal anti-site concentrations, however, remain high.

The analysis above considers a two-dimensional projection of the four-dimensional $\{\text{O}, \text{Li}, \text{La}, \text{Zr}\}$ chemical potential space. At a fixed value of $\Delta\mu_{\text{O}}$, varying the metal chemical potentials can cause a change in the dominant cation defect. For example, moving from lithium-rich/zirconium-poor to lanthanum-poor/zirconium-rich conditions at constant μ_{O} causes the dominant antisite defects to change from Li_{Zr} and Li_{La} to Zr_{Li} and Zr_{La} .

6.4 Variation in lithium stoichiometry

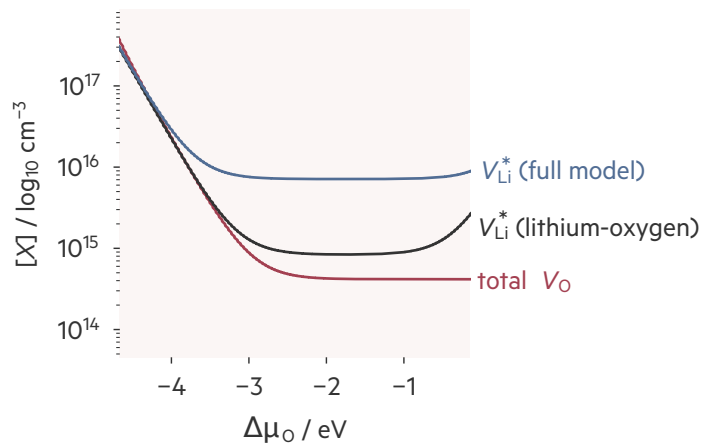
Tuning the lithium stoichiometry in lithium-stuffed garnets is a popular synthesis strategy to improve their ionic conductivities [10, 13, 15, 32]. A key question concerning the defect chemistry of these materials, therefore, is to what extent might their lithium stoichiometries differ from formal values as a function of synthesis conditions, due to native defect formation [10]. As described in the previous section, the range of chemical potentials under which LLZO is predicted to be thermodynamically stable can be characterised as lying between oxygen-rich/metal-poor and oxygen-poor/metal-rich limits. Of the component elements, the chemical potential of oxygen is perhaps most sensitive to synthesis conditions, and most easily controlled by varying temperature or oxygen partial-pressure during synthesis. Because oxygen vacancies might be expected to result in a net positive charge, it has been suggested that increasing the concentration of oxygen vacancies could cause a corresponding increase in $[V_{\text{Li}}]$, poten-

tially reducing lithium stoichiometries below their nominal values (e.g. Eqn. 6.2) [10, 19].

Previous quantitative analyses of the relationship between oxygen vacancies and lithium vacancies have used defect models that include only oxygen and lithium defect species [10, 18, 19] considering only fully charged and neutral defects [20]. In the previous section, however, we have shown that considering a broad range of defects in LLZO, in all charge states, reveals a more complex defect chemistry (Fig. 6.4). In particular, cation antisites are formed in concentrations comparable to $[V_O]$ under all thermodynamically accessible synthesis conditions. The presence of these additional defects means the relationship between oxygen and lithium stoichiometries is likely to be more complex than is predicted by charge-compensation schemes that assume only lithium point-defect concentrations can change in response to aliovalent doping.

To illustrate the effect of examining a “full” set of defects, we have calculated the lithium vacancy concentration as a function of oxygen chemical potential using two models. The first is a “lithium–oxygen” model, where we include only oxygen vacancies, lithium vacancies, and lithium interstitials. The second is an “all-defects” model that includes all the defects discussed in the previous section. For each model, we have performed a series of self-consistent Fermi energy calculations along a line in chemical potential space from oxygen-rich to oxygen-poor conditions. The predicted oxygen vacancy and lithium vacancy concentrations in each case are shown in Fig. 6.5.

Figure 6.5: Predicted V_{Li} and V_O concentrations as a function of $\Delta\mu_O$, from two comparative models: “lithium–oxygen” model, which only considers V_O , V_{Li} , and Li_i (all charge states) and “full” model including all defects considered in this current work.



The lithium–oxygen model predicts two regimes: at high $\Delta\mu_O$, the concentrations of lithium vacancies and of oxygen vacancies are both approximately independent of $\Delta\mu_O$, and the ratio of $[V_{Li}] : [V_O]$ is $\sim 2 : 1$, as expected from simple charge neutrality arguments (Eqn. 6.2). The observation that the vacancy concentrations in this regime are independent

of $\Delta\mu_{\text{O}}$ can be understood by considering the corresponding changes in the defect transition level diagrams (e.g. Figure 6.4). Being constrained by the region of thermodynamic stability for LLZO means a decrease in $\Delta\mu_{\text{O}}$ is coupled to an increase in $\Delta\mu_{\text{Li}}$. As $\Delta\mu_{\text{O}}$ decreases, the Fermi energy increases (pinned by the $V_{\text{Li}}/\text{Li}_i$ crossing point). The formation energies of V_{Li} , Li_i , and V_{O} (the latter in the +2 charge state) remain unchanged from their values at high $\Delta\mu_{\text{O}}$, and these defect concentrations are therefore also unchanged. At lower values of μ_{O} , a second regime is predicted, in which decreasing $\Delta\mu_{\text{O}}$ causes both V_{Li} and V_{O} concentrations to increase. This change in behaviour occurs when the Fermi energy becomes sufficiently high that the lowest energy V_{O} charge state changes from +2 to +1. Further decreases in $\Delta\mu_{\text{O}}$ are no longer fully compensated by increases in the Fermi energy, and the V_{O} energy starts to decrease. Because the dominant V_{O} charge state in this regime is +1 the $[V_{\text{Li}}] : [V_{\text{O}}]$ ratio decreases towards 1 : 1.

The “full” model has a similar overall shape, showing two general regimes of behaviour. The μ_{O} -independent regime is broader, however, than for the lithium–oxygen model, and lithium vacancy concentrations are higher, i.e. somewhat decoupled from the V_{O} concentrations. This is because the model now includes additional positive defects, such as $\text{Zr}_{\text{Li}}^{\bullet\bullet\bullet}$ and $\text{Zr}_{\text{La}}^{\bullet}$, with low formation energies. The transition to the $\Delta\mu_{\text{O}}$ -dependent regime occurs at a lower value of $\Delta\mu_{\text{O}}$ than in the lithium–oxygen model, and oxygen and lithium vacancy concentration are less tightly coupled. This, again, is due to the presence of other defects, particularly cation antisite defects, which buffer the response of system to changing $\Delta\mu_{\text{O}}$.

By performing this analysis across the full four-dimensional thermodynamic stability region of LLZO, we can calculate the full range of variation in lithium stoichiometry under all thermodynamically accessible synthesis conditions. Although the concentrations of individual defects vary with changing thermodynamic conditions, the net variation in lithium stoichiometry is small. We predict the minimum and maximum lithium stoichiometries of LLZO under thermodynamic equilibrium to be $x_{\text{Li}} = 6.9975$ and $x_{\text{Li}} = 7.00125$.

A simple sum over all lithium-defects does not, however, account for possible differences in mobility for lithium present as different defect species. For example, under lithium-rich/zirconium-poor conditions we predict high concentrations of Li_{Zr} antisites. The binding energy of lithium at a zirconium site can be estimated from the “Frenkel-pair” formation energy for $\text{Li}_{\text{Zr}} \rightarrow \text{Li}_i + V_{\text{Zr}}$, which we calculate as $\Delta E = +3.42$ eV. For comparison the Frenkel-pair formation energy for $\text{Li}_{\text{Li}} \rightarrow \text{Li}_i + V_{\text{Li}}$ is $\Delta E = +1.02$ eV. The much larger energy cost to remove lithium from

a zirconium site, than from a lithium site, suggests that lithium present as Li_{Zr} is strongly bound to the lattice-cation site, and is therefore not available as a mobile charge-carrier. This effect is not, however, expected to significantly affect lithium-ion conductivities, as within the regime of thermodynamic stability the maximum number of lithium ions trapped as Li_{Zr} antisites remains a small proportion of the total lithium ($\leq 0.002\%$).

A second factor that might effect lithium-ion mobilities is possible clustering of V'_{Li} and Li_i^\bullet to form associated defect pairs. Charged lithium vacancies and interstitials are expected to exhibit a mutual Coulombic attraction, giving a favourable negative defect association energy. Formation of a defect complex, however, decreases the number of independent defects in a system, and therefore decreases configurational entropy. Whether an equilibrium population of defects consists predominantly of bound complexes or of independent defects depends on the balance of these energetic and entropic contributions. These thermodynamic considerations give the approximate condition that for defect pairs to be predominantly associated at equilibrium, the defect-pair binding energy, E_{binding} , defined as

$$E_{\text{binding}} = E_{\text{pair}} - \sum_{X^q} \Delta E_f^{X^q}, \quad (6.3)$$

should be greater than the formation energy, $\Delta E_f^{X^q}$, of the individual defect species. If the inverse is true, and $\Delta E_f^{X^q} > E_{\text{binding}}$, these defects will be predominantly dissociated at equilibrium [33].

To assess this behaviour in LLZO, we have calculated formation energies for $V_{\text{Li}}-\text{Li}_i$ defect pairs separated by 4.16 Å and by 6.13 Å. 4.16 Å corresponds to the shortest $V_{\text{Li}}-\text{Li}_i$ distance at which these defects do not simply recombine during geometry optimisation, while 6.13 Å is the largest possible separation in the 96 atom primitive cell.¹ These calculations give a defect-pair association energy of 0.09 eV. Comparing the energy of the “associated” defect pair directly with the separate V'_{Li} and Li_i^\bullet formation energies gives a defect-pair association energy of 0.19 eV.

¹ Calculations performed using PBEsol in a 192 atom conventional cell indicate that $V_{\text{Li}}-\text{Li}_i$ pairs separated by more than 4.16 Å give a converged “well-separated” energy.

6.5 Oxygen vacancy charge states and diffusion

Although the oxygen-vacancy concentration is not predicted to directly affect the lithium-vacancy concentration, except under oxygen-poor conditions, we do predict a wide range of equilibrium concentrations for oxygen vacancies, varying from a slightly oxygen-rich material ($[\text{O}_i^*] = 2.56 \times 10^{13} / \text{cm}^3$) to an oxygen-poor material ($[\text{V}_\text{O}^*] = 6.53 \times 10^{17} / \text{cm}^3$) across the LLZO thermodynamic stability region. Oxygen vacancies have previously been suggested to affect the electronic, optical, and ion-conduction properties of lithium-garnets [17, 19]. In this section, we first

examine the electronic properties of oxygen vacancies, and then consider their capacity to diffuse through the garnet lattice, thereby potentially contributing to net ionic conductivities.

The simple “Schottky-pair” charge-compensation model of oxygen vacancy formation (Eqn. 6.2) considers oxygen vacancies to have a formal charge of +2. Our calculations predict that at low $\Delta\mu_{\text{O}}$ the favoured oxygen-vacancy charge state is +1, or even 0; oxygen vacancy formation leaves behind one, or two, electrons to be accommodated within the host lattice. In oxides containing reducible cations, such as TiO_2 , excess electrons from donor defects, such as V_{O} , are typically accommodated by reducing these cations (e.g. for TiO_2 this formally corresponds to reduction from Ti^{4+} to Ti^{3+} [34, 35]). LLZO does not contain any cations normally considered to have alternate accessible oxidation states. We find that excess electrons from V_{O} formation can be trapped at the vacant oxygen site to form occupied defect states lying deep in the band gap (Fig. 6.6), i.e. oxygen vacancies act as F-centers under reducing, or n-type, conditions. This behaviour is consistent with the experimental observations of Wolfenstein *et al.* who observed colouration of LLZO samples heated in (highly reducing) molten lithium, associated with the appearance of a characteristic electronic paramagnetic resonance signal proposed to correspond to unpaired electrons trapped at color centres [17].

Kubicek *et al.* have proposed that diffusion of oxygen vacancies in LLZO may contribute to net ionic conductivities [19]. To evaluate the capacity for diffusion by V_{O} , we have performed climbing-image nudged-elastic-band (CI-NEB) calculations [36] on the six symmetry inequivalent V_{O} diffusion pathways between nearest-neighbour oxygen-site pairs. We find the lowest diffusion barrier is 0.73 eV, which is similar to the barriers in high-temperature oxide-ion conductors [37, 38]. This suggests oxygen conduction does not make a significant contribution to net ionic conductivities under typical battery operating conditions, in agreement with the experimental analysis of Kubicek *et al.* [19]. Oxygen vacancies may, however, diffuse through the host structure during high-temperature sintering.

6.6 Response to supervalent doping

Having evaluated the native defect chemistry of LLZO as a function of synthesis conditions, we now consider the response to extrinsic doping by supervalent species. Here, we scale the predicted doping response using a generic “2+” dopant, such as a trivalent cation at a lithium site, $M_{\text{Li}}^{\bullet\bullet}$. Within a simple charge compensation model (Equation (6.1)) each dopant is expected to produce two charge-compensating lithium vacancies. Fig-

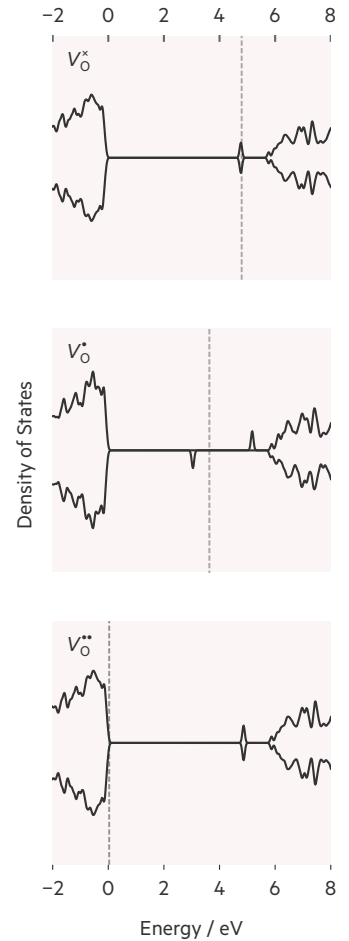


Figure 6.6: Density of states for structures containing oxygen vacancies in 0, +1, and +2 charge states. The valence-band maximum is aligned to 0 eV. The grey line indicates the position of the Fermi level.

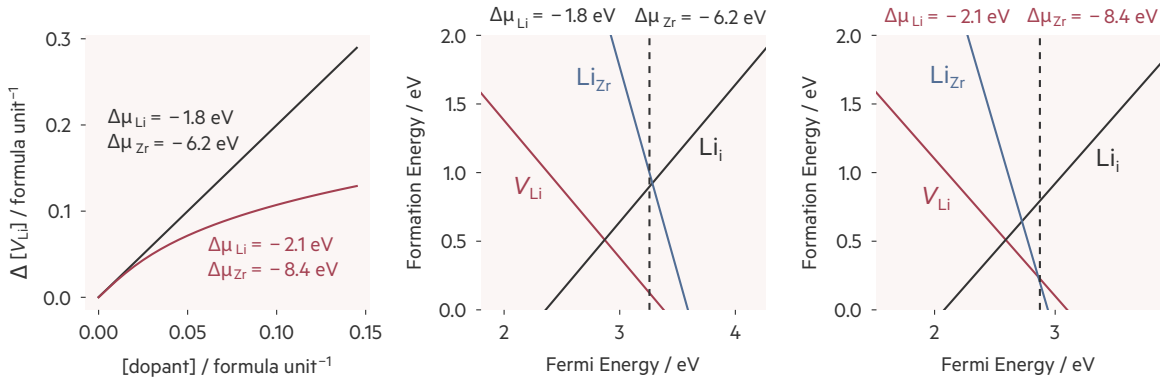


Figure 6.7: (a) Increase in lithium vacancy concentration as the amount of dopant $M_{Li}^{\bullet\bullet}$ per formula unit is increased for two different sets of chemical potentials. (b) and (c) Transition level diagrams for the two cases in (a). In each diagram we show the Fermi level position after supervalent (dashed vertical black line) doping (0.15 $M_{Li}^{\bullet\bullet}$ per formula unit). For clarity, here we only show the V_{Li} (red line), Li_i (black line), and Li_{Zr} (blue line) formation energies.

Figure 6.7(a) shows the calculated *excess* lithium vacancy concentration, relative to the corresponding undoped system, under two sets of chemical potentials. In the first example ($\Delta\mu_{Li} = -1.8 \text{ eV}$, $\Delta\mu_{Zr} = -6.2 \text{ eV}$, $\Delta\mu_{La} = -5.2 \text{ eV}$, $\Delta\mu_{O} = -1.6 \text{ eV}$) the doping response exactly follows the prediction of the simple charge-compensation model. Additional lithium vacancies are introduced in a 2:1 ratio to the number of $M_{Li}^{\bullet\bullet}$ dopants. In the second example, however, ($\Delta\mu_{Li} = -2.1 \text{ eV}$, $\Delta\mu_{Zr} = -8.4 \text{ eV}$, $\Delta\mu_{La} = -6.5 \text{ eV}$, $\Delta\mu_{O} = -0.7 \text{ eV}$), the number of excess lithium-vacancies is significantly lower than expected, with a negative deviation from the previous 2:1 ratio that becomes larger with increasing dopant concentration.

These contrasting behaviours can be understood by examining the transition level diagrams in each case, and considering the effects of changing the Fermi level when introducing dopants. Figs. 6.7b and 6.7c, respectively, show the two transition level diagrams for each set of chemical potentials. For clarity we only show the relevant lowest formation-energy defects: V_{Li} , Li_i , and Li_{Zr} . These two figures also show the self-consistent Fermi level calculated for the undoped system ($[M^{\bullet\bullet}] = 0$) and for $[M^{\bullet\bullet}] = 0.15 / \text{formula unit}$. In both cases, when undoped, the Fermi energy is pinned slightly below the V_{Li} / Li_i crossing point. Adding donor dopants to the system increases the Fermi energy. In the absence of low-energy competing defects (Fig. 6.7b) this decreases the V_{Li} energy, and increases the Li_i energy, resulting in an increased concentration of lithium vacancies. In the second case, the $\Delta\mu_{Li}$ chemical potential is relatively high compared to $\Delta\mu_{Zr}$, and increasing the Fermi level through doping causes the Li_{Zr}' formation energy to fall below that of V_{Li}' . For sufficiently high dopant concentrations, therefore, the Fermi energy is shifted high enough that Li_{Zr} becomes the dominant negative defect. Further supervalent doping will now *increase* the amount of lithium in the system, as the concentration of Li_{Zr} increases more rapidly than that of V_{Li} . These lithium

defects are not expected to contribute to the total lithium conductivity (see the discussion of Li_{Zr} binding in the previous section).

6.7 Summary and discussion

In this chapter, we have considered the defect chemistry of the prototypical lithium-stuffed garnet LLZO, by performing hybrid density-functional theory calculations on a broad range of defects, and calculating self-consistent defect concentrations as a function of component chemical potentials and dopant concentrations. For the native defects, we find a rich family of defect species, including lithium and oxygen vacancies and interstitials, which have been discussed previously [18–20, 39], and cation antisites; such as Li_{La} , La_{Zr} , Li_{Zr} , and Zr_{Li} , which are often neglected when considering the defect chemistry of lithium-garnets. Under all conditions except extremely oxygen-poor (reducing) conditions, cation anti-site defects are the highest concentration defect species after V_{Li} and Li_i . The existence of multiple native positive and negative defect species means the net lithium stoichiometry is somewhat insensitive to synthesis conditions, or rather oxygen chemical potential during synthesis. We predict that in undoped LLZO under equilibrium conditions the lithium stoichiometry deviates from its nominal value of $x_{\text{Li}} = 7$ by only $+0.00125/-0.0025$.

Under strongly reducing conditions, oxygen vacancies are stable in $+1$ or neutral charge states, and act as colour-centres by trapping electrons. We predict the lowest barrier for oxygen vacancy diffusion is 0.73 eV, which suggests that vacancy-mediated oxygen conduction is not significant at typical battery-operating temperatures, in agreement with previous experimental analysis [19], although oxygen vacancies may readily diffuse during high-temperature sintering of samples.

We also find that the response to supervalent doping depends on thermodynamic conditions, and broadly depends on a balance between lithium and zirconium chemical potentials. Under relatively low μ_{Li} / high μ_{Zr} conditions, supervalent doping produces proportionate numbers of charge-compensating lithium vacancies, as is often commonly assumed (e.g. Eqn. 6.1). Under relatively high μ_{Li} / low μ_{Zr} conditions, however, supervalent doping is chiefly compensated by Li_{Zr} antisites, and lithium stoichiometries strongly deviate from those predicted by mobile-ion point defect compensation models. This result means that synthetic recipes that use doping to tune the lithium stoichiometry in LLZO may not be able to assume direct compensation by lithium vacancies, as the dominant charge-compensating defect can vary with synthesis conditions.

Bibliography

- (1) Famprikis, T.; Canepa, P.; Dawson, J. A.; Islam, M. S.; Masquelier, C. *Nat. Mater.* **2019**, *21*, 1–14.
- (2) Morgan, B. *J. R. Soc. Open Sci.* **2017**, *4*, 170824–21.
- (3) Burbano, M.; Carlier, D.; Boucher, F.; Morgan, B. J.; Salanne, M. *Phys. Rev. Lett.* **2016**, *116*, 135901–6.
- (4) He, X.; Zhu, Y.; Mo, Y. *Nature Comm.* **2017**, *8*, 15893.
- (5) Thangadurai, V.; Narayanan, S.; Pinzaru, D. *Chem. Soc. Rev.* **2014**, *43*, 4714.
- (6) Liu, Q.; Geng, Z.; Han, C.; Fu, Y.; Li, S.; He, Y.-b.; Kang, F.; Li, B. *J. Power Sources* **2018**, *389*, 120–134.
- (7) Awaka, J.; Takashima, A.; Kataoka, K.; Kijima, N.; Idemoto, Y.; Akimoto, J. *Chem. Lett.* **2011**, *40*, 60–62.
- (8) Cussen, E. *J. Mater. Chem.* **2010**, *20*, 5167–5173.
- (9) Zeier, W. G. *Dalton Trans.* **2014**, *43*, 16133–16138.
- (10) Mukhopadhyay, S.; Thompson, T.; Sakamoto, J.; Huq, A.; Wolfenstine, J.; Allen, J. L.; Bernstein, N.; Stewart, D. A.; Johannes, M. D. *Chem. Mater.* **2015**, *27*, 3658–3665.
- (11) Kozinsky, B.; Akhade, S. A.; Hirel, P.; Hashibon, A.; Elsässer, C.; Mehta, P.; Logéat, A.; Eisele, U. *Phys. Rev. Lett.* **2016**, *116*, 055901–5.
- (12) Geiger, C. A.; Alekseev, E.; Lazic, B.; Fisch, M.; Armbruster, T.; Langner, R.; Fechtelkord, M.; Kim, N.; Pettke, T.; Weppner, W. *Inorg. Chem.* **2011**, *50*, 1089–1097.
- (13) Brugge, R.; Kilner, J.; Agüero, A. *Solid State Ion.* **2019**, *337*, 154–160.
- (14) Pesci, F. M.; Brugge, R. H.; Hekselman, A. K. O.; Cavallaro, A.; Chater, R. J.; Agüero, A. *J. Mater. Chem. A* **2018**, *6*, 19817–19827.
- (15) Li, Y.; Han, J. T.; Wang, C. A.; Xie, H.; Goodenough, J. B. *J. Mater. Chem.* **2012**, *22*, 15357.
- (16) Yeandel, S. R.; Chapman, B. J.; Slater, P. R.; Goddard, P. *J. Phys. Chem. C* **2018**, *122*, 27811–27819.
- (17) Wolfenstine, J.; Allen, J. L.; Read, J.; Sakamoto, J. *J. Mater. Sci.* **2013**, *48*, 5846–5851.
- (18) Zhan, X.; Lai, S.; Gobet, M. P.; Greenbaum, S. G.; Shirpour, M. *Phys. Chem. Chem. Phys.* **2018**, *20*, 1447–1459.

- (19) Kubicek, M.; Wachter-Welzl, A.; Rettenwandler, D.; Wagner, R.; Berendts, S.; Uecker, R.; Amthauer, G.; Hutter, H.; Fleig, J. *Chem. Mater.* **2017**, *29*, 7189–7196.
- (20) Moradabadi, A.; Kaghazchi, P. *Solid State Ion.* **2019**, *338*, 74–79.
- (21) Zhang, S. B.; Northrup, J. E. *Phys. Rev. Lett.* **1991**, *67*, 2339–2342.
- (22) Van de Walle, C. G.; Laks, D. B.; Neumark, G. F.; Pantelides, S. T. *Phys. Rev. B* **1993**, *47*, 9425–9434.
- (23) Persson, C.; Zhao, Y.-J.; Lany, S.; Zunger, A. *Phys. Rev. B* **2005**, *72*, 035211.
- (24) Freysoldt, C.; Grabowski, B.; Hickel, T.; Neugebauer, J.; Kresse, G.; Janotti, A.; Van de Walle, C. G. *Rev. Mod. Phys.* **2014**, *86*, 253–305.
- (25) Krukau, A. V.; Vydrov, O. A.; Izmaylov, A. F.; Scuseria, G. E. *J. Chem. Phys.* **2006**, *125*.
- (26) Perdew, J.; Ruzsinszky, A.; Csonka, G.; Vydrov, O.; Scuseria, G.; Constantin, L.; Zhou, X.; Burke, K. *Phys. Rev. Lett.* **2008**, *100*, 136406.
- (27) Canepa, P.; Dawson, J. A.; Sai Gautam, G.; Statham, J. M.; Parker, S. C.; Islam, M. S. *Chem. Mater.* **2018**, *30*, 3019–3027.
- (28) Buckeridge, J.; Scanlon, D. O.; Walsh, A.; Catlow, C. R. *Comput. Phys. Comm.* **2014**, *185*, 330–338.
- (29) Blöchl, P. E. *Phys. Rev. B* **1994**, *50*, 17953–17979.
- (30) Murnaghan, F. D. *Proc. Natl. Acad. Sci.* **1944**, *30*, 244–247.
- (31) Maier, J. *Phys. Chem. Chem. Phys.* **2003**, *5*, 2164–2173.
- (32) Allen, J. L.; Wolfenstine, J.; Rangasamy, E.; Sakamoto, J. J. *Power Sources* **2012**, *206*, 315–319.
- (33) Neugebauer, J.; Van de Walle, C. G. *MRS Proceedings* **1995**, *395*, 645.
- (34) Morgan, B. J.; Watson, G. W. *Surf. Sci.* **2007**, *601*, 5034–5041.
- (35) Morgan, B. J.; Watson, G. W. *J. Phys. Chem. C* **2010**, *114*, 2321–2328.
- (36) Henkelman, G.; Uberuaga, B. P.; Jónsson, H. *J. Chem. Phys.* **2000**, *113*, 9901–9904.
- (37) Cherry, M.; Islam, M.; Catlow, C. *J. Sol. Stat. Chem.* **1995**, *118*, 125–132.
- (38) Taylor, F. H.; Buckeridge, J.; Catlow, C. R. A. *Chem. Mater.* **2016**, *28*, 8210–8220.
- (39) KC, S.; Longo, R. C.; Xiong, K.; Cho, K. *Solid State Ion.* **2014**, *261*, 100–105.

Statement of Authorship

The following chapter concerns the article entitled **Low Electronic Conductivity of $\text{Li}_7\text{La}_3\text{Zr}_2\text{O}_{12}$ (LLZO) Solid Electrolytes from First Principles** currently **in review** and has been made available on ChemRxiv (available under the DOI [10.33774/chemrxiv-2021-zvwhh-v2](https://doi.org/10.33774/chemrxiv-2021-zvwhh-v2)).

This preprint reports on original research I conducted during the period of my Higher Degree by Research candidature.

Personal contributions: Formulation of ideas (70%): Prof. Aron Walsh initially proposed the study based of the data discussed in the previous chapter. With his help and the help of Dr. Daniel Davies I conceptualised the practical aspects of the work. Design of methodology (80%): After instruction in how to calculate the carrier mobilities from Dr. Daniel Davies I designed the additional DFT calculations and analysis code required. Dr. Sunghyun Kim suggested taking an approach which would keep the lithium off-stoichiometry fixed during self-consistent Fermi energy solutions. Experimental work (90%): I carried out all practical aspects of the work expect for the phonon frequency averaging procedure that was carried out by Dan Davies. Presentation of data in journal format (70%): The first drafts of the preprint were written by myself with input from Dr Benjamin Morgan. The finalised manuscript was prepared by Dr. Benjamin Morgan and myself with input from all co-authors.

Signed: _____

Date: _____

15/3/22

Context

In 2019, a relationship was drawn between non-negligible electronic conductivity and dendrite-driven failure in lithium solid-electrolyte battery cells [1]. It was proposed that some population of mobile electrons within the solid-electrolyte could reduce Li^+ to lithium metal, creating sites for the nucleation of lithium deposits which could then grow to form an electrical contact between the anode and the cathode. Ultimately, this would cause the battery to fail by short circuit. One of the proposed high-electronic-conductivity solid-electrolytes was LLZO. Analogously to mobile ions, the conductivity of electronic charge carriers is a product of their mobility and concentration. The concentration of free electronic carriers in a material with a finite bandgap can be calculated from a knowledge of the point defect formation energies [2]. Combining the results in the previous chapter with an approximate model for the mobility of electronic carriers in LLZO, in this chapter we predict the bulk electronic conductivity of LLZO using computational methods. Not only is this relevant in the context of potential dendrite-driven failure mechanisms, but also, the electronic conductivity of solid electrolytes should be minimal to prevent current leakage occurring via direct transport of electrons between the electrodes, via the solid electrolyte [3, 4].

This study has gained some additional urgency based off the recent suggestion that point defect formation within the bulk can indeed be linked to a non-negligible electronic conductivity in sulfide solid electrolytes [5]. In this work it is implied that this prediction may be extensible to other solid electrolytes such as LLZO. We find in our study of the electronic conductivity of LLZO that this material has all the properties of an excellent electronic insulator. By extension, it is likely that non-negligible electronic conductivity in LLZO is associated with extended defects [6]. Our calculated electron and hole mobilities only consider a single source of potential carrier scattering, and so these are ultimately an upper limit estimate for electron and hole transport in LLZO. We find, however, that ultimately the limiting factor for any potential electronic conductivity in bulk LLZO is a vanishingly small carrier concentration under operating conditions. While it may prove interesting to study the atomistic mechanisms for electron transport in LLZO in greater depth, this will likely be a more fruitful pursuit at extended defects.

This chapter follows the same structure as the associated preprint (see statement of authorship), however, it has been edited to remove information that would otherwise be redundant owing in the context of this thesis and to better reflect the overall narrative of this dissertation.

7.1 Introduction

The principal requirement for a practical solid-electrolyte is fast ion-conduction. As a consequence, significant research effort has been expended on developing an understanding of the physical principles that govern fast lithium-ion transport [7–12] and on the discovery of new highly-conducting solid electrolytes [13–17]. Other material properties are also desirable for the practical use of a solid electrolyte, including good electrochemical stability over a wide voltage operating range [18], sufficient mechanical strength to impede dendrite propagation [19], and low interfacial and grain boundary resistivities [20, 21]. The development of practical solid electrolytes for use in all-solid-state batteries therefore requires a clear understanding of a broad range of relevant material properties in candidate materials, and how these properties may be controlled by tuning synthesis conditions or through targeted chemical modification [22–24].

One additional property that can affect solid electrolyte performance is *electronic* conductivity. An ideal solid electrolyte should have minimal electronic conductivity to avoid gradual self-discharge [3, 4]. Non-negligible electronic conductivities have also been suggested as a possible contributing factor in lithium dendrite growth processes wherein mobile Li^+ is directly reduced to metallic Li^0 within the solid-electrolyte bulk [1, 25, 26].¹ These dendrites can grow to provide an electrical contact between the electrodes, causing the battery to fail by short circuit. Recent work by Han *et al.* has shown that this “bulk” dendrite growth is more prevalent in solid electrolytes with high electronic conductivities [1], leading to the suggestion that electronic conductivity is a critical parameter that determines the degree to which a given solid electrolyte is susceptible to this dendrite nucleation and growth process. On this basis, Han *et al.* have proposed empirical upper limit thresholds for total electronic conductivity for a solid electrolyte to resist dendrite growth via this bulk nucleation mechanism of $10^{-10} \text{ S cm}^{-1}$ and $10^{-12} \text{ S cm}^{-1}$ at current densities of 1 mA cm^{-2} and 10 mA cm^{-2} , respectively [1].

Despite the potential impact of non-zero electronic conductivities on the practical use of solid electrolytes in all-solid-state batteries—particularly in cells that use lithium-metal anodes—a detailed characterisation of solid electrolyte electronic conductivities, and their dependence on factors such as synthesis conditions and sample stoichiometry, is lacking for many materials. Experimental measurements of electronic conductivities are usually performed on polycrystalline otherwise morphologically complex samples, and non-negligible electronic conductivity values are typically attributed to contributions from grain boundaries or

¹ An analogous degradation process due to reduction of Na^+ to Na resulting from electronic conduction has been discussed for Na-beta-alumina [27, 28].

surfaces [26, 29], with any residual bulk contributions considered to be negligible. While it may be the case that for many solid electrolytes their macroscopic electronic conductivities are dominated by “extrinsic” contributions, i.e., those arising from surfaces and grain boundaries, it is still useful to characterise the “intrinsic” bulk electronic conductivities of solid electrolytes. As one example, if the bulk electronic conductivity is small with respect to surface and grain boundary contributions then this bulk value provides a lower limit to the net macroscopic electronic conductivity that might be obtained even under “optimal” morphological control (e.g., through sintering or surface treatment). Solid electrolytes with bulk electronic conductivities that are higher than the threshold values proposed by Han *et al.* therefore may be fundamentally incompatible with lithium metal anodes because they are inherently susceptible to internal dendrite nucleation, irrespective of any subsequent processing [30].

The direct experimental measurement of solid electrolyte bulk electronic conductivities can be technically challenging, and has been reported for only a few cases [3]. Bulk electronic conductivities, alternatively, can be calculated entirely from first principles using schemes based on electronic structure methods. These computational models are defined in terms of relevant thermodynamic conditions, i.e., elemental chemical potentials and temperature, and net stoichiometry. First-principles models can therefore be used to map how bulk electronic conductivities vary as a function of experimental variables, such as synthesis conditions or deliberate extrinsic doping, which in turn can give insight into how experimental synthesis protocols might be optimised to limit the impact of residual bulk electronic conductivities on overall electrolyte performance.

In this chapter, we calculate the bulk electronic conductivity of the lithium garnet solid electrolyte tetragonal- $\text{Li}_7\text{La}_3\text{Zr}_2\text{O}_{12}$ (LLZO), as a function of synthesis conditions (via the component chemical potentials) and aliovalent (supervalent) doping. We find that electrons and holes in LLZO have low mobilities ($< 1 \text{ cm}^2 \text{ V}^{-1} \text{ s}^{-1}$) and electronic carrier populations are vanishingly small under standard operating conditions in both undoped and doped samples. These factors suggest that the bulk electronic conductivity of LLZO is not sufficiently high to cause lithium-dendrite formation during cell operation by direct reduction of lithium ions to lithium metal within the bulk material. We therefore conclude that non-negligible electronic conductivities measured in experimental lithium garnet samples, and any associated potential for dendrite nucleation and growth, are likely due to contributions from extended defects or surfaces, and that morphological control is therefore critical to limit lithium dendrite growth due to electronic conductivity.

7.2 Theory

In this section, we reframe the discussion in Chapter 2 to explicitly discuss electronic conductivity in the context of defect chemistry, however, many principles of the key remain the same. The electronic conductivity σ_{elec} , of a semiconductor is given by

$$\sigma_{\text{elec}} = e[e']\mu_{\text{elec}}^{\text{mob}} + e[h^\bullet]\mu_{\text{hole}}^{\text{mob}}, \quad (7.1)$$

where $[e']$ and $[h^\bullet]$ are the concentrations of free electrons and holes respectively, e is the magnitude of charge of each carrier species (the elementary charge), and μ_e^{mob} and $\mu_{\text{hole}}^{\text{mob}}$ are the electron and hole mobilities. For wide-gap materials, such as solid electrolytes, the thermal energy at room-temperature is insufficient to generate free carriers by directly exciting electrons from the valence band to the conduction band. The presence of point defects, however, can produce free charge carriers by pinning the Fermi level close to the conduction-band or valence-band edge increasing the number of thermally generated electrons or holes, respectively [31, 32]. Aliovalent doping can also shift the position of the Fermi energy within the band gap. By varying synthesis conditions and doping protocol, therefore, the Fermi energy could move close enough to either the valence- or conduction-band edge that the population of thermally generated electronic charge carriers is sufficiently high to give a non-negligible electronic conductivity [30].

Electron and hole carrier concentrations can be calculated as functions of the Fermi energy, E_{Fermi} , and the bulk electronic density of states, $g(E)$;

$$[e'] = \int_{E_g}^{\infty} \frac{1}{\exp[(E - E_{\text{Fermi}})/k_B T] + 1} g(E) dE \quad (7.2)$$

$$[h^\bullet] = \int_{-\infty}^{E_{\text{vbm}}} 1 - \frac{1}{\exp[(E - E_{\text{Fermi}})/k_B T] + 1} g(E) dE. \quad (7.3)$$

where k_B is the Boltzmann constant and T is the temperature [33]. Point defect concentrations are given by

$$[X^q] = N_0^X \exp\left(\frac{\Delta E_f^{X,q}[E_{\text{Fermi}}, \Delta\mu_i]}{k_B T}\right), \quad (7.4)$$

where N_0^X is the density of available sites for defect X , $\Delta E_f^{X,q}$ is the formation energy of defect X in charge-state q , which in turn depends on the Fermi energy, E_{Fermi} , and $\Delta\mu_i$ are the chemical potentials of any atomic species added to or removed from the system when forming each defect [34, 35]. Equations 7.2, 7.3, and 7.4 are coupled by a common Fermi energy, which itself is constrained by the requirement that the system is net charge-neutral—the charge-density contributions from electrons,

holes, and any charged point-defects must sum to zero;

$$\rho(E_{\text{Fermi}}) = \sum_{X^q} q[X^q] + [\text{h}^\bullet] - [\text{e}'] = 0 \quad (7.5)$$

where $\rho(E_{\text{Fermi}})$ is the charge density. Calculating equilibrium carrier concentrations under specific synthesis conditions—which define the external chemical potentials—consists of finding a self-consistent solution to Equations 7.2, 7.3, and 7.4, subject to the charge-neutrality constraint expressed in Equation 7.5 [34, 36].

The effect of extrinsic dopants can be accounted for by including an additional term in Equation 7.5 [36, 37]. For a dopant M with relative charge r and fixed concentration $[M^r]$, $\rho(E_{\text{Fermi}})$ becomes

$$\rho(E_{\text{Fermi}}, r[M^r]) = \sum_{X^q} q[X^q] + [\text{h}^\bullet] - [\text{e}'] + r[M^r]. \quad (7.6)$$

In the dilute-defect limit there is no direct interaction between dopants and native defects, and the doping response does not depend explicitly on the choice of dopant species and insertion site but only on the product $r[M^r]$. The necessary inputs to solve Equations 7.2–7.6 are the reference elemental chemical potentials, which are restricted by the condition that the defect host material must be thermodynamically stable with respect to likely degradation products, the native defect formation energies, and the electronic density of states for the non-defective system.

The mobilities of the electron and hole charge carriers— $\mu_{\text{elec}}^{\text{mob}}$ and $\mu_{\text{hole}}^{\text{mob}}$, respectively are dependent on the effective mass of the carrier: a renormalisation of the carrier mass accounting for the periodic potential experienced by the carrier in the crystal, m^* , and the frequency of scattering events which can change the direction or energy of the carrier. For example, in ionic systems, when an ion is displaced, a significant amount of charge is displaced also. This can cause a local electric field significant enough to alter the motion of the electron. This process is known as optical phonon scattering [38]. Interactions between a dynamic lattice and an electronic charge carrier are known as polarons, a form of quasiparticle, which will have a different mobility to that of a “free” electron with effective mass m^* . Robust methodologies for calculating polaron mobilities has been an intense subject of research for condensed matter physicists for some decades now [39–41]. Building on the work of Herbert Fröhlich, Richard Feynman managed to frame the problem of how to calculate polaron mobility as an alternate quasiparticle which acted as an electron (with renormalised mass) interacting with a mass via a harmonic spring [42, 43]. The mobility of this quasiparticle is dependant on the strength of the interaction between the ionic motion and the electron, characterised

by the dimensionless “coupling-constant” α ,

$$\alpha = \frac{1}{4\pi\epsilon_0} \frac{1}{2} \left(\frac{1}{\epsilon} - \frac{1}{\epsilon_e} \right) \frac{e^2}{\hbar\Omega} \left(\frac{2m^*\Omega}{\hbar} \right)^{1/2} \quad (7.7)$$

where m^* is the electron or hole effective mass, ϵ_0 is the permittivity of free space, ϵ is the total dielectric response of the material, and ϵ_e is the electronic dielectric response. Ω is an average over the vibrational frequencies of the scattering phonons weighted by the amount of charge displaced by the ionic motion. These phonon frequencies can be derived from the output of the dielectric constant calculations. A large value of α ($\alpha \gg 1$) indicates strong electron-phonon interactions. Temperature dependant mobility can then be calculated as a function of α [41]. The solution for temperature dependant mobility is, however, non-trivial. We have used the implementation in the open-source JULIA package POLARONMOBILITY [44]. Importantly, however, as the approach used here to calculating carrier mobilities considers only one scattering process we obtain an upper limit value for the carrier mobilities in a perfect crystal.

7.3 Carrier concentrations

The predicted region of thermodynamic stability of LLZO described in Chapter 6 spans a range of values in four-dimensional chemical-potential space that can be broadly characterised along an O-rich/metal-poor \rightarrow O-poor/metal-rich axis. To further restrict this region to values corresponding to typical synthesis conditions, we relate the oxygen chemical potential to the synthesis pressure, P , and temperature, T , via

$$\Delta\mu_{\text{O}}(T, P) = \frac{1}{2} \left\{ C_p(T - T_0) - T \left[S_0 + C_p \ln \frac{T}{T_0} + k_B \ln \frac{P}{P_0} \right] \right\}, \quad (7.8)$$

using the experimental value for the oxygen standard entropy, $S_0 = 205 \text{ J mol}^{-1} \text{ K}^{-1}$ [45]. Assuming oxygen behaves as an ideal gas, we use $C_p = (7/2) k_B$ for the constant-pressure specific-heat-capacity per diatomic molecule. This approach reproduces well experimentally tabulated values of $\Delta\mu_{\text{O}}(T, P)$, with a maximum error of $\sim 15 \text{ meV}$ at the higher end of the temperature range under which LLZO is typically synthesised (1500 K) [46, 47]. The full thermodynamic-stability region of LLZO (as discussed in Chapter 6) is limited by the additional constraints we place on the oxygen chemical potential, corresponding to synthesis temperatures of 1000 to 1500 K, and oxygen partial pressures of 1 to 1×10^{-10} atm. The reduced synthetically accessible chemical potential volume is plotted in the $\{\Delta\mu_{\text{Li}}, \Delta\mu_{\text{O}}\}$ plane in Fig. 7.1.

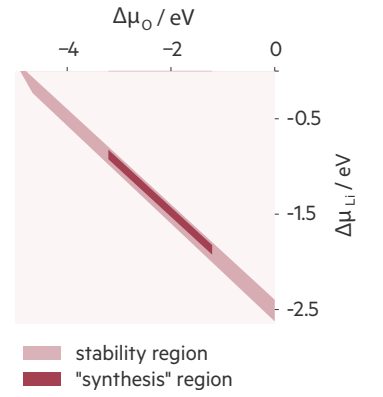


Figure 7.1: Chemical potential stability region of LLZO in the $\{\Delta\mu_{\text{Li}}, \Delta\mu_{\text{O}}\}$ plane. The dark red region is constricted by Equation 7.8 to represent synthesis conditions ranging from $T = 1000$ to 1500 K and $P_{\text{O}_2} = 1$ to $1 \times 10^{-10} \text{ atm}$.

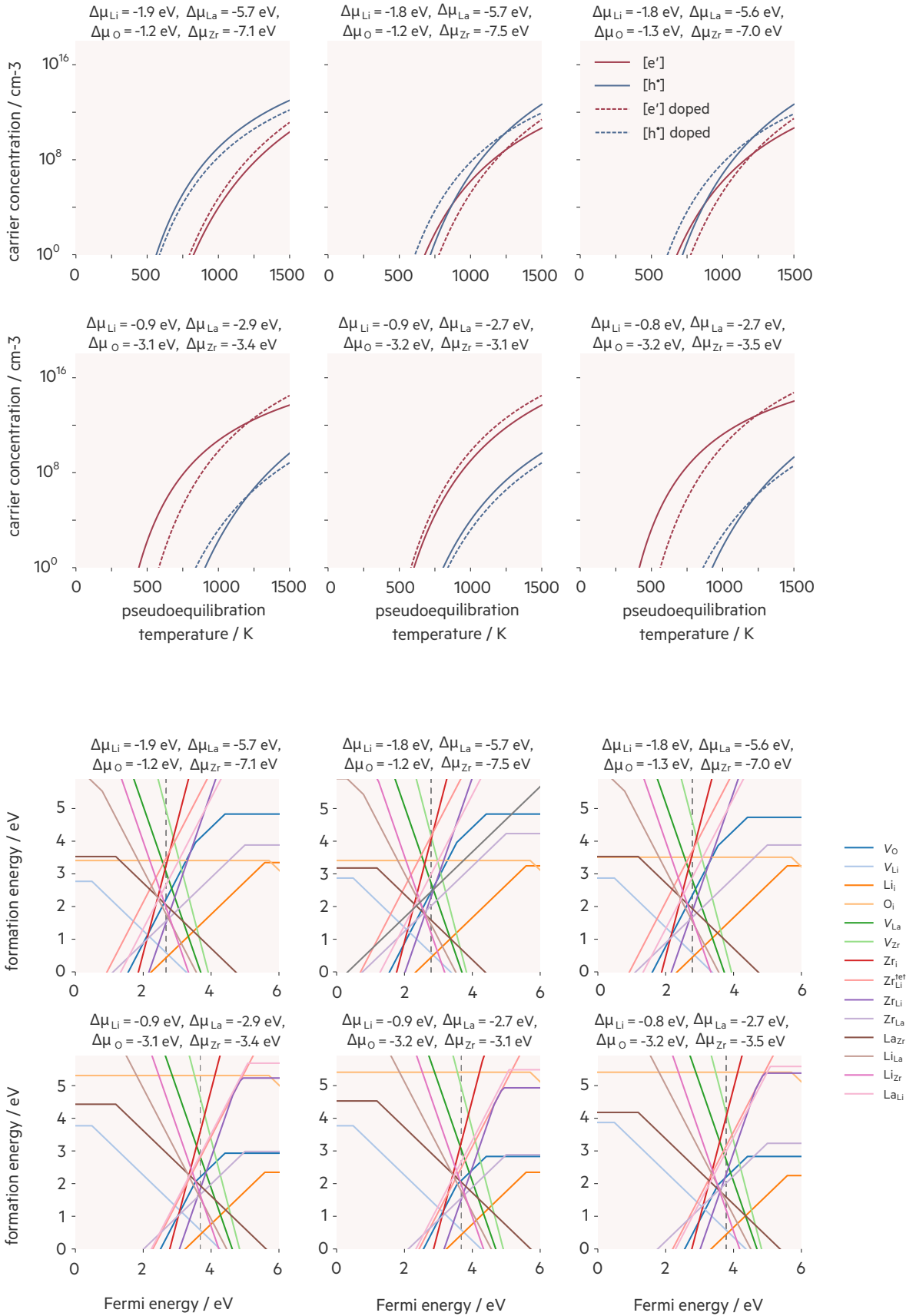


Figure 7.2: the **top six panels** show $[e']$ and $[h^\bullet]$ carrier concentrations at six sets of chemical potentials (each set corresponds to a vertex of the estimated chemical potential stability region that LLZO can be synthesised within). The chemical potentials used to calculate defect concentrations are shown above each plot. The carrier concentrations are calculated at 1500 K initially, the concentrations of all defects other than lithium vacancies, interstitials and electron and hole concentrations are then fixed to these high temperature values for subsequent, lower temperature solutions. All carrier concentrations are given for both a undoped sample, and a sample containing 0.15 per formula unit of some dopant M^{2+} . The **bottom six panels** show the transition level diagrams calculated at each set of chemical potentials for which carrier concentrations are calculated.

While LLZO is typically synthesised at high temperature (up to 1500 K), we are ultimately interested in predicting the electronic conductivity at much lower temperatures corresponding to typical operating conditions—approximately 298 K. We assume that host-framework point-defects, i.e. those involving La, Zr, or O, formed during synthesis are “frozen in” during subsequent cooling to operating temperatures. The kinetic barriers for the reorganization of such defects within the host-framework are large, which prevents the system from fully re-equilibrating at low temperatures on experimentally relevant timescales [48]. Because LLZO is a fast-ion solid electrolyte, with highly-mobile lithium interstitials and vacancies, we do, however, expect V_{Li} and Li_i defects to re-equilibrate during cooling. Electron and hole populations are similarly expected to re-equilibrate on experimentally-relevant timescales [49, 50].

To obtain electron and hole carrier concentrations under operating conditions, as a function of initial synthesis conditions, we therefore first calculate self-consistent defect and charge-carrier concentrations for the relevant range of elemental chemical potentials at a characteristic synthesis temperature of 1500 K. We then fix the concentrations of all defects, except for V_{Li} and Li_i , and recompute “pseudo-equilibrium” defect and charge-carrier populations at a range of lower temperatures to predict how carrier concentrations change during sample cooling. For this second calculation, we impose the constraint that there is no lithium exchange with the surroundings during cooling, i.e., the net lithium stoichiometry is set by the high-temperature synthesis conditions.

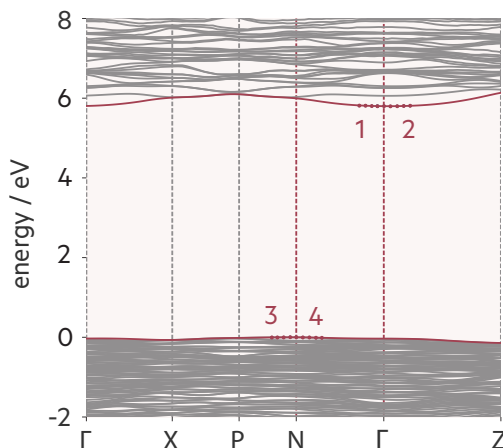
To illustrate the effect of varying synthesis conditions on the resulting carrier concentrations, we consider six chemical potential “limits”, which correspond to the vertices of the estimated synthetically-accessible chemical-potential space. These chemical-potential limits can be considered as two groups depending on whether they can be broadly characterised as O-rich/metal-poor or O-poor/metal-rich. Fig. 7.2 shows the calculated pseudo-equilibrium electron and hole carrier-concentrations as a function of the re-equilibration temperature, for each of these limits. For each set of synthesis conditions (elemental chemical potentials) we present data for undoped LLZO, with only intrinsic defects present, as well as for aliovalently-doped LLZO, where we introduce a concentration of 0.15 per formula unit of a generic supervalent dopant with relative charge $r = +2$. Defect transition level diagrams and respective self-consistently calculated Fermi energies are also plotted in Fig. 7.2.

Under O-rich/metal-poor conditions (Fig. 7.2; top row) we predict p -type conductivity (i.e. $[\text{h}^\bullet] > [e']$), but this can become slightly n -type when the system is cooled. In contrast, under O-poor/metal-rich conditions (Fig. 7.2; second row), we predict strong n -type behaviour.

The total number of charge carriers (summing both electrons and holes) under O-rich/metal-poor conditions, however, is smaller than under O-poor/metal-rich conditions. These low carrier concentrations are associated with a “mid-gap” Fermi energy: within the considered chemical potential space, the minimum calculated Fermi energy is 2.67 eV, and the maximum calculated Fermi energy is 3.78 eV (Fig. 7.2, bottom two rows) and the calculated band gap, aligned to the valence band maximum, ranges from 0 to 5.9 eV. Ultimately, we predict low room temperature carrier concentrations under all synthesis conditions and doping protocols.

7.4 Electronic conductivity

Figure 7.3: The electronic band structure of tetragonal LLZO calculated using HSE06, plotted along a high symmetry path in the Brillouin zone according to the Bradley and Cracknell notation [51]. The coloured points mark the band edges used to calculate the effective masses, with numeric labels indicating the corresponding entry in Table 7.1.



The electronic conductivity is given by the products of carrier concentrations and carrier mobilities summed over contributions from both electron and hole carriers (Eqn. 7.1). For the carrier mobilities, we are interested in these values under typical cell operating conditions, which we take as 298 K. Our model assumes that the carrier mobilities do not vary with changes in synthesis conditions or doping levels. The carrier mobilities therefore act as fixed scaling factors that can be used to convert carrier concentrations—which do vary according to synthesis conditions and doping levels—into electronic conductivities.

Table 7.1: Curvature effective masses, m^* , for holes and electrons determined by a parabolic fit to LLZO band edges [52], and the relevant crystallographic direction for transport. Numbers indicate the corresponding features in the electronic band structure (Fig. 7.3).

Carrier	Direction	m^*	No.
electron	$\Gamma \rightarrow \text{N}$	2.35	1
electron	$\Gamma \rightarrow \text{Z}$	2.41	2
hole	$\text{N} \rightarrow \text{P}$	2.39	3
hole	$\text{N} \rightarrow \Gamma$	21.44	4

To solve for polaron mobility we first determine the electron and hole effective masses. Carrier populations in wide-gap materials such as LLZO are low compared to conventional semiconductors, and we therefore calculate “curvature” effective-masses at the conduction band minimum

(CBM) and valence band maximum (VBM) [53]. The band-structure for tetragonal-LLZO is shown in Fig. 7.3, and the resulting curvature effective masses are given in Table 7.1. The lowest effective mass found for charge carriers in LLZO at the band edges is $2.35 m_e$. Using these data to calculate room-temperature carrier mobilities yields a maximum value (for both holes and electrons) of $0.2 \text{ cm}^2 \text{ V}^{-1} \text{ s}^{-1}$ [41].

The results above predict that under all considered synthesis conditions, carrier concentrations are relatively high at the initial synthesis temperature of 1500 K, but decrease by many orders of magnitude as the temperature is reduced under pseudo-equilibrium conditions. The significance of this decrease in carrier concentrations can be seen more clearly by plotting approximate electronic conductivities (via Eqn. 7.1) by scaling these predicted carrier concentrations by the previously calculated maximum room-temperature carrier mobility of $0.2 \text{ cm}^2 \text{ V}^{-1} \text{ s}^{-1}$. The resulting “room-temperature” intrinsic (undoped) and extrinsic (doped) electronic conductivities are plotted in Fig. 7.4 for both O-rich/metal-poor and O-poor/metal-rich conditions, as a function of the temperature at which the e^-/h^\bullet and $V_{\text{Li}}/\text{Li}_i$ populations re-equilibrate. In both cases, the high carrier concentrations for as-synthesised samples (1500 K) correspond to room-temperature electronic conductivities well in excess of the threshold values proposed by Han *et al.* For these high bulk electronic conductivities to be observed under operating conditions, however, would require that the electron and hole carrier populations do not re-equilibrate during, or after, sample cooling. Re-equilibration of the electron and hole carrier populations (and the lithium vacancy and interstitial populations), however, greatly reduces the carrier concentrations (Fig. 7.2) and the corresponding room-temperature electronic conductivities are predicted to be well below the threshold values proposed for intrinsic bulk lithium-dendrite growth.

7.5 Summary and Discussion

Minimising the electronic conductivity of lithium solid electrolytes is crucial to the effective operation of a solid state battery. In recent years, non-negligible electronic conductivity has been linked to lithium-dendrite growth in lithium solid electrolytes, leading to cell failure [1, 25]. This raises the question of whether the intrinsic electronic conductivity of various solid state electrolytes makes them fundamentally incompatible with a lithium metal anode. Motivated by this proposal, and to provide an estimate of the room-temperature bulk electronic conductivities of lithium-garnet solid electrolytes, we calculate the electronic conductivity of the lithium-conducting solid electrolyte LLZO, as a function of synthesis conditions and doping protocol.

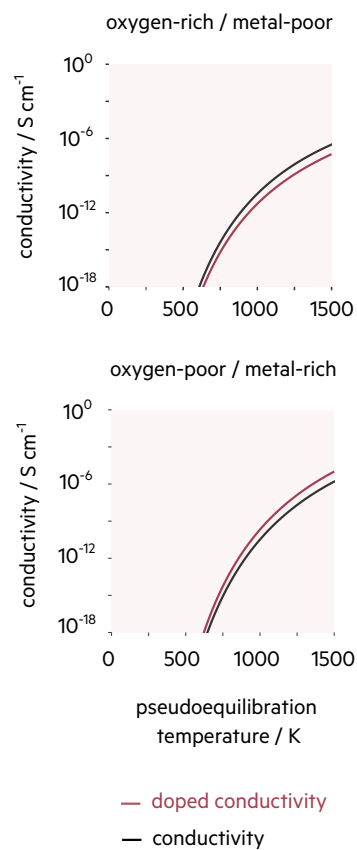


Figure 7.4: Effective “room temperature” (298 K) electronic conductivities for LLZO synthesised under O-rich/metal-poor (top panel) and O-poor/metal-rich (bottom panel) conditions, as a function of $\{V_{\text{Li}}, \text{Li}_i\}$ and $\{e^-/h^\bullet\}$ pseudo-equilibration temperature. Conductivities are calculated via Eqn. 7.1), using the electronic carrier concentrations in Fig. 7.2 and the previously calculated maximum room-temperature electron and hole carrier mobilities of $0.2 \text{ cm}^2 \text{ V}^{-1} \text{ s}^{-1}$. Solid lines show results for undoped LLZO, and dashed lines show results under supervalent doping with M^{2+} at a concentration of 0.15 per formula unit.

We find that electronic carriers have low mobilities ($<1 \text{ cm}^2 \text{ V}^{-1} \text{ s}^{-1}$) owing to large hole and electron effective masses and strong electron-phonon interactions. While the electronic carrier populations predicted under typical synthesis conditions ($\sim 1500 \text{ K}$) are sufficiently high that the corresponding room-temperature electronic conductivities would be well in excess of the threshold values proposed by Han *et al.*, these electronic carrier populations decrease significantly under subsequent sample cooling. At room-temperature, assuming full re-equilibration of e'/h^\bullet carriers (and $V_{\text{Li}}/\text{Li}_i$ defects), carrier concentrations are predicted to be negligible, giving room-temperature electronic conductivities that are well below the threshold values of Han *et al.* This result is consistent with recent experimental data that gave a much lower electronic conductivity for single-crystal samples of LLZO than previously reported for polycrystalline samples [3]. We note, however, that in experimental samples there may be additional contributions to electronic conductivity from electronic charge carriers that are thermally excited at high temperature (e.g., directly after synthesis) and then kinetically trapped during cooling, to give non-equilibrium carrier populations with higher electronic conductivities than we predict here.

In the context of understanding the possible contribution of electronic conductivity to dendrite nucleation and growth, one limitation of the present study is that it considers only *bulk* properties. Real-world solid electrolytes possess surfaces and (typically) grain boundary interfaces, which may contribute to net electronic conductivities or otherwise promote lithium-dendrite growth. Previous theoretical work has observed dramatic band-gap reductions at LLZO surfaces ($E_g^{\text{bulk}} = 5.46 \text{ eV}$, $E_g^{\text{surface}} = 2.19 \text{ eV}$) [29] and a recent combined experimental and theoretical study predicts similar narrowing at grain boundaries ($E_g^{\text{bulk}} = 6 \text{ eV}$, $E_g^{\text{gb}} = 1 \text{ to } 3 \text{ eV}$) [6]. Such band-gap narrowing is expected to greatly increase the number of free charge-carriers at thermal equilibrium (cf. Equations (7.2) and (7.3)), potentially giving high local electronic conductivities that may facilitate dendrite nucleation and growth. Grain boundaries and surfaces may also exhibit non-bulk defect populations. Local variations in defect standard chemical potentials can drive defect segregation to (or from) these regions, causing local shifts in the electrostatic potential (band bending) and increasing (or decreasing) local free carrier populations relative to the bulk [54, 55]. Lithium nucleation has been observed at grain boundaries in LLZO in recent experimental studies [6, 26], which illustrates the likely critical role of sample morphology on dendrite growth in lithium garnets, and underscores the need for the development of new theoretical methods that can accurately model equilibrium defect and free carrier populations at interfaces, such as grain boundaries and surfaces.

Bibliography

- (1) Han, F.; Westover, A. S.; Yue, J.; Fan, X.; Wang, F.; Chi, M.; Leonard, D. N.; Dudney, N. J.; Wang, H.; Wang, C. *Nat. Energy* **2019**, *4*, 187–196.
- (2) Buckeridge, J. *Comput. Phys. Commun.* **2019**, *244*, 329–342.
- (3) Philipp, M.; Gadermaier, B.; Posch, P.; Hanzu, I.; Ganschow, S.; Meven, M.; Rettenwander, D.; Redhammer, G. J.; Wilkening, H. M. R. *Adv. Mater. Inter.* **2020**, 2000450.
- (4) Lotsch, B. V.; Maier, J. J. *Electroceram.* **2017**, *38*, 128–141.
- (5) Gorai, P.; Famprakis, T.; Singh, B.; Stevanović, V.; Canepa, P. *Chem. Mater.* **2021**, *33*, 7484–7498.
- (6) Liu, X.; Garcia-Mendez, R.; Lupini, A. R.; Cheng, Y.; Hood, Z. D.; Han, F.; Sharafi, A.; Idrobo, J. C.; Dudney, N. J.; Wang, C.; Ma, C.; Sakamoto, J.; Chi, M. *Nat. Mater.* **2021**, 1–6.
- (7) Burbano, M.; Carlier, D.; Boucher, F.; Morgan, B. J.; Salanne, M. *Phys. Rev. Lett.* **2016**, *116*, 135901–6.
- (8) He, X.; Zhu, Y.; Mo, Y. *Nature Comm.* **2017**, *8*, 15893.
- (9) Kraft, M. A.; Culver, S. P.; Calderon, M.; Böcher, F.; Krauskopf, T.; Senyshyn, A.; Dietrich, C.; Zevalkink, A.; Janek, J.; Zeier, W. G. *J. Am. Chem. Soc.* **2017**, *139*, 10909–10918.
- (10) Stefano, D. D.; Miglio, A.; Robeyns, K.; Filinchuk, Y.; Lechartier, M.; Senyshyn, A.; Ishida, H.; Spannenberger, S.; Prutsch, D.; Lunghammer, S.; Rettenwander, D.; Wilkening, M.; Roling, B.; Kato, Y.; Hautier, G. *Chem* **2019**, *5*, 2450–2460.
- (11) Culver, S. P.; Squires, A. G.; Minafra, N.; Armstrong, C. W. F.; Krauskopf, T.; Böcher, F.; Li, C.; Morgan, B. J.; Zeier, W. G. *J. Am. Chem. Soc.* **2020**, *142*, 21210–21219.
- (12) Morgan, B. J. *Chem. Mater.* **2021**, *33*, 2004–2018.
- (13) Zhang, Y.; He, X.; Chen, Z.; Bai, Q.; Nolan, A. M.; Roberts, C. A.; Banerjee, D.; Matsunaga, T.; Mo, Y.; Ling, C. *Nature Comm.* **2019**, *10*, 1–7.
- (14) Kahle, L.; Marcolongo, A.; Marzari, N. *Energy Environ. Sci.* **2020**, *13*, 928–948.
- (15) Muy, S.; Voss, J.; Schlem, R.; Koerver, R.; Sedlmaier, S. J.; Maglia, F.; Lamp, P.; Zeier, W. G.; Shao-Horn, Y. *iScience* **2019**, *16*, 270–282.
- (16) Sendek, A. D.; Cubuk, E. D.; Antoniuk, E. R.; Cheon, G.; Cui, Y.; Reed, E. J. *Chem. Mater.* **2018**, *31*, 342–352.

- (17) Morscher, A.; Dyer, M. S.; Duff, B. B.; Han, G.; Gamon, J.; Daniels, L. M.; Dang, Y.; Surta, T. W.; Robertson, C. M.; Blanc, F.; Claridge, J. B.; Rosseinsky, M. J. *Chem. Mater.* **2021**, *33*, 2206–2217.
- (18) Richards, W. D.; Miara, L. J.; Wang, Y.; Kim, J. C.; Ceder, G. *Chem. Mater.* **2015**, *28*, 266–273.
- (19) Monroe, C.; Newman, J. J. *Electrochem. Soc.* **2005**, 152.
- (20) Janek, J.; Zeier, W. G. *Nat. Energy* **2016**, *1*, 1–4.
- (21) Famprikis, T.; Canepa, P.; Dawson, J. A.; Islam, M. S.; Masquelier, C. *Nat. Mater.* **2019**, *21*, 1–14.
- (22) Ohno, S. et al. *ACS Energy Lett.* **2020**, *5*, 910–915.
- (23) Ohno, S.; Banik, A.; Dewald, G. F.; Kraft, M. A.; Krauskopf, T.; Minafra, N.; Till, P.; Weiss, M.; Zeier, W. G. *Prog. Energy* **2020**, *2*, 022001–36.
- (24) Banik, A.; Famprikis, T.; Ghidui, M.; Ohno, S.; Kraft, M. A.; Zeier, W. G. *Chem.* **2021**, *12*, 6238–6263.
- (25) Aguesse, F.; Manalastas, W.; Buannic, L.; Lopez del Amo, J. M.; Singh, G.; Llordés, A.; Kilner, J. *ACS Appl. Mater. & Inter.* **2017**, *9*, 3808–3816.
- (26) Song, Y.; Yang, L.; Zhao, W.; Wang, Z.; Zhao, Y.; Wang, Z.; Zhao, Q.; Liu, H.; Pan, F. *Adv. Energy Mater.* **2019**, *9*, 1900671.
- (27) Jonghe, L. C. D.; Feldman, L.; Buechele, A. *Solid State Ion.* **1981**, *5*, 267–269.
- (28) Jonghe, L. C. D.; Feldman, L.; Beuchele, A. *J. Mater. Sci.* **1981**, *16*, 780–786.
- (29) Tian, H.-K.; Liu, Z.; Ji, Y.; Chen *Chem. Mater.* **2019**, *31*, 7351–7359.
- (30) Gorai, P.; Famprikis, T.; Singh, B.; Stevanović, V.; Canepa, P. *Chem. Mater.* **2021**, Just Accepted.
- (31) Scanlon, D. O.; Kehoe, A. B.; Watson, G. W.; Jones, M. O.; David, W. I. F.; Payne, D. J.; Egdell, R. G.; Edwards, P. P.; Walsh, A. *Phys. Rev. Lett.* **2011**, *107*, 246402.
- (32) Scanlon, D. O.; King, P. D. C.; Singh, R. P.; de la Torre, A.; Walker, S. M.; Balakrishnan, G.; Baumberger, F.; Catlow, C. R. A. *Adv. Mater.* **2012**, *24*, 2154–2158.
- (33) Kittel, C., *Thermal Physics*; W. H. Freeman: San Francisco, 1980.
- (34) Ashcroft, N., *Solid State Physics*; Cengage Learning: Andover England, 1976.
- (35) Zhang, S. B.; Northrup, J. E. *Phys. Rev. Lett.* **1991**, *67*, 2339–2342.

- (36) Buckeridge, J. *Comp. Phys. Commun.* **2019**, *244*, 329–342.
- (37) Squires, A. G.; Scanlon, D. O.; Morgan, B. J. *Chem. Mater.* **2020**, *32*, 1876–1886.
- (38) Yu, P. Y.; Cardona, M., *Fundamentals of Semiconductors*; Springer Berlin Heidelberg: 2010.
- (39) Franchini, C.; Reticcioli, M.; Setvin, M.; Diebold, U. *Nat. Rev. Mater.* **2021**, *6*, 560–586.
- (40) Peeters, F. M.; Devreese, J. T. In *Solid State Physics*, Ehrenreich, H., Turnbull, D., Seitz, F., Eds.; Academic Press: 1984; Vol. 38, pp 81–133.
- (41) Frost, J. M. *Phys. Rev. B* **2017**, *96*, 195202.
- (42) Feynman, R. P. *Phys. Rev.* **1955**, *97*, 660–665.
- (43) Fröhlich, H. *Proc. R. Soc. Lond. A Math. Phys. Sci.* **1952**, *215*, 291–298.
- (44) Frost, J. M. *J. Open Source Softw.* **2018**, *3*, 566.
- (45) CRC Handbook, *CRC Handbook of Chemistry and Physics, 88th Edition*, 88th ed.; CRC Press: 2007.
- (46) Finnis, M.; Lozovoi, A.; Alavi, A. *Annu. Rev. Mater. Res.* **2005**, *35*, 167–207.
- (47) Thangadurai, V.; Narayanan, S.; Pinzaru, D. *Chem. Soc. Rev.* **2014**, *43*, 4714.
- (48) Sasaki, K.; Maier, J. *J. Appl. Phys.* **1999**, *86*, 5422–5433.
- (49) Maier, J. *Phys. Chem. Chem. Phys.* **2003**, *5*, 2164–2173.
- (50) Canepa, P.; Gautam, G. S.; Broberg, D.; Bo, S.-H.; Ceder, G. *Chem. Mater.* **2017**, *29*, 9657–9667.
- (51) Bradley, C. J., *The mathematical theory of symmetry in solids : representation theory for point groups and space groups*; Clarendon Press: Oxford New York, 2010.
- (52) Whalley, L. D. *J. Open Source Soft.* **2018**, *3*, 797.
- (53) Whalley, L. D.; Frost, J. M.; Morgan, B. J.; Walsh, A. *Phys. Rev. B* **2019**, *99*, 085207.
- (54) Dean, J. M.; Coles, S. W.; Saunders, W. R.; McCluskey, A. R.; Wolf, M. J.; Walker, A. B.; Morgan, B. J. *arXiv* **2021**, 2104.00623.
- (55) Swift, M. W.; Swift, J. W.; Qi, Y. *Nature Comp. Sci.* **2021**, *1*, 212–220.

Evidence for an inductive effect in the lithium solid electrolyte LGPS on isovalent doping

Statement of Authorship

The following chapter concerns the article entitled **Evidence for a Solid-Electrolyte Inductive Effect in the Superionic Conductor $\text{Li}_{10}\text{Ge}_{1-x}\text{Sn}_x\text{P}_2\text{S}_{12}$** published in the Journal of the American Chemical Society (*J. Am. Chem. Soc.* 2020 142 (50), 21210-21219).

This paper reports on original research I conducted during the period of my Higher Degree by Research candidature.

Personal contributions: It should be noted that these percentages only account for the computational aspect of this study, the related experimental work was carried out by the group of Prof. Wolfgang Zeier. Formulation of ideas (70%): I have been heavily involved with all decisive stages of development of the project with guidance from Dr Benjamin Morgan on the motivation for the work, after the model was originally proposed by Prof. Wolfgang Zeier with input from Dr Morgan. Design of methodology (80%): After carrying out the Bader calculations proposed by Dr Benjamin Morgan, all further methodological decision were taken by myself. I designed the individual calculations and wrote bespoke post-processing code to analyse the results with input on best practice from Dr Benjamin Morgan. Experimental work (90%): Callum Armstrong carried out some preliminary Bader calculations on $\text{Li}_{10}\text{GeP}_2\text{S}_{12}$ and $\text{Li}_{10}\text{SnP}_2\text{S}_{12}$, beyond that, I carried out all other practical aspects of the work. Presentation of data in journal format (60%): The first drafts of the computational methodology and results section were written by me, with input from Dr Benjamin Morgan. The finalised manuscript was prepared by Dr Benjamin Morgan, Prof. Wolfgang Zeier, Nicolò Minafra and myself with input from all co-authors. I then re-contextualised the computational work

for inclusion in this dissertation.

Reproduced in part with permission from *J. Am. Chem. Soc.* 2020 142 (50), 21210-21219. Copyright 2020 American Chemical Society.

Signed:



Date:

15 / 3 / 22

Context

This chapter represents a departure from the other results chapters in this thesis. In this instance, rather than focus on the changing concentrations of defects (and electrons and holes) in response to doping, we consider how defect mobilities change. We do this for the lithium ions in the solid-electrolyte LGPS and investigate how isovalent doping of $\text{Ge}^{4+} \rightarrow \text{Sn}^{4+}$ affects lithium ion mobility via a possible solid-electrolyte “inductive effect”. A key point of difference between this results chapter and the others are that here we look at defect properties of a disordered material. When considering the mobile-ion host-framework properties of LGPS, such as the bonding interactions between Ge/Sn and S ions, we use a pseudo-ordered structure taken from the Materials Project [1] and assume the arrangement of lithium ions will not influence these properties significantly. When dealing with how doping may influence lithium-ion mobility directly we take two different approaches. For the case of how local lithium vacancy formation energies change depending on their distance from dopant ions, we enumerate many possible orderings and calculate lithium vacancy formation energies in these structures. In the case of the NEB calculations used to directly probe lithium-ion mobility, we take only one example structure for each of $\text{Li}_{10}\text{SnP}_2\text{S}_{12}$ and $\text{Li}_{10}\text{GeP}_2\text{S}_{12}$ and calculate the barriers for lithium hopping away from both a Ge^{4+} ion bonded to a S^{2-} ion, and an Sn^{4+} ion bonded to a S^{2-} ion. As this represents a minute fraction of all possible lithium-ion orderings, this should be taken as merely an indication of how dopants may modulate the barrier for lithium-ion hopping.

The work presented in this chapter follows the same structure as the associated paper (see statement of authorship), however, it has been abridged to better reflect the overall narrative of this dissertation. Additionally, the associated paper is the product of a collaboration with an

experimental group, however I felt that the computational work alone presents a full argument for the existence of an experimentally relevant inductive effect in Sn-doped LGPS. To reflect this, and as the rest of this thesis is concerned exclusively with computational modelling, the experimental parts of the associated paper were removed.

8.1 Introduction

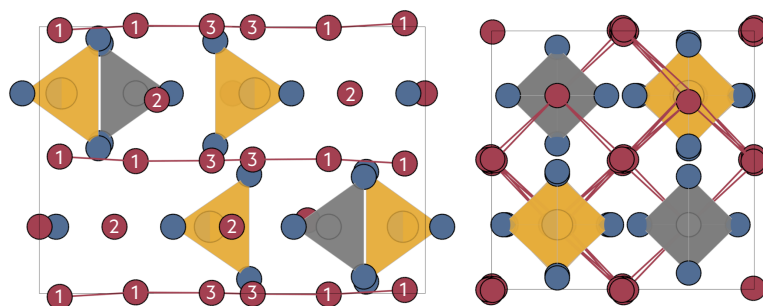


Figure 8.1: **Left** LGPS unit cell oriented along the b -axis. Lithium ions are shown in red, sulphur in blue. GeS_4/PS_4 tetrahedra in yellow, and PS_4 tetrahedra in grey. The red line connects the lithium ions along the “main” diffusion channel which is formed of lithium 1 and lithium 3 sites with the lithium between channels designated as lithium 2. **Right**, the same cell oriented down the c -axis where the red lines show the connectivity between the main lithium diffusion channels.

The lithium solid electrolyte $\text{Li}_{10}\text{GeP}_2\text{S}_{12}$ (LGPS) and its derivatives are of great interest to the battery materials community [1–6], their room-temperature ionic conductivities have been reported in excess of 0.01 S cm^{-1} which places them as some of the highest conductivity lithium ion solid electrolytes discovered to date [7]. Unravelling the factors that control ionic-transport in these materials is a key research question, because such an understanding can inform the development of general “design rules” for property-optimisation, additionally, lessons-learned from one material can often be mapped onto other materials, aiding in the identification and optimization of new fast-ion conducting materials [8–10], thereby broadening the pool of candidate solid electrolytes for future solid-state battery applications. A partial answer to the question of what makes some solid electrolytes much faster ionic conductors than others comes from an understanding of favorable structural motifs. Families of structurally related solid electrolytes, however, often exhibit room temperature ionic conductivities that vary by several orders of magnitude, highlighting the important role of chemical composition as a factor in understanding ionic conductivity trends between similar solid electrolytes [10–14].

$\text{Li}_{10}\text{GeP}_2\text{S}_{12}$ adopts a tetragonal structure consisting of a framework of GeS_4^{4-} and PS_4^{3-} tetrahedra that accommodate a percolating network of lithium ions. The structure has open channels oriented along the c -axis (fig. 8.1) that enable lithium diffusion. These c -oriented channels are connected by cross-linked lithium sites that allow slower diffusion in the

a - b plane (fig. 8.1) [15]. The dominant lithium diffusion process along c consists of lithium ions moving through alternating Li(1) and Li(3) sites [15]. The potential-energy profile for lithium diffusion between these sites is determined by both the electrostatic interactions between lithium ions and by the interactions between the mobile lithium ions and the host-framework [16]. Introducing dopants can affect both the geometry and charge-density-distribution of the host-framework and both effects may modulate the lithium-ion potential-energy profile, resulting in either increased or decreased lithium-ion conductivity [17].

Doping within a solid-electrolyte host-framework is a well-established strategy for enhancing the ionic conductivities of specific solid-electrolytes [2]. The selection of potentially beneficial framework-atom substitutions is often guided by considering geometric models that aim to predict how particular substitutions might affect the structure of the host-framework. One such model, for example, considers the increase in crystal volume that occurs when replacing small framework atoms with larger substitute species. The resulting framework expansion is expected to increase the interstitial volume available to diffusing lithium, thereby promoting lithium conduction [18]. An alternative model considers how substitution of specific framework atoms might affect the local geometry along critical lithium diffusion pathways, causing an expansion or contraction of rate-limiting “bottlenecks” and thereby promoting or impeding lithium diffusion respectively [17]. Geometric models such as these often provide intuitive explanations for the conductivity trends observed within families of solid electrolytes. In some notable cases, however, observed conductivity trends run counter to those predicted on geometric grounds: chemical substitutions that would be expected to increase lithium-ion conductivities instead give the opposite effect and decrease ionic conductivities. One example of this contrary behavior is the isovalent doping of germanium with the larger and more polarisable tin within the $\text{Li}_{10}\text{Ge}_x\text{Sn}_{1-x}\text{P}_2\text{S}_{12}$ system, which was initially expected to produce an increased ionic conductivity due to an increase in overall lattice volume, but in practice gives the opposite trend, with increasing tin content giving a decreased lithium-ion conductivity [4, 17].

Krauskopf et al. have recently suggested that this “inverted” response to chemical substitution might be explained by a so-called solid-electrolyte “inductive effect” [17]. This model predicts that the lower electronegativity of tin versus germanium causes Sn-S bonds to be more polar than equivalent Ge-S bonds, with tin-bonded sulphur atoms therefore having greater associated negative charge-density than the equivalent germanium-bonded sulphur atoms. This increased negative charge for SnS_4 sulfur atoms compared to GeS_4 sulfur atoms means that the electrostatic inter-

action between these sulfur atoms and nearby lithium ions is stronger in the tin-substituted system than in the germanium analogue. This increases the effective potential-energy barrier for lithium diffusion along the Li(3)–Li(1) channels resulting in a reduced lithium-ion conductivity. The proposed inductive effect is illustrated schematically in Figure 8.2.

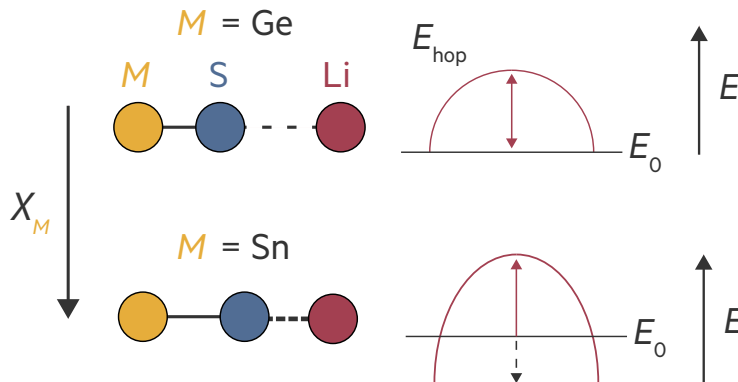


Figure 8.2: Schematic of the predicted difference in M -S...Li bonding for $M = \text{Ge}$ vs $M = \text{Sn}$ due to a hypothetical inductive effect. Changes in the M -S bonding modulate the Coulombic interaction between S and adjacent Li^+ ions. A less electronegative cation, M creates a more polar M -S bond, leaving more charge density on the sulphur ion, strengthening the electrostatic interaction between the sulphur and lithium ions producing an increased potential energy barrier for lithium diffusion.

Together with the proposal by Krauskopf *et al.* that an inductive effect might explain the observed lithium conductivity trend in $\text{Li}_{10}\text{MP}_2\text{S}_{12}$, solid-electrolyte inductive effects have been invoked to explain anomalous conductivity trends in a number of other systems, including $\text{Na}_{11}\text{Sn}_2\text{PnS}_{12}$ ($\text{Pn} = \text{P}, \text{Sb}$) [12], $\text{Na}_3\text{P}_{1-x}\text{As}_x\text{S}_4$ [19], $\text{Li}_{4-x}\text{Sn}_{1-x}\text{Sb}_x\text{S}_4$ [20], and $\text{LiM}_2(\text{PO}_4)_3$ ($M = \text{Zr}, \text{Sn}$) [21]. The inductive-effect model is founded on simple chemical-bonding concepts, making it an appealing for explaining these unexpected conductivity trends. Yet there is no direct evidence that such an inductive effect can be expected to have an observable impact on lithium-ion diffusion. More specifically, it is not known to what extent varying the electronegativities of host-framework atoms within a solid electrolyte can affect either the intra-framework bonding interactions or the electrostatic interactions between the host framework and the mobile ions; nor is it clear whether such effects, if present, can modify the potential energy surface for lithium ion transport sufficiently to explain observed trends in experimental solid-electrolyte conductivities.

Motivated by the question of whether the solid-electrolyte inductive effect does indeed exist, or rather, should be expected to have a meaningful impact on lithium ion transport in solid electrolytes, we have performed a computational study of the $\text{Li}_{10}\text{Ge}_{1-x}\text{Sn}_x\text{P}_2\text{S}_{12}$ system. We note a series of subtle electronic changes produced by $\text{Ge}^{4+} \rightarrow \text{Sn}^{4+}$ substitution that are consistent with the model proposed by Krauskopf *et al.*: COOP/COHP and Bader analysis show that the inclusion of lower-electronegativity tin

produces weaker (more polar) M -S bonds within the MS_4^{4-} tetrahedra, calculated lithium-binding energies provide further complementary evidence that tin-substitution increases the strength of the S^{2-} - Li^+ interactions. We also show that these changes in M -S bonding and S^{2-} - Li^+ interactions are coupled to a modulation of the Li^+ potential-energy profile along the Li(3)-Li(1) diffusion pathway in the main diffusion channels: substituting Ge^{4+} for Sn^{4+} gives a higher potential-energy maximum for single-lithium-ion motion. Further calculations for the tin substituted system, but with a fixed geometry corresponding to the germanium substituted analogue, show that tin substitution increases the height of the lithium diffusion profile even in the absence of changes in host-framework geometry, providing further evidence for an electronic inductive effect.

When considered together, these results provide evidence in support of a solid-electrolyte inductive effect in the $Li_{10}Ge_xSn_{1-x}P_2S_{12}$ system. These data also illustrate how information about subtle changes in host-framework bonding and framework-mobile-ion interactions arising from framework-atom doping can be obtained through computational techniques, and how this may provide a clearer understanding of the chemical effects responsible for modulating ionic conductivities in families of structurally-similar lithium-ion solid electrolytes.

8.2 Methods

DFT calculations were carried out with valence electron configurations of Li [$2s^1$], Ge [$4s^24p^2$], Sn [$5s^25p^2$], P [$3s^23p^3$], and S [$3s^23p^4$]. All calculations used the GGA functional PBEsol [22]. Calculations with a fixed cell volume used a plane-wave cutoff of 500 eV, while calculations with a variable cell volume used an increased cutoff of 650 eV to minimise errors arising due to Pulay stress. Geometry optimizations were deemed converged when all atomic forces were smaller than 0.01 eV \AA^{-1} . All calculations were spin-polarized and used a Monkhorst-Pack grid for sampling \mathbf{k} -space, with the minimum spacing between \mathbf{k} -points set to 0.3^{-1} .

To quantify charge distributions and bonding characters from our DFT calculations, we assign net atomic-charges, calculated using the Bader charge-partitioning methodology [23] as implemented by Henkelman *et al.* [24]; additionally we calculate COOPs and COHPs using the LOBSTER code [25–27]. Within LOBSTER, the *vaspfitpbe2015* basis functions were used to map the plane-wave basis-set onto local orbitals. To sample single-lithium-ion diffusion potential-energy profiles along the c channels, we performed climbing-image nudged-elastic-band (CI-NEB) [28] calculations, using the pathfinder algorithm of Rong *et al.* [29] to obtain an initial approximation of each minimum-energy-barrier path.

To estimate changes in the S–Li interaction for $M = \text{Sn, Ge}$, we calculated “vertical” (unrelaxed) Li^+ vacancy formation energies ($\Delta E_f^{V_{\text{Li}}}$) for all lithium atoms as a function of nearest-neighbor S–Li distance, with reference to the sulphur atoms that constitute the vertices of the SnS_4^{4-} tetrahedra. The Li^+ vacancy formation energies, were calculated as

$$\Delta E_f^{V_{\text{Li}}} = \Delta E^{V_{\text{Li}}} + \mu_{\text{Li}} - E_{\text{Fermi}} \quad (8.1)$$

where $\Delta E^{V_{\text{Li}}}$ is given by the difference in energy between a stoichiometric defect-free supercell and an equivalent cell containing a single Li^+ vacancy, with all other atoms held fixed in place.¹

Calculations of formation energies of charged defects using periodic models, as for the lithium vacancy considered here, typically include an image-charge energy term (E_{icc}) [30, 31], to correct for a shift in total energy due to the artificial interaction of a defect with its periodic images. This correction requires calculation of the dielectric tensor, which is ill-defined within a DFT framework for an intrinsically disordered system such as LGPS. For the results presented here, we do not include an explicit image-charge correction, and instead attempt to minimize the variation in the neglected correction term—which scales approximately as L^{-3} , where L is the length of the simulation cell [32]—by performing our defect calculations in large 400 atom $2 \times 2 \times 2$ LGPS supercells. We have estimated the magnitude of the (neglected) image-charge correction term by performing an explicit calculation for a V_{Li}' vacancy in a pseudo-ordered structure of $\text{Li}_{10}\text{GeP}_2\text{S}_{12}$ taken from the Materials Project, [33] using the approach of Lany and Zunger adapted for anisotropic systems by Murphy and Hine, [30, 31] which gives a representative value of $E_{\text{icc}} = 0.05$ eV.

Because $\text{Li}_{10}\text{GeP}_2\text{S}_{12}$ is intrinsically lithium-disordered, the S–Li interaction may not be well characterized by considering a single lithium-vacancy formation-energy. To account for this lithium disorder, we have sampled the distribution of vacancy–formation-energies as a function of (M)S–Li distance from a set of 160 lithium configurations. These representative 160 configurations were selected from an initial set of 500,000 structures, with candidate structures selected by ranking their approximate electrostatic energies, using the Ewald summation functionality in the PYMATGEN python package [34].

8.3 Bond-strength indicators and changing M –S bonding interactions

To explore how the choice of $M = \{\text{Ge, Sn}\}$ affects the M –S bonding character, we have calculated iCOOPs and iCOHPs for the M –S bonds in $\text{Li}_{10}\text{Ge}_{0.5}\text{Sn}_{0.5}\text{P}_2\text{S}_{12}$. The iCOOP values plotted in fig. 8.3, left, show an

¹ This is a truncated form of Equation (4.25) (the equation for the formation energy of defect X in charge state q). In this instance, we are not interested in how the formation energy of the defect changes with respect to chemical potential. We are comparing the formation energy of defects which all consist of the removal of a single lithium atom: proper consideration of the lithium chemical potential will change the absolute energy of the formation of these defects, but the relative difference between them will remain the same.

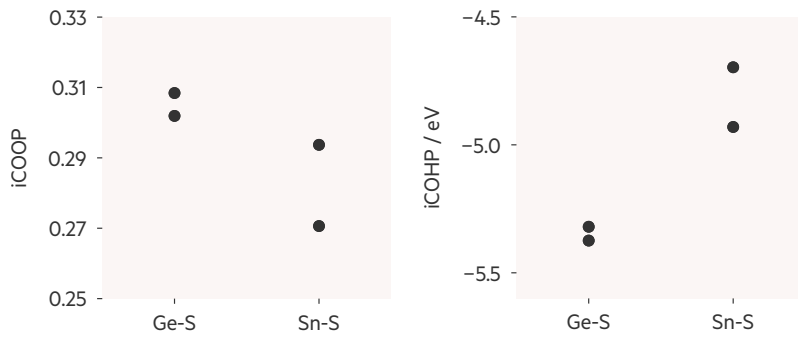
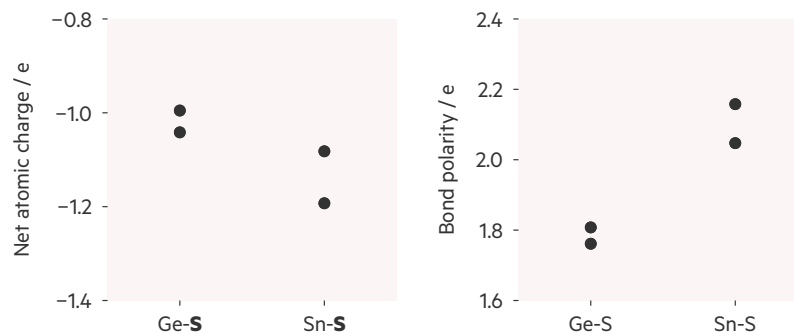


Figure 8.3: **Left**, iCOOP values computed for M -S bonds in $\text{Li}_{10}\text{Ge}_{0.5}\text{Sn}_{0.5}\text{P}_2\text{S}_{12}$, **Right**, iCOHP values computed for M -S bonds in $\text{Li}_{10}\text{Ge}_{0.5}\text{Sn}_{0.5}\text{P}_2\text{S}_{12}$.

increased orbital overlap between the Ge-S bonds relative to the Sn-S, correlated with a more negative iCOHP value in the more “covalent” Ge-S bond. The iCOHP values are plotted in Figure 8.3, right, and are indicative of bonding strength within the respective MS_4 tetrahedra: more negative values indicate stronger and more-covalent bonding, while more positive values indicate weaker and more polar bonding [25–27]. The more negative values obtained for the GeS_4^{4-} tetrahedra compared to the SnS_4^{4-} tetrahedra suggest stronger bonding interactions for these Ge-S bonds compared to the equivalent Sn-S bonds.

Figure 8.4: **Left**, net atomic charges computed for S atoms bonded to M atoms in both $\text{Li}_{10}\text{GeP}_2\text{S}_{12}$ and $\text{Li}_{10}\text{SnP}_2\text{S}_{12}$. **Right**, net atomic charge “bond polarity” (difference) computed for M -S atoms bonded to M atoms in both $\text{Li}_{10}\text{GeP}_2\text{S}_{12}$ and $\text{Li}_{10}\text{SnP}_2\text{S}_{12}$.



To investigate whether these changes in bond-strength are coupled to a measurable change in the charge density associated with the M -bonded S^{2-} ions, we have also calculated net atomic-charges for the $\text{Li}_{10}\text{GeP}_2\text{S}_{12}$ and $\text{Li}_{10}\text{SnP}_2\text{S}_{12}$ end-members (Figure 8.4, left). This analysis assigns larger more-negative charges to tin-bonded S^{2-} ions in $\text{Li}_{10}\text{SnP}_2\text{S}_{12}$ than to equivalent germanium-bonded S^{2-} ions in $\text{Li}_{10}\text{GeP}_2\text{S}_{12}$. To quantify the M -S bond polarity in $\text{Li}_{10}\text{GeP}_2\text{S}_{12}$ and $\text{Li}_{10}\text{SnP}_2\text{S}_{12}$, we computed the differences in net atomic-charge values between the germanium or tin ions and their coordinating S^{2-} ions (Figure 8.4, right). We again find a subtle but clear difference in bonding character between these two end-members, with the Ge-S bonds in $\text{Li}_{10}\text{GeP}_2\text{S}_{12}$ being less polar in character than the Sn-S bonds in $\text{Li}_{10}\text{SnP}_2\text{S}_{12}$, i.e., the difference in net

atomic charges between M and S when $M = \text{Sn}$ is greater than when $M = \text{Ge}$.

These bond-strength indicators and bond polarity data together give a coherent picture of how substituting tin for germanium in $\text{Li}_{10}\text{MP}_2\text{S}_{12}$ affects the M - S bonding. Ge-S bonding is stronger and less polar than Sn-S bonding and germanium bonded sulphur atoms in $\text{Li}_{10}\text{GeP}_2\text{S}_{12}$ have smaller (less negative) associated charges than tin-bonded sulphur atoms in $\text{Li}_{10}\text{SnP}_2\text{S}_{12}$. Each of these observations is consistent with the predictions of the inductive effect model.

8.4 Ge \rightarrow Sn substitution effects on the Li-ion potential energy surface.

To corroborate the stabilizing effect of tin-substitution on nearby Li^+ , we performed a further series of DFT calculations in which we computed the Li^+ vacancy-formation energies ($\Delta E_f^{V_f}$) for a set of $\text{Li}_{10}\text{GeP}_2\text{S}_{12}$ supercells each containing one tin ion. These Li^+ vacancy-formation energies give a relative measure of the “binding energy” of Li^+ at different positions within each supercell; a larger vacancy-formation energy corresponds to a more stable Li^+ position. Figure 6a shows the resulting distributions of calculated Li^+ vacancy-formation energies, classified according to whether the Li^+ ion removed is originally located less than 3 \AA of a tin-bonded sulphur ion or not. The vacancy-formation-energies for Li^+ ions close to tin-bonded sulphur atoms are shifted to higher energies relative to the vacancy-formation-energies for Li^+ ions that sit further away, i.e. there is a greater energy cost to remove lithium ions from Sn- S -adjacent positions.

The enhanced binding of Li^+ ions near Sn- S is expected to correspond to a modulation of the potential energy profile for Li^+ ions moving within these c -oriented diffusion channels. To better quantify the effect of germanium-tin substitution on the Li^+ ion potential-energy profile along the $\text{Li}(3)$ - $\text{Li}(1)$ diffusion channels, we consider potential energy profiles obtained from a series climbing-image nudged elastic band (CI-NEB) calculations for a single Li^+ ion moving from the $\text{Li}(3)$ site to the $\text{Li}(1)$ site. Li diffusion in $\text{Li}_{10}\text{GeP}_2\text{S}_{12}$ proceeds by the concerted string-like motion of groups of lithium ions [35], and NEB pathways for individual lithium ions therefore should not be equated with the true microscopic free-energy-barrier for lithium motion (which determines the activation energy for Li^+ conduction). In this case, however, we are interested in local differences in the potential energy surfaces as a function of Ge \rightarrow Sn substitution, and we consider these single- Li^+ NEB barriers as a proxy metric for the “roughness” of the true many-body potential-energy surface. The CI-NEB profiles for Li^+ diffusion in $\text{Li}_{10}\text{GeP}_2\text{S}_{12}$ and in $\text{Li}_{10}\text{SnP}_2\text{S}_{12}$ are shown in Figure 8.6, left panel. These profiles were computed following the stan-

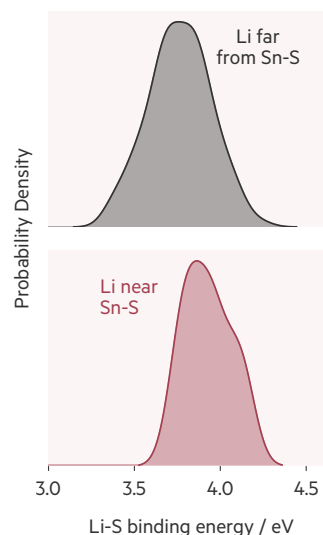
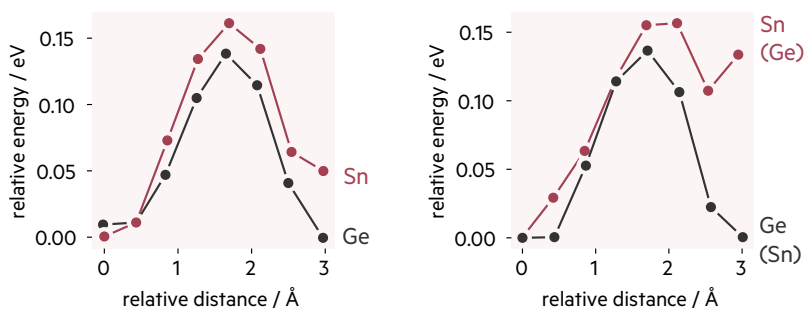


Figure 8.5: Computed probability distribution of Li vacancy formation energies in a $\text{Li}_{10}\text{GeP}_2\text{S}_{12}$ supercell containing one single Sn ion. The blue distribution shows vacancies far ($\geq 3 \text{ \AA}$) from the sulfur ions bonded to Sn, and the orange, those vacancies near the same S^{2-} ions with a distance $< 3 \text{ \AA}$. The distribution suggests that Li^+ is more strongly bound to SnS_4^{4-} tetrahedra, compared to GeS_4^{4-}

standard CI-NEB procedure, allowing all images along the diffusion path to fully relax within the CI-NEB constraints. These relaxed CI-NEB profiles show a larger potential energy barrier for $\text{Li}(3) \rightarrow \text{Li}(1)$ Li-movement in $\text{Li}_{10}\text{SnP}_2\text{S}_{12}$ than in $\text{Li}_{10}\text{GeP}_2\text{S}_{12}$, in agreement with conductivity trends from experiment and diffusion coefficients from previous molecular dynamics simulations of $\text{Li}_{10}\text{Ge}_{1-x}\text{Sn}_x\text{P}_2\text{S}_{12}$ [2]. This result, again, agrees with the qualitative predictions of the solid-electrolyte inductive effect model.

Figure 8.6: **Left** Nudged elastic band calculations performed for the $\text{Li}_{10}\text{GeP}_2\text{S}_{12}$ and $\text{Li}_{10}\text{SnP}_2\text{S}_{12}$ structures for a single lithium ion moving from a site adjacent to a (M)S-Li motif, to an adjacent lithium site. **Right**, recalculated batteries taking the relaxed structures from the initial calculations have swapped the atomic identity of *M*, e.g. Sn (Ge) refers to single point calculations along the $\text{Li}_{10}\text{GeP}_2\text{S}_{12}$ pathway, where Sn has been substituted for Ge.



The substitution of germanium for tin in $\text{Li}_{10}\text{GeP}_2\text{S}_{12}$ does not only affect the chemical bonding and charge distribution within the host-framework; it also changes the host-framework geometry. It is therefore possible that even though our data provide strong evidence for a solid-electrolyte inductive effect in $\text{Li}_{10}\text{Ge}_{1-x}\text{Sn}_x\text{P}_2\text{S}_{12}$, this might not be the cause of the conductivity trend observed in experiment—instead the observed effect may be due to the geometric effects of $\text{Ge} \rightarrow \text{Sn}$ substitution [36]. To resolve the electronic and geometric contributions to the potential-energy-barrier difference predicted for our fully-relaxed CI-NEB calculations, we performed a second set of calculations with tin fully substituted into $\text{Li}_{10}\text{GeP}_2\text{S}_{12}$ and Ge fully substituted into $\text{Li}_{10}\text{SnP}_2\text{S}_{12}$, and with each image along the diffusion pathway held fixed at the original geometry. In other words, we compute an approximate barrier for $\text{Li}_{10}\text{SnP}_2\text{S}_{12}$ fixed at the optimized $\text{Li}_{10}\text{GeP}_2\text{S}_{12}$ cell parameters and ionic positions, and for $\text{Li}_{10}\text{GeP}_2\text{S}_{12}$ fixed at the optimized $\text{Li}_{10}\text{SnP}_2\text{S}_{12}$ cell parameters and ionic positions. If the relative potential energy barriers for $\text{Li}_{10}\text{GeP}_2\text{S}_{12}$ and for $\text{Li}_{10}\text{SnP}_2\text{S}_{12}$ depend only on the difference in host-framework geometry produced by $\text{Ge} \rightarrow \text{Sn}$ substitution, we would expect the relative barriers from these cation-exchanged fixed-geometry calculations to give a lower barrier for $\text{Li}_{10}\text{SnP}_2\text{S}_{12}$ (computed using the optimized $\text{Li}_{10}\text{GeP}_2\text{S}_{12}$ geometries), and a higher barrier for $\text{Li}_{10}\text{GeP}_2\text{S}_{12}$ (computed using the optimized $\text{Li}_{10}\text{SnP}_2\text{S}_{12}$ geometries). Instead we see the opposite trend (Figure 8.6, right panel). The approximate potential-energy barrier is higher for $\text{Li}_{10}\text{SnP}_2\text{S}_{12}$ even when the geometry of the

diffusion pathway is that of fully relaxed $\text{Li}_{10}\text{GeP}_2\text{S}_{12}$. Providing these Li^+ ion potential energy barriers are effective descriptors of the variation in the true many-body free-energy surface in $\text{Li}_{10}\text{Ge}_{1-x}\text{Sn}_x\text{P}_2\text{S}_{12}$, this result suggests that the observed conductivity trend cannot be attributed solely to geometric effects, and that electronic effects, such as those described by the solid-electrolyte inductive effect model, have an effect on the ionic conductivities of the $\text{Li}_{10}\text{Ge}_{1-x}\text{Sn}_x\text{P}_2\text{S}_{12}$ series.

8.5 Conclusions

The solid-electrolyte inductive effect model offers a possible explanation for the otherwise anomalous conductivity trend observed for $\text{Li}_{10}\text{Ge}_{1-x}\text{Sn}_x\text{P}_2\text{S}_{12}$, as well as for a number of other solid electrolyte families. This model proposes that in $\text{Li}_{10}\text{Ge}_{1-x}\text{Sn}_x\text{P}_2\text{S}_{12}$ the lower electronegativity of tin compared to germanium causes Sn–S bonds to be weaker and more polar than analogous Ge–S bonds. The increased polarity of these Sn–S bonds corresponds to a larger (more negative) charge density associated with the Sn-bonded sulphur atoms, which in turn causes a stronger Coulombic attraction between these S atoms and nearby Li^+ cations. Li^+ ions adjacent to Sn-bonded S atoms are therefore expected to be more “tightly bound”—i.e. they have lower potential energies—relative to Li^+ ions further away, than otherwise equivalent Li^+ ions adjacent to Ge-bonded S atoms. This change in S–Li interaction-strength is then predicted to change the profile of the potential energy surface for lithium diffusion along the *c*-oriented one-dimensional channels, giving a higher barrier to diffusion in $\text{Li}_{10}\text{SnP}_2\text{S}_{12}$ than in $\text{Li}_{10}\text{GeP}_2\text{S}_{12}$, thereby offering an explanation for the reduced room-temperature ionic conductivity and higher lithium-conduction activation energy observed in the Sn-doped system experiments.

While this solid-electrolyte inductive effect model is chemically intuitive, and potentially explains a number of otherwise anomalous conductivity trends, there has previously been insufficient data to confirm whether this mechanism does indeed produce a significant effect in lithium-ion solid electrolytes, including $\text{Li}_{10}\text{Ge}_{1-x}\text{Sn}_x\text{P}_2\text{S}_{12}$. To address this issue, we have conducted a DFT study of the variation in bonding interactions lithium-ion potential-energy profile in the $\text{Li}_{10}\text{Ge}_{1-x}\text{Sn}_x\text{P}_2\text{S}_{12}$ series. Our calculations show that substituting Sn into $\text{Li}_{10}\text{Ge}_{1-x}\text{Sn}_x\text{P}_2\text{S}_{12}$ does indeed produce a decrease in *M*–S bonding strength, leading to an increasing electron density on S. Binding energies corroborates a stronger Coulombic attraction between Li^+ and S^{2-} . Additional CI-NEB DFT calculations indicate that these changes in *M*–S and S–Li interactions are associated with an increased potential energy barrier for Li diffusing along

the c -oriented diffusion channels. These data are all consistent with the predictions of the solid-electrolyte inductive effect model [36], and provide supporting evidence for the existence of this inductive effect in the $\text{Li}_{10}\text{Ge}_{1-x}\text{Sn}_x\text{P}_2\text{S}_{12}$ family of superionic solid electrolytes. Finally, analysis of the potential energy profile along the c -oriented diffusion channels for $\text{Li}_{10}\text{SnP}_2\text{S}_{12}$ fixed at $\text{Li}_{10}\text{GeP}_2\text{S}_{12}$ geometries and for $\text{Li}_{10}\text{GeP}_2\text{S}_{12}$ fixed at $\text{Li}_{10}\text{SnP}_2\text{S}_{12}$ geometries shows that the predictions of the solid-electrolyte inductive effect model hold even in the absence of the structural changes that accompany Sn-substitution in real materials, suggesting that the inductive effect produces a sufficiently large perturbation to the lithium-ion potential energy profile to be experimentally meaningful, even when decoupled from structural changes to the host-framework.

While the data presented here provide evidence for an experimentally significant solid-electrolyte inductive effect in the $\text{Li}_{10}\text{Ge}_{1-x}\text{Sn}_x\text{P}_2\text{S}_{12}$ system, it is unknown to what extent analogous inductive effects may be a factor in the relative ionic conductivities of other families of solid electrolytes [12, 19–21]. The $\text{Li}_{10}\text{Ge}_{1-x}\text{Sn}_x\text{P}_2\text{S}_{12}$ system may be an exceptional case because of the particular geometry of the host-framework—in this crystal structure the M -bonded S anions, i.e. those directly affected by $\text{Ge} \rightarrow \text{Sn}$ substitution, are arranged along the sides of the main c -oriented conduction pathways, and may therefore exhibit a particularly strong influence on Li^+ ion diffusion. To what extent the inductive effect does, or does not, play a role in controlling ionic transport in other families of solid electrolytes therefore remains an intriguing question for future study.

Bibliography

- (1) Bron, P.; Johansson, S.; Zick, K.; auf der Günne, J. S.; Dehnen, S.; Roling, B. *J. Am. Chem. Soc.* **2013**, *135*, 15694–15697.
- (2) Ong, S. P.; Mo, Y.; Richards, W. D.; Miara, L.; Lee, H. S.; Ceder, G. *Energy Environ. Sci.* **2013**, *6*, 148–156.
- (3) Hori, S.; Suzuki, K.; Hirayama, M.; Kato, Y.; Saito, T.; Yonemura, M.; Kanno, R. *Faraday Discuss.* **2014**, *176*, 83–94.
- (4) Kato, Y.; Saito, R.; Sakano, M.; Mitsui, A.; Hirayama, M.; Kanno, R. *J. of Power Sources* **2014**, *271*, 60–64.
- (5) Bron, P.; Dehnen, S.; Roling, B. *J. Power Sources* **2016**, *329*, 530–535.
- (6) Kato, Y.; Hori, S.; Saito, T.; Suzuki, K.; Hirayama, M.; Mitsui, A.; Yonemura, M.; Iba, H.; Kanno, R. *Nat. Energy* **2016**, *1*.

- (7) Kamaya, N.; Homma, K.; Yamakawa, Y.; Hirayama, M.; Kanno, R.; Yonemura, M.; Kamiyama, T.; Kato, Y.; Hama, S.; Kawamoto, K.; Mitsui, A. *Nat. Mater.* **2011**, *10*, 682–686.
- (8) Muy, S.; Voss, J.; Schlem, R.; Koerver, R.; Sedlmaier, S. J.; Maglia, F.; Lamp, P.; Zeier, W. G.; Shao-Horn, Y. *iScience* **2019**, *16*, 270–282.
- (9) Katcho, N. A.; Carrete, J.; Reynaud, M.; Rouse, G.; Casas-Cabanas, M.; Mingo, N.; Rodríguez-Carvajal, J.; Carrasco, J. *J. Appl. Crystallogr.* **2019**, *52*, 148–157.
- (10) Ohno, S.; Banik, A.; Dewald, G. F.; Kraft, M. A.; Krauskopf, T.; Minafra, N.; Till, P.; Weiss, M.; Zeier, W. G. *Prog. Energy* **2020**, *2*, 022001–36.
- (11) Bachman, J. C.; Muy, S.; Grimaud, A.; Chang, H. H.; Pour, N.; Lux, S. F.; Paschos, O.; Maglia, F.; Lupart, S.; Lamp, P.; Giordano, L.; Shao-Horn, Y. *Chem. Rev.* **2016**, *116*, 140–162.
- (12) Zhang, Z.; Ramos, E.; Lalère, F.; Assoud, A.; Kaup, K.; Hartman, P.; Nazar, L. F. *Energy Environ. Sci.* **2018**, *11*, 87–93.
- (13) Liu, Y.; Wang, S.; Nolan, A. M.; Ling, C.; Mo, Y. *Adv. Energy Mater.* **2020**, 2002356.
- (14) Dawson, J. A.; Famprakis, T.; Johnston, K. E. *J. Mater. Chem. A* **2021**, *9*, 18746–18772.
- (15) Iwasaki, R.; Hori, S.; Kanno, R.; Yajima, T.; Hirai, D.; Kato, Y.; Hiroi, Z. *Chem. Mater.* **2019**, *31*, 3694–3699.
- (16) Kahle, L.; Marcolongo, A.; Marzari, N. *Phys. Rev. Mater.* **2018**, *2*.
- (17) Krauskopf, T.; Culver, S. P.; Zeier, W. G. *Chem. Mater.* **2018**, *30*, 1791–1798.
- (18) Wang, Y.; Richards, W. D.; Ong, S. P.; Miara, L. J.; Kim, J. C.; Mo, Y.; Ceder, G. *Nat. Mater.* **2015**, *14*, 1026–1031.
- (19) Yu, Z.; Shang, S.-L.; Seo, J.-H.; Wang, D.; Luo, X.; Huang, Q.; Chen, S.; Lu, J.; Li, X.; Liu, Z.-K.; Wang, D. *Adv. Mater.* **2017**, *29*, 1605561.
- (20) Kwak, H.; Park, K. H.; Han, D.; Nam, K.-W.; Kim, H.; Jung, Y. S. *J. Power Sources* **2020**, *446*, 227338.
- (21) Li, X.; Liang, J.; Yang, X.; Adair, K. R.; Wang, C.; Zhao, F.; Sun, X. *Energy Environ. Sci.* **2020**, *13*, 1429–1461.
- (22) Perdew, J.; Ruzsinszky, A.; Csonka, G.; Vydrov, O.; Scuseria, G.; Constantin, L.; Zhou, X.; Burke, K. *Phys. Rev. Lett.* **2008**, *100*, 136406.

- (23) Bader, R. F. W., *Atoms in Molecules*, 1990.
- (24) Henkelman, G.; Arnaldsson, A.; Jónsson, H. *Comp. Mater. Sci.* **2006**, *36*, 354–360.
- (25) Deringer, V. L.; Tchougreff, A. L.; Dronskowski, R. *J. Phys. Chem. A* **2011**, *115*, 5461–5466.
- (26) Maintz, S.; Deringer, V. L.; Tchougréeff, A. L.; Dronskowski, R. *J. Comput. Chem.* **2013**, *34*, 2557–2567.
- (27) Maintz, S.; Deringer, V. L.; Tchougréeff, A. L.; Dronskowski, R. *J. Comput. Chem.* **2016**, *37*, 1030–1035.
- (28) Henkelman, G.; Uberuaga, B. P.; Jónsson, H. *J. Chem. Phys.* **2000**, *113*, 9901–9904.
- (29) Rong, Z.; Kitchaev, D.; Canepa, P.; Huang, W.; Ceder, G. *J. Chem. Phys.* **2016**, *145*, 074112.
- (30) Murphy, S. T.; Hine, N. D. M. *Phys. Rev. B* **2013**, *87*, 094111.
- (31) Lany, S.; Zunger, A. *Phys. Rev. B* **2009**, *80*, 085202.
- (32) Makov, G.; Payne, M. C. *Physical Review B* **1995**, *51*, 4014–4022.
- (33) Persson, K. Materials Data on Li₁₀Ge(PS₆)₂ by Materials Project, en, 2020.
- (34) Ong, S. P.; Richards, W. D.; Jain, A.; Hautier, G.; Kocher, M.; Cholia, S.; Gunter, D.; Chevrier, V. L.; Persson, K. A.; Ceder, G. *Comp. Mater. Sci.* **2013**, *68*, 314–319.
- (35) Xu, M.; Ding, J.; Ma, E. *Appl. Phys. Lett.* **2012**, *101*, 031901.
- (36) Krauskopf, T.; Culver, S. P.; Zeier, W. G. *Chem. Mater.* **2018**, *30*, 1791–1798.

Closing remarks

The subject of this thesis has been to study the point defect chemistry of emerging battery materials—specifically lithium-ion solid-state electrolytes. After discussing the importance of defect engineering in solid electrolytes for modulating both the concentration and mobility of ionic charge carriers, we study the defect chemistry of two different solid electrolytes and the response of their native defect concentrations to the introduction of aliovalent dopants. This is done using a self-consistent thermodynamic model within which the coupling between the point-defect equilibria are treated via the Fermi energy. Introducing a new charged species (the dopant) into our material perturbs the condition of charge neutrality which then influences the Fermi energy [1]. For a charged defect, the formation energy is a function of the Fermi energy, and therefore, aliovalent doping will change the concentrations of all charged defects, not just mobile-ion defects.

In the antiperovskite solid electrolyte Li_3OCl we discuss how low concentrations of native mobile-ion point defects—lithium vacancies and interstitials—suggests undoped Li_3OCl is likely to be a poor ionic conductor. Significant improvements to the ionic conductivity via aliovalent doping appear challenging. Aliovalent-doping-driven perturbations to the Fermi energy do not exclusively result in an increase in mobile ion point defects. This is particularly true when doping to increase ionic conductivity via subvalent doping intended to increase the concentration of the minority carrier, the highly mobile lithium interstitial [2]. The predominant effect of this doping strategy is an increase in the concentration of chlorine vacancies and a reduction in the concentration the majority charge-carrying mobile-ion defect, the lithium vacancy.

In applying this model to the lithium-garnet LLZO, we again find a complex response to aliovalent doping, showing that there is thermodynamic competition between the formation of lithium vacancies and lithium-zirconium antisites on supervalent doping (typically used to stabilise the high ionic conductivity cubic phase as compared to the low ionic conductivity tetragonal phase). Our model therefore predicts that composition-property relationships that are derived from the assumption

of mobile-defect charge compensation on aliovalent doping are likely to be inaccurate. We then extend our model of the defect chemistry of LLZO to examine electronic carrier populations and approximate their mobilities. In doing so we confirm that LLZO has all the qualities of an excellent electronic insulator, and it is likely that any electronic conductivity driven dendrite formation and associated battery failure is a consequence of conductivity contributions at extended defects such as grain boundaries [3, 4].

Finally we turn to the role that dopants can play in modulating the defect-formation energy and mobility landscape in $\text{Li}_{10}\text{GeP}_2\text{S}_{12}$ and carry out a first principles investigation of the so-called solid-electrolyte “inductive effect” [5]. We find corroborating evidence that isovalent doping of a less electronegative framework cation ($\text{Ge}^{4+} \rightarrow \text{Sn}^{4+}$) can modulate the charge density distribution in the host-lattice enough to influence both local defect formation energies and barriers for single-defect hopping. This shows that even very subtle chemical changes can influence the defect properties of solid electrolytes.

While it is hoped that the work and approach taken in this thesis inspires more studies which examine the point defect chemistry of solid state electrolytes which consider the coupling between the concentrations of all defect species when modelling the defect chemistry of solid electrolytes, the spectre of how to treat the inherent disorder present in many of the most effective solid electrolytes in a comprehensive defect model has not gone unnoticed. In a disordered material, the energy change upon adding or removing an ion should be computed as ensemble averages over all thermally accessible microstates as opposed to the energy difference between a single host and defective structure [6]. This presents a rather fundamental challenge, while statistical mechanical models to treat disorder in are employed in materials modelling, these typically either require a “brute-force” approach [6], or the generation of large training sets of data which can be used to train predictive models [7]. Both approaches ultimately require a large number of calculations, and as discussed in Section 3.5, accurately modelling defect properties using DFT typically requires the use of costly computational approaches. We anticipate that the development of highly accurate models of defect equilibria in disordered materials will require advances in both the thermodynamic formalism used in constructing models and in the computational approaches used for calculating defect energies. Meeting these challenges brings the promise of an improved understanding of defect chemistry of current and emerging solid electrolytes, and the potential for more accurate and practical tuning of their material properties through doping and controlled synthetic conditions led by computational modelling studies.

Bibliography

- (1) Buckeridge, J. *Comp. Phys. Commun.* **2019**, *244*, 329–342.
- (2) Li, P.; Hussain, F.; Cui, P.; Li, Z.; Yang, J. *Phys. Rev. Mater.* **2019**, *3*, 115402.
- (3) Han, F.; Westover, A. S.; Yue, J.; Fan, X.; Wang, F.; Chi, M.; Leonard, D. N.; Dudney, N. J.; Wang, H.; Wang, C. *Nat. Energy* **2019**, *4*, 187–196.
- (4) Liu, X.; Garcia-Mendez, R.; Lupini, A. R.; Cheng, Y.; Hood, Z. D.; Han, F.; Sharafi, A.; Idrobo, J. C.; Dudney, N. J.; Wang, C.; Ma, C.; Sakamoto, J.; Chi, M. *Nat. Mater.* **2021**, 1–6.
- (5) Krauskopf, T.; Culver, S. P.; Zeier, W. G. *Chem. Mater.* **2018**, *30*, 1791–1798.
- (6) Gorai, P.; Long, H.; Jones, E.; Santhanagopalan, S.; Stevanović, V. J. *Mat. Chem. A* **2020**, *8*, 3851–3858.
- (7) Van der Ven, A.; Ceder, G. *Phys. Rev. B* **2005**, *71*, 10–7.